Selected open-charm decays of the narrow P_c states: Quark-interchange predictions and pion-exchange sensitivity

Vandan Patel[*] and Ajay Kumar Rai[†]

Department of Physics, Sardar Vallabhbhai National Institute of Technology, Surat, Gujarat-395007, India

(Received 24 August 2026; accepted 7 October 2026; published 30 October 2026)

The proximity of the narrow $P_c(4312)$, $P_c(4440)$, and $P_c(4457)$ structures to the $\Sigma_c\bar{D}^{(*)}$ thresholds motivates their interpretation as hadronic molecules. We treat the $P_c(4312)$ as an S-wave $\Sigma_c\bar{D}$ state with $J^P = 1/2^-$ and examine both $J^P = 1/2^-$ and $3/2^-$ $\Sigma_c\bar{D}^*$ assignments for each heavier peak. The selected S-wave open-charm transitions to $\Lambda_c\bar{D}^{(*)}$ are calculated at Born order in the quark-interchange model, including the prior and post rearrangement diagrams and their color, flavor, spin, and spatial matrix elements. Across the input variations considered, the quark-interchange widths robustly favor $\Lambda_c\bar{D}^*$ over $\Lambda_c\bar{D}$ for every $J^P = 1/2^-$ assignment. At either heavier peak mass, the $\Lambda_c\bar{D}^*$ width for $J^P = 3/2^-$ is suppressed by approximately one order of magnitude relative to $J^P = 1/2^-$, providing a potential decay-based discriminator of the spin assignments. The large channel hierarchies arise from spatial overlaps and interference between spin-independent and hyperfine contributions and are not universal heavy-quark-spin-symmetry ratios. We also explore a retarded one-pion-exchange transition at first Born order. It affects $P_c(4312)\to\Lambda_c\bar{D}^*$ most strongly, while the coherent widths remain sensitive to the cutoff, energy-transfer prescription, short-distance subtraction, and unresolved relative matching sign. The quark-interchange hierarchies are therefore the central predictions, whereas the pion-exchange results quantify matching sensitivity. Measurements of the $\Lambda_c\bar{D}^*$ modes can directly test these patterns.

DOI: 10.1103/6ldz-y3vh

I. INTRODUCTION

The spectroscopy of hadrons beyond conventional quark-antiquark and three-quark configurations provides an important probe of nonperturbative quantum chromodynamics. The expanding exotic-hadron spectrum includes both tetraquark and pentaquark candidates, for which compact-multiquark and hadronic-molecular descriptions are among the principal interpretations [1,2]. Phenomenological studies range from Regge-trajectory analyses of tetraquark spectra across the light, strange, charm, and bottom flavor sectors [3–5] to constituent-model investigations of beauty-containing tetraquark spectroscopy and decay dynamics [6] and of singly charmed pentaquark spectra and meson-baryon decay patterns [7]. Since different structural hypotheses can produce similar mass spectra, decay observables are especially valuable for discriminating among them.

In the hidden-charm baryon sector, the LHCb Collaboration first observed structures in the $J/\psi p$ invariant-mass distribution of $\Lambda_b^0\to J/\psi pK^-$ decays [8]. A later analysis with a larger data sample revealed the narrow $P_c(4312)^+$ state and resolved the former $P_c(4450)^+$ enhancement into the nearby $P_c(4440)^+$ and $P_c(4457)^+$ peaks [9]. Their proximity to the $\Sigma_c\bar{D}$ and $\Sigma_c\bar{D}^*$ thresholds makes a hadronic-molecular interpretation particularly attractive, although compact multiquark configurations and kinematic mechanisms have not been excluded; see Refs. [10,11] for reviews.

In the simplest S-wave molecular picture, the $P_c(4312)$ is predominantly an isospin-1/2 $\Sigma_c\bar{D}$ state with $J^P = 1/2^-$, whereas the $P_c(4440)$ and $P_c(4457)$ are associated, in an experimentally unresolved order, with the $J^P = 1/2^-$ and $3/2^-$ $\Sigma_c\bar{D}^*$ states. Such a multiplet arises naturally in descriptions based on heavy-quark spin symmetry (HQSS) and coupled-channel dynamics [12–14]. The peak masses alone have not fixed the spin ordering, and theoretical assignments remain model dependent. This motivates the central question of the present work: can selected open-charm decay hierarchies distinguish the two molecular spin assignments?

Decay observables contain information not supplied by the masses. HQSS gives characteristic relations among

[*]Contact author: vandankp12998@gmail.com
[†]Contact author: raiajayk@gmail.com

Published by the American Physical Society under the terms of the Creative Commons Attribution 4.0 International license. Further distribution of this work must maintain attribution to the author(s) and the published article's title, journal citation, and DOI. Funded by SCOAP³.

hidden-charm $J/\psi N$ and $\eta_c N$ modes and, under molecular assumptions, among open-charm $\Lambda_c\bar{D}^{(*)}$ modes [15,16]. Effective-Lagrangian calculations have estimated a broader set of allowed strong decays [17]. At the constituent level, Wang *et al.* applied the quark-interchange (QI) model to $P_c \to J/\psi p, \eta_c p$ and showed that hidden-charm decay ratios can probe the molecular composition [18]. Because the QI transition is generated by constituent interactions constrained by ordinary hadron spectroscopy rather than channel-specific P_c–hadron couplings, it provides a microscopic framework for studying open-charm rearrangement decays as well. Coupled-channel and compositeness analyses have also treated the $\Lambda_c\bar{D}^{(*)}$ channels explicitly and extracted their couplings, decay strengths, or production rates [19,20].

Several approaches already indicate that $\Lambda_c\bar{D}^*$ is an especially informative final state. Constituent-quark, Bethe-Salpeter, and complex-scaling calculations find a pronounced $\Lambda_c\bar{D}^*$ preference for the $P_c(4312)$, although their absolute widths and dynamical treatments differ [21–23]. Group-theoretical analyses likewise identify spin-dependent restrictions in hidden- and open-charm channels [24]. For the two heavier peaks, however, no common spin assignment has emerged. Complex-scaling and pion-exchange triangle-diagram studies favor $J[P_c(4440)] = 1/2$ and $J[P_c(4457)] = 3/2$ under their respective assumptions [23,25], whereas coupled-channel, Bethe-Salpeter, effective-Lagrangian, and Born-Oppenheimer effective field theory (EFT) analyses have supported the reverse ordering [14,26–28]. Phenomenological constraints based on the disparity between the $\Lambda_c\bar{D}$ and $\Lambda_c\bar{D}^*$ modes also favor $J[P_c(4440)] = 3/2$, while questioning whether $P_c(4457)$ belongs to the same simple molecular multiplet [29].

Long-distance pion dynamics must also be interpreted with care. Iterated tensor one-pion exchange (OPE) in nonperturbative multichannel calculations requires suitable short-distance operators for regulator independence, and on-shell $\Lambda_c\bar{D}^{(*)}\pi$ intermediate states generate three-body cuts in a unitary description [14,23]. Dedicated effective-Lagrangian calculations also find sizable $\bar{D}^{(*)}\Lambda_c\pi$ three-body widths and identify these modes as promising search channels [30]. Moreover, the short-range part of OPE cannot be separated from contact or quark-exchange dynamics in a model-independent way; its treatment can affect spin-dependent conclusions [31]. A Born-level QI-OPE combination must therefore be presented as a controlled sensitivity study rather than a complete coupled-channel construction.

The relevant open-charm final states are experimentally accessible. LHCb has observed $\Lambda_b^0 \to \Lambda_c^+ \bar{D}^{(*)0} K^-$ decays and identified them as useful normalization channels for future pentaquark searches in the same final states [32]. A complementary LHCb search for prompt pentaquark production in charm-hadron final states found no significant signal and established upper limits on the corresponding yields [33]. Theoretical studies also identify $\Lambda_b^0 \to \Lambda_c^+ \bar{D}^{*0} K^-$ as a promising channel for future searches [20,29]. Measurements of the resonant $\Lambda_c\bar{D}^{(*)}$ strengths can consequently test both channel hierarchies and the spin dependence of the two heavier structures.

In this work, we calculate the selected transitions $\Sigma_c\bar{D}^{(*)} \to \Lambda_c\bar{D}^{(*)}$ for the $P_c(4312)$, $P_c(4440)$, and $P_c(4457)$, treating the initial states as pure S-wave molecules. Our central calculation evaluates the S-wave QI amplitudes at Born order, including all retained prior and post rearrangement diagrams and their color, flavor, spin, and spatial matrix elements. We test the resulting partial widths against variations of the molecular scale, threshold prescription, and constituent inputs. The $\Lambda_c\bar{D}^*$ mode is favored for every tested $J^P = 1/2^-$ assignment and is strongly suppressed for $J^P = 3/2^-$ at a fixed heavier peak mass. We then supplement QI with a direct retarded OPE kernel at first Born order. A pion-pole prescription and the full regulated kernel are used to diagnose long-distance and short-distance-matching sensitivity, including the unresolved global QI-OPE sign. The QI patterns are our central predictions; the coherent QI + OPE widths are alternative matching scenarios. The calculation is restricted to the selected channels and to final S waves. In particular, $P_c(J^P = 3/2^-) \to \Lambda_c\bar{D}$ begins in a D wave and is not evaluated.

The paper is organized as follows. Section II defines the molecular assignments, kinematics, and amplitude conventions. Sections III and IV construct the QI and OPE transition mechanisms. Numerical inputs and validation checks are given in Sec. V, followed by the results and discussion in Sec. VI. Section VII summarizes the conclusions and outlook.

II. MOLECULAR ASSIGNMENTS, KINEMATICS, AND CONVENTIONS

We work in natural units, $\hbar = c = 1$. This Section fixes the channel states, partial-wave truncation, molecular wave functions, and amplitude normalization used throughout the calculation. We first specify the spin-isospin basis and the allowed final partial waves, then define the initial radial wave function, and finally connect the transition kernels constructed in Secs. III and IV to the partial widths.

The three narrow structures reported by LHCb [9] are treated as near-threshold hadronic molecules with total isospin $I = \frac{1}{2}$. The configurations considered are

$$P_c(4312)^+ : \left|\Sigma_c\bar{D}; I = \frac{1}{2}, J^P = \frac{1}{2}^-\right\rangle, \tag{1}$$

$$P_c(4440)^+, P_c(4457)^+ : \left|\Sigma_c\bar{D}^*; I = \frac{1}{2}\right\rangle,$$
$$J^P = \frac{1}{2}^- \quad \text{or} \quad J^P = \frac{3}{2}^-. \tag{2}$$

Their proximity to the corresponding $\Sigma_c\bar{D}^{(*)}$ thresholds motivates these assignments. For ground-state constituents in a relative S wave, $\Sigma_c\bar{D}$ has $J^P = \frac{1}{2}^-$, whereas $\Sigma_c\bar{D}^*$ allows $J^P = \frac{1}{2}^-$ and $\frac{3}{2}^-$. These assignments are widely used in molecular descriptions of the narrow P_c states [12,13,18,23].

Because the relative spin ordering of the two heavier peaks remains model dependent [12,14,23,34], we do not impose either ordering at this stage. Instead, both $J^P = \frac{1}{2}^-$ and $\frac{3}{2}^-$ are evaluated for each peak. Hence, Eqs. (1) and (2) define five state-spin cases: one for $P_c(4312)$ and two for each heavier state.

At the level of the initial molecular wave function, every case is approximated as a pure, single-channel $\Sigma_c\bar{D}^{(*)}$ molecule; coupled-channel admixtures and their dynamical feedback are outside the baseline calculation. The spin-flavor wave functions and charge-channel reconstruction are evaluated in the isospin-symmetric limit. Physical charged and neutral hadron masses enter only through the explicitly stated molecular threshold prescription and two-body kinematics; they do not alter the isospin Clebsch-Gordan algebra.

A. Isospin, spin, and allowed partial waves

We denote total isospin and its third component by I and I_3, total angular momentum and its projection by J and M_J, and the initial (final) relative orbital angular momentum and channel spin by L_i, S_i (L_f, S_f). We use the Condon-Shortley convention for isospin Clebsch-Gordan coefficients and fix the charge-state phases by

$$|\Sigma_c^{++}\rangle = |1,+1\rangle, \qquad |\Sigma_c^{+}\rangle = |1,0\rangle,$$
$$|\bar{D}^{(*)0}\rangle = \left|\frac{1}{2},+\frac{1}{2}\right\rangle, \qquad |D^{(*)-}\rangle = \left|\frac{1}{2},-\frac{1}{2}\right\rangle. \tag{3}$$

The positively charged $I = 1/2$ initial state is then

$$\left|\Sigma_c\bar{D}^{(*)}; I=\frac{1}{2}, I_3=+\frac{1}{2}\right\rangle = \sqrt{\frac{2}{3}}|\Sigma_c^{++}D^{(*)-}\rangle - \frac{1}{\sqrt{3}}|\Sigma_c^{+}\bar{D}^{(*)0}\rangle. \tag{4}$$

Because Λ_c is an isosinglet, the corresponding $I = 1/2$ final state is simply

$$\left|\Lambda_c\bar{D}^{(*)}; I=\frac{1}{2}, I_3=+\frac{1}{2}\right\rangle = |\Lambda_c^{+}\bar{D}^{(*)0}\rangle. \tag{5}$$

The QI calculation explicitly evaluates the charged initial component $\Sigma_c^{++}D^{(*)-}$. To show how this result determines the physical $I = 1/2$ transition, let $\mathcal{A}_{\rm ch}$ and $\mathcal{A}_{\rm neu}$ denote, for any fixed spin and momentum arguments, the amplitudes from the charged and neutral initial components, respectively. Let $\mathcal{A}_{1/2}$ be the amplitude between the normalized $I = 1/2$ states in Eqs. (4) and (5). Since the strong transition operator is an isoscalar, its $I = 3/2 \to I = 1/2$ matrix element vanishes. The Clebsch-Gordan projections therefore give

$$\mathcal{A}_{\rm ch} = \sqrt{\frac{2}{3}}\mathcal{A}_{1/2}, \qquad \mathcal{A}_{\rm neu} = -\frac{1}{\sqrt{3}}\mathcal{A}_{1/2} = -\frac{\mathcal{A}_{\rm ch}}{\sqrt{2}},$$
$$\mathcal{A}_{1/2} = \sqrt{\frac{2}{3}}\mathcal{A}_{\rm ch} - \frac{1}{\sqrt{3}}\mathcal{A}_{\rm neu} = \sqrt{\frac{3}{2}}\mathcal{A}_{\rm ch}. \tag{6}$$

By linearity, Eq. (6) applies both to a charge-channel kernel at fixed momenta and to the amplitude obtained after folding that kernel with the molecular wave function. Its use in constructing the physical QI kernel is made explicit in Sec. III. The neutral charge diagrams are therefore not recalculated independently with charge-dependent masses. An overall phase of either channel is conventional, but the relative sign in Eq. (4) must be retained. The additional relative phase required when QI and OPE are combined is discussed in Sec. IV.

For later use, consider an initial molecular state with relative momentum $\mathbf{p}$, $p = |\mathbf{p}|$, and $\hat{\mathbf{p}} = \mathbf{p}/p$. Its spin-orbital wave function is written as

$$\Psi_{P_c}^{JM_J}(\mathbf{p}) = \sum_{m_{L_i}, M_{S_i}} \langle L_i m_{L_i}, S_i M_{S_i} | J M_J\rangle \times R_{L_i}(p) Y_{L_i m_{L_i}}(\hat{\mathbf{p}}) [\chi_A \otimes \chi_B]_{S_i M_{S_i}}, \tag{7}$$

where $A = \bar{D}^{(*)}$ is the initial anticharmed meson, $B = \Sigma_c$ is the initial charmed baryon, R_{L_i} is the radial wave function, and $Y_{L_i m_{L_i}}$ is a spherical harmonic. The bracketed product couples the meson and baryon spins to S_i, M_{S_i}. Although channel names are often written in baryon-meson order, spin states are coupled in meson-baryon order in both the initial and final channels; this convention fixes the associated Clebsch-Gordan phases. The constituent-hadron spins are $s_{\bar{D}} = 0$, $s_{\bar{D}^*} = 1$, and $s_{\Sigma_c} = 1/2$.

For the initial S waves retained here, $L_i = m_{L_i} = 0$ and $S_i = J$; $R_{L_i=0}$ is the state-dependent function R_0 defined in Sec. II B. The final meson and baryon spins are likewise coupled in the basis $[\chi_{M_f} \otimes \chi_{B_f}]_{S_f M_{S_f}}$, where $M_f = \bar{D}^{(*)}$ and $B_f = \Lambda_c$.

The intrinsic parities of $M_f = \bar{D}^{(*)}$ and $B_f = \Lambda_c$ are $-$ and $+$, respectively. Their two-body parity is therefore

$$P_f = P_{M_f} P_{B_f} (-1)^{L_f} = -(-1)^{L_f}. \tag{8}$$

Parity conservation for a negative-parity P_c requires even L_f. For $L_f = 0$, the $\Lambda_c\bar{D}$ channel has $S_f = 1/2$ and hence only $J = 1/2$, whereas $\Lambda_c\bar{D}^*$ has $S_f = 1/2$ or $3/2$ and

TABLE I. Lowest parity- and angular-momentum-allowed partial waves for the selected open-charm channels. The D-wave channel is physically allowed but is not evaluated in this work.

Initial configuration	J^P	$\Lambda_c\bar{D}$	$\Lambda_c\bar{D}^*$
$\Sigma_c\bar{D}$	$\frac{1}{2}^-$	S wave	S wave
$\Sigma_c\bar{D}^*$	$\frac{1}{2}^-$	S wave	S wave
$\Sigma_c\bar{D}^*$	$\frac{3}{2}^-$	D wave	S wave

admits both values of J considered here. The lowest allowed partial waves are summarized in Table I.

The $\Lambda_c\bar{D}$ entry in the last row is not a selection-rule zero: $P_c(3/2^-)\to\Lambda_c\bar{D}$ begins at $L_f = 2$. Our calculation retains only the diagonal $L_i = L_f = 0$ projection and does not evaluate the $L_i = 0\to L_f = 2$ amplitude generated by noncentral rank-two terms. Thus, this decay is uncalculated rather than forbidden. A rough order-of-magnitude comparison with calculations that retain the required rank-two transition operators is given in Sec. VI D. The five state-spin cases and the selected final channels consequently give eight calculated S-wave widths.

B. Molecular wave function and binding prescription

Following the pure-molecule scenario of Wang *et al.* [18], we retain only the dominant initial $\Sigma_c\bar{D}^{(*)}$ component. Its relative S-wave momentum distribution is approximated by the normalized Gaussian

$$\psi_{P_c}(\mathbf{p}) = R_0(p)Y_{00}(\hat{\mathbf{p}}),$$
$$R_0(p) = \frac{2}{\pi^{1/4}\beta_{P_c}^{3/2}}\exp\left(-\frac{p^2}{2\beta_{P_c}^2}\right), \tag{9}$$

where $Y_{00} = 1/\sqrt{4\pi}$ and β_{P_c} is the molecular momentum width. The normalization is

$$\int_0^\infty p^2\,dp|R_0(p)|^2 = 1, \qquad \int d^3p|\psi_{P_c}(\mathbf{p})|^2 = 1. \tag{10}$$

The peak dependence of R_0 enters through β_{P_c} and is suppressed in the notation.

For a selected pair of initial-hadron masses M_A and M_B, define the positive binding energy and reduced mass by

$$E_{\rm bind} = M_A + M_B - M_{P_c} > 0, \quad \mu_{AB} = \frac{M_A M_B}{M_A + M_B}. \tag{11}$$

The Gaussian root-mean-square radius and the characteristic molecular size used in Ref. [18] are

$$r_{\rm rms}^{(G)} = \sqrt{\frac{3}{2}}\frac{1}{\beta_{P_c}}, \qquad r_{\rm typ} = \frac{1}{\sqrt{2\mu_{AB}E_{\rm bind}}}. \tag{12}$$

Equating these two scales gives the working prescription

$$\beta_{P_c} = \sqrt{3\mu_{AB}E_{\rm bind}}. \tag{13}$$

Equation (13) is a phenomenological Gaussian-size prescription; it is not the universal zero-range expression for a bound-state root-mean-square radius.

For the reference calculation, M_A and M_B in Eq. (11) are set equal to the arithmetic charge averages

$$M_A^{\rm av} = \frac{1}{2}(M_{D^{(*)-}} + M_{\bar{D}^{(*)0}}),$$
$$M_B^{\rm av} = \frac{1}{2}(M_{\Sigma_c^{++}} + M_{\Sigma_c^+}),$$
$$\bar{M}_{\rm th}^{D^{(*)}} \equiv M_A^{\rm av} + M_B^{\rm av}, \qquad \mu_{AB}^{\rm av} \equiv \frac{M_A^{\rm av}M_B^{\rm av}}{M_A^{\rm av} + M_B^{\rm av}}. \tag{14}$$

Thus, the central values use $E_{\rm bind} = \bar{M}_{\rm th}^{D^{(*)}} - M_{P_c}$ and $\mu_{AB} = \mu_{AB}^{\rm av}$. The averaged threshold is the arithmetic mean of the $\Sigma_c^{++}D^{(*)-}$ and $\Sigma_c^+\bar{D}^{(*)0}$ thresholds, not a Clebsch-Gordan–weighted average. The two physical thresholds and direct variations of β_{P_c} are later used as sensitivity tests; their numerical values are given in Sec. V.

C. Two-body kinematics, amplitudes, and widths

For a fixed transition, let i denote the initial P_c channel and $f = M_f B_f$ the final two-hadron channel, with $M_f = \bar{D}^{(*)}$ and $B_f = \Lambda_c$. A suffix fi is always ordered as final, initial, in accordance with a matrix element $\langle f|V|i\rangle$. In the P_c rest frame, the four-momenta are

$$P^\mu = (M_{P_c}, \mathbf{0}), \qquad k = |\mathbf{k}|,$$
$$p_M^\mu = (E_{M_f}, \mathbf{k}), \qquad p_B^\mu = (E_{B_f}, -\mathbf{k}). \tag{15}$$

The final relative-momentum magnitude is

$$k = \frac{\lambda_{\rm K}^{1/2}(M_{P_c}^2, M_{M_f}^2, M_{B_f}^2)}{2M_{P_c}},$$
$$\lambda_{\rm K}(x,y,z) = x^2 + y^2 + z^2 - 2xy - 2xz - 2yz, \tag{16}$$

where M_{M_f} and M_{B_f} are the physical final-hadron masses. Their energies are

$$E_{M_f} = \sqrt{M_{M_f}^2 + k^2}, \qquad E_{B_f} = \sqrt{M_{B_f}^2 + k^2}. \tag{17}$$

We use the delta-normalized scattering states and partial-wave convention of Ref. [18], $\langle\mathbf{p}'|\mathbf{p}\rangle = \delta^3(\mathbf{p}' - \mathbf{p})$. The transition dynamics is first represented by the spin-coupled, but molecularly unfolded, kernel $V_{{\rm eff};fi}^{(J)}(k,p,u)$, where

$$u = \hat{\mathbf{k}}\cdot\hat{\mathbf{p}}$$

is the cosine of the angle between the final and initial relative momenta. Here $\mathbf{p}$ is the initial relative momentum as mentioned earlier. The kernel is evaluated between normalized spin-coupled initial and final channel states with the same J, M_J. For the central $L_i = L_f = 0$ sector retained here, rotational invariance makes the projected scalar amplitude independent of the particular value of M_J. For $L_i = L_f = 0$, the zeroth Legendre polynomial is $P_0(u) = 1$. Folding the corresponding S-wave kernel with the initial radial wave function therefore defines

$$T^{(J)}_{00;fi}(k) = \int_0^\infty p^2\, dp\, R_0(p) \times \int_{-1}^{1} du\, V^{(J)}_{\mathrm{eff};fi}(k,p,u). \tag{18}$$

The first and second zero in $T^{(J)}_{00;fi}$ denote $L_f = 0$ and $L_i = 0$, respectively. The superscript (J) labels the conserved total-angular-momentum channel.

Let s_M, m_M and s_B, m_B be the spins and canonical spin projections of M_f and B_f, defined along a common quantization axis. Since $L_f = 0$, $S_f = J$, and the polarization-resolved nonrelativistic amplitude is

$$\mathcal{T}_{fi;M_J;m_M m_B}(\mathbf{k}) = \frac{T^{(J)}_{00;fi}(k)}{(2\pi)^2} Y_{00}(\hat{\mathbf{k}}) \times \langle s_M m_M, s_B m_B | J M_J \rangle. \tag{19}$$

The Clebsch-Gordan coefficient converts the final state from the coupled-spin basis to definite meson and baryon spin projections. All dynamical spin dependence remains in $T^{(J)}_{00;fi}$.

Writing $\hat{V}_{\mathrm{eff}}$ for the transition operator whose unfolded kernel appears in Eq. (18), and abbreviating the complete final state as $|f;\mathbf{k}, m_M m_B\rangle \equiv |M_f(\mathbf{k}, m_M) B_f(-\mathbf{k}, m_B)\rangle$, the same amplitude is related to the relativistically normalized decay amplitude by

$$\mathcal{T}_{fi;M_J;m_M m_B}(\mathbf{k}) \equiv \langle f;\mathbf{k}, m_M m_B | \hat{V}_{\mathrm{eff}} | P_c(J M_J)\rangle = -\frac{\mathcal{M}_{fi;M_J;m_M m_B}}{\mathcal{N}_f},$$
$$\mathcal{N}_f = (2\pi)^{3/2}\sqrt{2M_{P_c}}\sqrt{2E_{M_f}}\sqrt{2E_{B_f}}. \tag{20}$$

Thus, $V^{(J)}_{\mathrm{eff};fi}$, $T^{(J)}_{00;fi}$, $\mathcal{T}_{fi}$, and $\mathcal{M}_{fi}$ denote, respectively, the unfolded kernel, its molecularly folded S-wave amplitude, the polarization-resolved nonrelativistic matrix element, and the relativistic decay amplitude.

In terms of $\mathcal{M}_{fi}$, the standard two-body decay formula is

$$\Gamma^{(J)}_{fi} = \frac{k}{32\pi^2 M^2_{P_c}} \frac{1}{2J+1} \times \sum_{M_J, m_M, m_B} \int d\Omega_k |\mathcal{M}_{fi;M_J;m_M m_B}|^2. \tag{21}$$

For the QI contribution, explicit spin matrix elements are evaluated at $M_J = +1/2$; the OPE coefficients are already projected onto definite-J channels. The quantity $T^{(J)}_{00;fi}$ is independent of M_J by rotational invariance, but it is not a Wigner-Eckart reduced matrix element. The Clebsch-Gordan normalization gives

$$\frac{1}{2J+1} \sum_{M_J, m_M, m_B} |\langle s_M m_M, s_B m_B | J M_J\rangle T^{(J)}_{00;fi}(k)|^2 = |T^{(J)}_{00;fi}(k)|^2. \tag{22}$$

Using Eqs. (19)–(22) together with $\int d\Omega_k |Y_{00}|^2 = 1$, Eq. (21) reduces to

$$\Gamma^{(J)}_{fi} = \rho_{fi} |T^{(J)}_{00;fi}(k)|^2, \qquad \rho_{fi} \equiv \frac{k E_{M_f} E_{B_f}}{(2\pi)^3 M_{P_c}}. \tag{23}$$

Thus, for each retained S-wave channel, the initial-spin average is exactly cancelled by the complete sum over the normalized final spin states; no additional factor of $2J+1$ is inserted.

In the conventions used here, $[V^{(J)}_{\mathrm{eff};fi}] = \mathrm{GeV}^{-2}$, $[R_0] = \mathrm{GeV}^{-3/2}$, and $[T^{(J)}_{00;fi}] = \mathrm{GeV}^{-1/2}$. Consequently, $[\rho_{fi}] = \mathrm{GeV}^2$ and Eq. (23) yields a width in GeV.

The assignments and normalized radial wave functions specified above define the initial states. Section III constructs the short-range QI contribution to $V^{(J)}_{\mathrm{eff};fi}$, while Sec. IV constructs the OPE contribution and converts it to the same normalization. Only the spin–isospin-reduced OPE transition kernel is taken from Ref. [23]; its complex-scaled resonance wave functions and c-product normalization are not used. Inserting either kernel into Eq. (18) gives its contribution to $T^{(J)}_{00;fi}$, and the corresponding partial width then follows from Eq. (23). All QI and OPE amplitudes quoted below are expressed in this common convention.

III. QUARK-INTERCHANGE TRANSITION MECHANISM

This Section constructs the short-range QI contribution $V^{(J)}_{\mathrm{QI};fi}$ to the generic transition kernel $V^{(J)}_{\mathrm{eff};fi}$ introduced in Sec. II C. The construction proceeds in four steps. We first identify the labeled constituent rearrangements and their prior and post Born representations. We then specify the

pairwise constituent interaction and evaluate its color, flavor, spin, and spatial matrix elements. Finally, we antisymmetrize the two identical light quarks and project the explicitly calculated charge component onto the physical $I = 1/2$ channel. Folding the resulting kernel with $R_0(p)$ gives the QI contribution to $T^{(J)}_{00;fi}$.

At Born order, a constituent interaction acts between the two incoming color-singlet hadrons, after which their constituents are recombined into the outgoing hadrons [18,35–39]. The mechanism is short ranged at the hadronic level because the internal wave functions of the incoming hadrons must overlap for the constituent rearrangement to occur. Those finite wave functions also suppress the kernel at large external momenta.

We evaluate explicitly the charged initial component appearing in Eq. (4). Its constituents are labeled as

$$A(12) = D^{(*)-}(\bar{c}_1 d_2), \qquad B(345) = \Sigma_c^{++}(c_3 u_4 u_5), \quad (24)$$

where A denotes the initial anticharmed meson and B the initial charmed baryon. Either identical u quark can enter the final anticharmed meson, so the same physical final channel has two temporarily labeled clusterings,

$$F_{14}\colon\ M_f(14) + B_f(325),$$
$$M_f(14) = (\bar{c}_1 u_4), \qquad B_f(325) = (c_3 d_2 u_5), \quad (25)$$

$$F_{15}\colon\ M_f(15) + B_f(324),$$
$$M_f(15) = (\bar{c}_1 u_5), \qquad B_f(324) = (c_3 d_2 u_4). \quad (26)$$

Here $M_f = \bar{D}$ or $\bar{D}^*$ and $B_f = \Lambda_c$. The labels 14 and 15 identify which u quark enters M_f; they do not denote distinct asymptotic decay channels. Although physical channel names are commonly written in baryon-meson order, all spin products below retain the meson-baryon coupling order fixed in Sec. II A.

A. Born kernels and prior-post representations

The same constituent Hamiltonian may be partitioned with respect to either the initial or final hadron clusters,

$$\hat{H} = \hat{H}^0_A + \hat{H}^0_B + \hat{V}_{AB} = \hat{H}^0_{M_f} + \hat{H}^0_{B_f} + \hat{V}_{M_f B_f}. \quad (27)$$

The residual operator $\hat{V}_{AB}$ connects constituents belonging to different initial clusters, whereas $\hat{V}_{M_f B_f}$ connects constituents belonging to different final clusters. These two partitions define, respectively, the prior and post Born kernels. For a labeled final clustering F_a, with $a \in \{14, 15\}$, they are

$$V^{(J)}_{\mathrm{pr},a}(k,p,u) \equiv \langle F_a; JM_J|\hat{V}_{AB}|AB; JM_J\rangle,$$
$$V^{(J)}_{\mathrm{po},a}(k,p,u) \equiv \langle F_a; JM_J|\hat{V}_{M_f B_f}|AB; JM_J\rangle. \quad (28)$$

Thus, Eq. (28) is the constituent-level realization of the unfolded kernel in Eq. (18), before identical-quark antisymmetrization and isospin projection. The external variables are the final momentum k, initial momentum p, and $u = \hat{\mathbf{k}} \cdot \hat{\mathbf{p}}$. The superscript (J) labels the conserved total-angular-momentum channel. We evaluate explicit spin matrix elements at $M_J = +1/2$; rotational invariance makes the scalar kernel independent of this choice.

Replacing the two residual operators by sums of pairwise constituent interactions gives the ordered pair sets

$$\mathcal{P}_{\mathrm{pr},a} = \{13, 14, 15, 23, 24, 25\}, \quad (29)$$

$$\mathcal{P}_{\mathrm{po},14} = \{13, 12, 15, 43, 42, 45\}, \quad (30)$$

$$\mathcal{P}_{\mathrm{po},15} = \{13, 12, 14, 53, 52, 54\}. \quad (31)$$

For example, 13 denotes an interaction between constituents 1 and 3, with the first label fixing the direction assigned to the transferred momentum. The prior set connects the two initial clusters; each post set connects the two final clusters. Figure 1 displays the complete prior and post sets for F_{14}. The F_{15} diagrams follow from the exchange $4 \leftrightarrow 5$.

For exact on-shell eigenstates, the prior and post representations are equivalent. Small differences arise in practical calculations that use variational internal hadron wave functions [18,36,38]. Following Ref. [18], we therefore use their arithmetic average for each labeled clustering,

$$V^{(J)}_a(k,p,u) = \frac{1}{2}[V^{(J)}_{\mathrm{pr},a}(k,p,u) + V^{(J)}_{\mathrm{po},a}(k,p,u)]. \quad (32)$$

The factor $1/2$ in Eq. (32) is included once, when the diagram coefficients are assembled below.

B. Constituent interaction and internal hadron states

For an ordered constituent pair $\nu\nu'$, with $\nu, \nu' \in \{1, \ldots, 5\}$, let $\mathbf{q}_{\nu\nu'}$ be the momentum transferred to constituent ν; constituent ν' receives $-\mathbf{q}_{\nu\nu'}$. We use the momentum-space interaction of Ref. [18],

$$V_{\nu\nu'}(\mathbf{q}_{\nu\nu'}) = \mathbf{t}_\nu \cdot \mathbf{t}_{\nu'}\left[\frac{4\pi\alpha_s(\mathcal{Q}^2_{\nu\nu'})}{q^2_{\nu\nu'}} + \frac{6\pi b}{q^4_{\nu\nu'}} - \frac{8\pi\alpha_s(\mathcal{Q}^2_{\nu\nu'})}{3m_\nu m_{\nu'}}\mathbf{s}_\nu \cdot \mathbf{s}_{\nu'} e^{-q^2_{\nu\nu'}/(4\tau^2_{\mathrm{hf}})}\right], \quad (33)$$

where $q_{\nu\nu'} = |\mathbf{q}_{\nu\nu'}|$, m_ν is a constituent mass, b is the string tension, τ_{hf} is the hyperfine smearing scale, and $\mathbf{s}_\nu$ is the spin operator of constituent ν. The color generator is $\mathbf{t} = \boldsymbol{\lambda}^c/2$ for a quark and $\mathbf{t}_{\bar{q}} = -\mathbf{t}^*_q$ for an antiquark, where $\boldsymbol{\lambda}^c$ denotes the eight Gell-Mann matrices. The first two terms in Eq. (33) are the Coulomb and linear-confinement contributions; together we label them CL. The last term

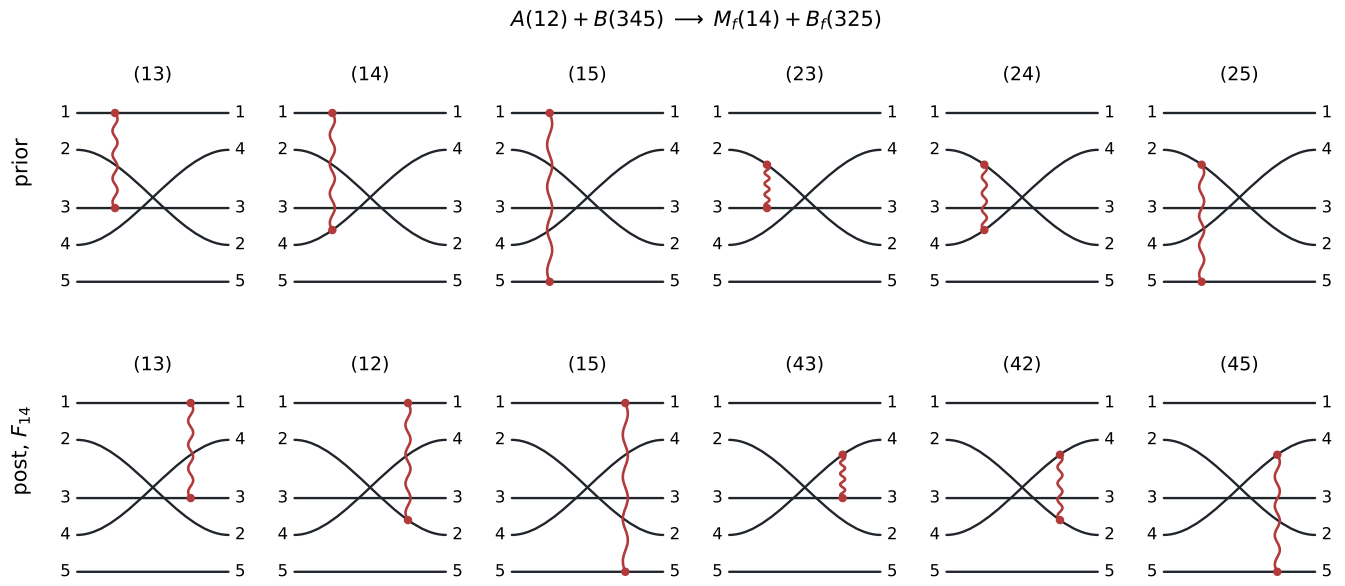


FIG. 1. Born-order QI diagrams for the labeled clustering F_{14}, $A(12)+B(345)\to M_f(14)+B_f(325)$. Quark lines run from left to right. The red wavy line denotes one constituent interaction $V_{\nu\nu'}$; only its endpoints are interaction vertices, and crossings with spectator lines do not represent additional interactions. The upper and lower rows contain the complete prior and post pair sets, respectively. The crossing trajectories display the constituent interchange. The clustering F_{15} is obtained by $4\leftrightarrow 5$ and is not drawn separately.

is the smeared hyperfine contribution, labeled HF. Tensor and spin-orbit interactions are not included in the present S-wave calculation.

The running coupling is

$$\alpha_s(Q^2)=\frac{12\pi}{(33-2n_f)\ln\left(A_\alpha+Q^2/B_\alpha^2\right)}. \tag{34}$$

We take Q^2 to represent the characteristic invariant-mass scale of the interacting constituent pair. Since the constituents are generally off shell inside the molecular folding integral, this scale is not uniquely fixed by on-shell kinematics. We therefore adopt the fixed-threshold prescription

$$Q^2_{\nu\nu'}=(m_\nu+m_{\nu'})^2 \tag{35}$$

and set $n_f=4$. These choices fully specify the coupling used in the present calculation. With the central parameters in Table II, the resulting values

$$\alpha_s(qq)=0.561838,\qquad \alpha_s(qc)=0.374074,$$
$$\alpha_s(c\bar{c})=0.304590 \tag{36}$$

provide direct numerical cross-checks; here q denotes either light constituent u or d.

Each external hadron state is factorized into normalized color, flavor, spin, and internal momentum-space factors,

$$\Psi_H=\chi_H^c\chi_H^f\chi_H^s\phi_H, \tag{37}$$

where $H\in\{A,B,M_f,B_f\}$ labels any external hadron in the transition $A+B\to M_f+B_f$. The internal S-wave functions ϕ_H are Gaussian. We use the same baryon widths $(\alpha_\rho,\alpha_\lambda^{(c)})$ for Σ_c and Λ_c, and the meson widths in Table II for both charge states. No parameter is fitted separately to the decay channels considered here. The normalized meson and baryon Gaussians, their mass-weighted relative and Jacobi momenta, and the topology-dependent baryon orderings are given in Appendix A 1. The internal functions ϕ_H must be distinguished from the molecular radial function $R_0(p)$ in Eq. (9): the former resolve the constituent

TABLE II. Constituent-model parameters and internal Gaussian widths used in the central QI calculation. The potential parameters and widths follow Ref. [18]; Eq. (35) and $n_f=4$ complete the running-coupling prescription used here.

Quantity	Value	Unit
$m_u=m_d$	0.334	GeV
$m_c=m_{\bar{c}}$	1.776	GeV
b	0.180	GeV^2
$\tau_{\rm hf}$	0.897	GeV
A_α	10.0	⋯
B_α	0.310	GeV
n_f	4	⋯
α_ρ	0.400	GeV
$\alpha_\lambda^{(c)}$	0.490	GeV
β_D	0.600	GeV
β_{D^*}	0.520	GeV

overlap inside the Born kernel, whereas the latter folds that kernel over the initial two-hadron molecule.

The internal and molecular Gaussians describe two distinct levels of the cluster approximation and are not eigenfunctions obtained from a single common Hamiltonian. The constituent-interaction parameters and the isolated-hadron widths in Table II are adopted together as the QI input set. The latter are phenomenological single-Gaussian representations of the hadrons: the meson widths are tied to isolated-meson size estimates, whereas the baryon widths follow the oscillator prescription in Eq. (A10). They are not exact solutions of the pairwise interaction in Eq. (33). In contrast, β_{P_c} is fixed independently from the binding energy through Eq. (13). Neither the QI rearrangement kernel nor the OPE transition kernel is iterated to generate the molecular bound state in the present first-Born treatment. Possible binding-induced modifications of the internal hadron wave functions are consequently neglected.

For the central inputs, Eq. (12) gives molecular rms separations of approximately 1.46, 0.90, and 1.97 fm for the $P_c(4312)$, $P_c(4440)$, and $P_c(4457)$, respectively. Applying the corresponding coordinate-space Gaussian conversion to the internal widths gives relative coordinate lengths of approximately 0.40 and 0.46 fm for the $\bar{D}$ and $\bar{D}^*$ mesons, and 0.49–0.60 fm for the baryon Jacobi variables. These quantities are Gaussian coordinate lengths rather than charge radii. The molecular coordinate is therefore more extended than the internal hadron coordinates, although the separation is only moderate for the more deeply bound $P_c(4440)$. This hierarchy supports the cluster factorization but should not be interpreted as a fully self-consistent five-body solution. The residual dependence on the two scales is probed in Table X by varying β_{P_c} and the internal meson and baryon widths independently; the resulting envelopes are reported in Table XI and Fig. 3.

C. Color, flavor, and spin factors

To expose how the constituent interaction enters each diagram, we write

$$V_{\nu\nu'} = \mathbf{t}_\nu \cdot \mathbf{t}_{\nu'} \sum_{X \in \{\mathrm{CL,HF}\}} v^X_{\nu\nu'}(q_{\nu\nu'}) \hat{O}_X,$$
$$\hat{O}_{\mathrm{CL}} = 1, \qquad \hat{O}_{\mathrm{HF}} = \mathbf{s}_\nu \cdot \mathbf{s}_{\nu'}. \tag{38}$$

Here v^{CL} contains the Coulomb and confinement terms, whereas v^{HF} contains the scalar coefficient and Gaussian smearing of the hyperfine term. For representation $r \in \{\mathrm{pr}, \mathrm{po}\}$, clustering $a \in \{14, 15\}$, and pair $\nu\nu' \in \mathcal{P}_{r,a}$, define

$$I^a_{C,r}(\nu\nu') = \langle \chi^c_{F_a} | \mathbf{t}_\nu \cdot \mathbf{t}_{\nu'} | \chi^c_{AB} \rangle, \tag{39}$$

$$I^a_F = \langle \chi^f_{F_a} | \chi^f_{AB} \rangle, \tag{40}$$

$$I^{a,J}_{S,X,r}(\nu\nu') = \langle \chi^{s;JM_J}_{F_a} | \hat{O}_X | \chi^{s;JM_J}_{AB} \rangle. \tag{41}$$

These matrix elements respectively carry the color, flavor, and spin dependence of a diagram; its momentum dependence resides in the spatial overlap introduced below. All states in Eqs. (39)–(41) are normalized and use the phase conventions of Sec. II A and Appendix A.

The color singlets are formed with $\delta_{ab}/\sqrt{3}$ for a meson and $\epsilon_{abc}/\sqrt{6}$ for a baryon. The final Λ_c contains an antisymmetric light-flavor pair. For the labeled states in Eqs. (25) and (26), its overlap with the initial charged flavor state is

$$I^{14}_F = I^{15}_F = \frac{1}{\sqrt{2}}. \tag{42}$$

The complete color and flavor factors are listed in Table III. Each color vector sums to zero. This color-singlet identity removes a constant interquark interaction and is used below in the distributional treatment of the confinement kernel.

The spin states are constructed in the Condon-Shortley convention. The u_4u_5 pair in the initial Σ_c has spin 1 and is coupled with the charm spin to $s_{\Sigma_c} = 1/2$, whereas the light pair in the final Λ_c has spin 0. The meson and baryon spins are subsequently coupled, in that order, to total J. Table IV gives the spin-independent overlap $I^{14,J}_{S,\mathrm{CL}}$ and the pair-dependent hyperfine factors for F_{14}. The F_{15} factors follow from $4 \leftrightarrow 5$ together with the pair reordering shown in Table III.

Together, Tables III and IV provide the complete algebraic input for the S-wave QI transitions. Explicit constituent states, phase conventions, and representative contractions are collected in Appendix A; no channel-dependent coupling is introduced.

We now combine these algebraic factors with the spatial matrix element. To include the prior-post average of Eq. (32) at the coefficient level, define

$$\kappa^{(J)}_{r,a,\nu\nu',X} = \frac{1}{2} I^a_{C,r}(\nu\nu') I^a_F I^{a,J}_{S,X,r}(\nu\nu'), \qquad \nu\nu' \in \mathcal{P}_{r,a}. \tag{43}$$

The kernel for one labeled clustering is then

TABLE III. Color and flavor factors for the labeled open-charm clusterings. Within each row, the entries of $\mathbf{I}_C$ follow the displayed ordered pair set. All entries are matrix elements of normalized states.

Set	Ordered pairs	$\mathbf{I}_C$	I_F
Prior, F_{14}	(13, 14, 15, 23, 24, 25)	$(2,-4,2,-2,4,-2)/9$	$1/\sqrt{2}$
Post, F_{14}	(13, 12, 15, 43, 42, 45)	$(2,-4,2,-2,4,-2)/9$	$1/\sqrt{2}$
Prior, F_{15}	(13, 14, 15, 23, 24, 25)	$(-2,-2,4,2,2,-4)/9$	$1/\sqrt{2}$
Post, F_{15}	(13, 12, 14, 53, 52, 54)	$(-2,4,-2,2,-4,2)/9$	$1/\sqrt{2}$

TABLE IV. Spin factors for clustering F_{14}. The prior vectors are ordered as (13, 14, 15, 23, 24, 25) and the post vectors as (13, 12, 15, 43, 42, 45). We use $\zeta = \sqrt{3}/24$. The two heavier peaks have the same factors for a fixed $\Sigma_c\bar{D}^*$ spin assignment. The table covers every S-wave transition evaluated in this work.

Transition	J	$I^{14,J}_{S,\mathrm{CL}}$	$\boldsymbol{I}^{14,J}_{S,\mathrm{HF,pr}}$	$\boldsymbol{I}^{14,J}_{S,\mathrm{HF,po}}$
$\Sigma_c\bar{D}\to\Lambda_c\bar{D}$	$\frac{1}{2}$	0	$(3\zeta, 0, 0, -3\zeta, 0, 0)$	$(3\zeta, 0, 0, -3\zeta, 0, 0)$
$\Sigma_c\bar{D}\to\Lambda_c\bar{D}^*$	$\frac{1}{2}$	$-\frac{1}{2}$	$(\frac{1}{4}, -\frac{1}{8}, -\frac{3}{8}, -\frac{1}{4}, \frac{1}{8}, \frac{3}{8})$	$(\frac{1}{4}, \frac{3}{8}, -\frac{3}{8}, \frac{1}{4}, \frac{1}{8}, -\frac{1}{8})$
$\Sigma_c\bar{D}^*\to\Lambda_c\bar{D}$	$\frac{1}{2}$	$-\frac{1}{2}$	$(-\frac{1}{4}, \frac{3}{8}, \frac{1}{8}, -\frac{1}{4}, \frac{1}{8}, \frac{3}{8})$	$(-\frac{1}{4}, -\frac{1}{8}, \frac{1}{8}, \frac{1}{4}, \frac{1}{8}, -\frac{1}{8})$
$\Sigma_c\bar{D}^*\to\Lambda_c\bar{D}^*$	$\frac{1}{2}$	$1/\sqrt{3}$	$(-\zeta, 2\zeta, -2\zeta, \zeta, -2\zeta, -6\zeta)$	$(-\zeta, 2\zeta, -2\zeta, -7\zeta, -2\zeta, 2\zeta)$
$\Sigma_c\bar{D}^*\to\Lambda_c\bar{D}^*$	$\frac{3}{2}$	$-1/(2\sqrt{3})$	$(-\zeta, -\zeta, \zeta, -5\zeta, \zeta, 3\zeta)$	$(-\zeta, -\zeta, \zeta, -\zeta, \zeta, -\zeta)$

$$V_a^{(J)}(k,p,u) = \sum_{r\in\{\mathrm{pr,po}\}} \sum_{\nu\nu'\in\mathcal{P}_{r,a}} \sum_{X\in\{\mathrm{CL,HF}\}} \kappa^{(J)}_{r,a,\nu\nu',X} \times I^{r,a,\nu\nu'}_{\mathrm{space},X}(k,p,u). \tag{44}$$

Equation (44) therefore assembles the separately evaluated color, flavor, spin, and spatial overlaps into the constituent-level Born kernel. Because the factor $1/2$ is already contained in $\kappa^{(J)}_{r,a,\nu\nu',X}$, no additional prior-post averaging factor is applied to Eq. (44).

For illustration, the coefficient of the prior 13 hyperfine diagram for F_{14} in $\Sigma_c\bar{D}\to\Lambda_c\bar{D}$ is

$$\kappa^{(1/2)}_{\mathrm{pr},14,13,\mathrm{HF}} = \frac{1}{2}\left(\frac{2}{9}\right)\left(\frac{1}{\sqrt{2}}\right)\left(\frac{\sqrt{3}}{8}\right) = \frac{\sqrt{6}}{144}. \tag{45}$$

This example also provides a direct check of the coefficient conventions and of the single prior-post averaging factor.

D. Spatial matrix elements and reduced kernel

For each ordered pair $\nu\nu'$, the remaining diagram dependence is carried by the internal momentum overlap. We choose the initial momenta $\mathbf{p}_3$ and $\mathbf{p}_4$ of constituents three and four as independent internal integration variables. For fixed external momenta $\mathbf{k}$ and $\mathbf{p}$, transferred momentum $\mathbf{q}_{\nu\nu'}$, ordered pair $\nu\nu'$, and clustering a, all other constituent momenta are fixed by momentum conservation and the momentum-transfer routing. Suppressing the resulting arguments of the four hadron wave functions, the spatial overlap takes the common form

$$I^{r,a,\nu\nu'}_{\mathrm{space},X}(\mathbf{k},\mathbf{p}) = \int d^3\, q_{\nu\nu'}\, d^3p_3 d^3p_4\, v^X_{\nu\nu'}(q_{\nu\nu'})\phi^*_{M_f}\phi^*_{B_f}\phi_A\phi_B. \tag{46}$$

The complete constituent-momentum routing and an explicit F_{14} example for the ordered pair 13 are given in Appendix B 1. The mass-weighted Jacobi momenta entering the hadron wave functions are defined in Appendix A 1. The integration measures in Eq. (46) follow the convention of Ref. [18]; no additional $(2\pi)^{-3}$ factor is inserted into the internal overlap.

Because the four internal hadron functions are Gaussian, all internal integrations for the hyperfine contribution can be performed analytically. For the Coulomb and confinement terms, the six components associated with $\mathbf{p}_3$ and $\mathbf{p}_4$ are integrated analytically, leaving a three-dimensional integral over the transferred momentum. After the complete color-flavor-spin weighted CL diagram sum has been assembled, denote its reduced form factor for representation r and clustering a by $\mathcal{F}^{(J)}_{r,a}(\mathbf{q})$. The linear-confinement contribution is then evaluated through the finite distributional combination

$$\int d^3q \frac{\mathcal{F}^{(J)}_{r,a}(\mathbf{q}) - \mathcal{F}^{(J)}_{r,a}(\mathbf{0})}{q^4}. \tag{47}$$

The subtraction is applied only after the complete color-weighted spin-independent sum is formed. At $\mathbf{q} = \mathbf{0}$, the pair form factors in a given representation reduce to a common overlap, while the corresponding color factors in Table III sum to zero. Consequently, the subtraction in Eq. (47) implements the regulated Fourier transform of the linear potential; it is not an adjustable infrared cutoff. The Gaussian reduction and distributional derivation are given in Appendix B, and the numerical convergence tests are reported in Appendix D.

In the normalization of Sec. II C, $[I_{\mathrm{space},X}] = [V^{(J)}_a] = \mathrm{GeV}^{-2}$, and the subsequent molecular fold gives $[T^{(J)}_{00,\mathrm{QI};fi}] = \mathrm{GeV}^{-1/2}$. The instantaneous constituent interaction and real Gaussian functions make the Born-order QI amplitudes real in the phase convention adopted here.

E. Antisymmetrization, isospin projection, and physical QI amplitude

Equation (44) still refers to one temporarily labeled clustering. We next combine F_{14} and F_{15} into the normalized asymptotic state and then reconstruct the physical $I = 1/2$ kernel. The two clusterings are labeled representations of the same final channel, not independent final

states. Fermionic antisymmetry of the identical u quarks requires

$$|F_{\rm AS}\rangle = \frac{|F_{14}\rangle - |F_{15}\rangle}{\sqrt{2}}. \tag{48}$$

Projection onto this state gives the kernel for the explicitly calculated charged initial component,

$$V^{(J)}_{\rm ch}(k,p,u) = \frac{V^{(J)}_{14}(k,p,u) - V^{(J)}_{15}(k,p,u)}{\sqrt{2}}. \tag{49}$$

To see the relative sign, let P_{45} exchange the identical light quarks. Then $|F_{15}\rangle = P_{45}|F_{14}\rangle$ and $P_{45}|AB;JM_J\rangle = -|AB;JM_J\rangle$. The isospin-symmetric constituent interaction is covariant under the same relabeling. The explicit color, flavor, spin, and spatial factors therefore satisfy, pointwise in (k,p,u),

$$V^{(J)}_{15} = -V^{(J)}_{14}, \qquad V^{(J)}_{\rm ch} = \sqrt{2}V^{(J)}_{14}. \tag{50}$$

The factor $1/\sqrt{2}$ in Eq. (48) normalizes the asymptotic fermionic state and is distinct from both the flavor overlap in Eq. (42) and the prior-post factor in Eq. (32). A creation-operator derivation and the scope of the asymptotic-state normalization are given in Appendix C.

Only $\Sigma_c^{++}D^{(*)-}\to\Lambda_c^+\bar{D}^{(*)0}$ is evaluated directly. The neutral initial component is reconstructed with the exact-isospin relation derived in Eq. (6). Applied to the unfolded QI kernels, it gives

$$V^{(J)}_{\rm neu}(k,p,u) = -\frac{V^{(J)}_{\rm ch}(k,p,u)}{\sqrt{2}},$$
$$V^{(J)}_{{\rm QI};fi}(k,p,u) = \sqrt{\frac{3}{2}}V^{(J)}_{\rm ch}(k,p,u). \tag{51}$$

Here $V^{(J)}_{{\rm QI};fi}$ is the short-range kernel between normalized physical $I=1/2$ channel states, and the suffix fi retains the final-initial ordering established in Sec. II C. Physical charged-neutral mass splittings enter only the molecular-scale and kinematic variations of Sec. V; they do not modify the exact-isospin projection in Eq. (51).

The QI contribution to the folded amplitude of Eq. (18) is therefore

$$T^{(J)}_{00,{\rm QI};fi}(k) = \int_0^\infty p^2\,dp\,R_0(p)\int_{-1}^1 du\,V^{(J)}_{{\rm QI};fi}(k,p,u)$$
$$= T^{(J)}_{00,{\rm CL};fi}(k) + T^{(J)}_{00,{\rm HF};fi}(k). \tag{52}$$

Both terms on the second line are in the physical $I=1/2$ normalization: $T^{(J)}_{00,{\rm CL};fi}$ contains the Coulomb and confinement pieces, and $T^{(J)}_{00,{\rm HF};fi}$ contains the smeared hyperfine piece. Thus, Eq. (52) completes the chain from the constituent Born diagrams to the short-range contribution in the common amplitude convention of Sec. II C. Its QI-only partial width follows by inserting $T^{(J)}_{00,{\rm QI};fi}$ into Eq. (23). Section IV next constructs the OPE contribution in the same normalization before the two mechanisms are combined coherently.

IV. LONG-RANGE ONE-PION-EXCHANGE CONTRIBUTION

The QI mechanism constructed in Sec. III describes a short-range rearrangement of the constituent quarks. We supplement it with the direct OPE transition

$$\Sigma_c\bar{D}^{(*)} \longrightarrow \Lambda_c\bar{D}^{(*)}, \tag{53}$$

which provides the leading chiral long-distance connection between these channels whenever both pion vertices are allowed. The OPE interaction is evaluated once at Born order and folded with the same molecular radial wave function $R_0(p)$ as the QI kernel. It is not iterated in a coupled-channel equation, and the complex-scaled resonance wave functions of Ref. [23] are not imported into the present calculation.

The construction proceeds as follows. We first obtain the spin-isospin reduced three-dimensional OPE potential from the chiral vertices and specify its channel phases. We then define the retarded energy transfer and treat the physical-sheet pion cut analytically. After separating the contactlike and pion-pole pieces, we convert the potential to the $T^{(J)}_{00;fi}$ normalization of Sec. II C and combine it coherently with $T^{(J)}_{00,{\rm QI};fi}$. The QI-only widths remain the central predictions; the OPE and QI + OPE results quantify the sensitivity to long-distance dynamics and to the relative matching of the two descriptions.

A. Chiral vertices and the direct OPE kernel

We follow the heavy-hadron chiral conventions of Ref. [23]. Only the axial interactions that generate the $\Sigma_c\Lambda_c\pi$ and $\bar{D}^{(*)}\bar{D}^{(*)}\pi$ vertices required by Eq. (53) are needed,

$$\mathcal{L}^{\rm int}_\pi = g_2{\rm Tr}(\bar{\psi}^\mu u_\mu B_1 + {\rm H.c.}) + g\langle\bar{\tilde{H}}\not{u}\gamma_5\tilde{H}\rangle, \tag{54}$$

where

$$u_\mu = -\frac{\tau^a\partial_\mu\pi^a}{2f_\pi} + \mathcal{O}(\pi^3). \tag{55}$$

Here π^a are the pion fields, τ^a are the Pauli matrices in $SU(2)$ flavor space, f_π is the pion decay constant, and $\not{u} \equiv \gamma^\mu u_\mu$. The symbol H.c. denotes the

Hermitian-conjugate interaction. The trace Tr acts in flavor space, whereas $\langle\cdots\rangle$ denotes a Dirac trace.

The isosinglet field B_1 contains the Λ_c. The spin-1/2 isotriplet B_3 and the spin-3/2 isotriplet $B_3^{*\mu}$, containing the Σ_c and Σ_c^* states, are combined into the heavy-quark-spin superfield

$$\psi^\mu = B_3^{*\mu} - \frac{1}{\sqrt{3}}(\gamma^\mu + v^\mu)\gamma_5 B_3, \tag{56}$$

where v^μ is the common heavy-hadron velocity, $v^2 = 1$, and $\bar{\psi}^\mu$ is the Dirac adjoint. The anticharmed pseudoscalar and vector mesons are collected in

$$\tilde{H} = (\tilde{P}^*_\mu \gamma^\mu + i\tilde{P}\gamma_5)\frac{1-\not{v}}{2}, \qquad \bar{\tilde{H}} = \gamma^0 \tilde{H}^\dagger \gamma^0. \tag{57}$$

In this convention, the $SU(2)$ antimeson doublets are

$$\tilde{P} = \begin{pmatrix} \bar{D}^0 \\ D^- \end{pmatrix}, \qquad \tilde{P}^*_\mu = \begin{pmatrix} \bar{D}^{*0} \\ D^{*-} \end{pmatrix}_\mu .$$

Expanding Eq. (54) produces the $\bar{D}\bar{D}^*\pi$ and $\bar{D}^*\bar{D}^*\pi$ vertices, but no leading-order $\bar{D}\,\bar{D}\,\pi$ axial vertex. This accounts for the vanishing $\Sigma_c\bar{D}\to\Lambda_c\bar{D}$ entry in Table VI.

Let the exchanged pion carry $q_\pi^\mu = (q_\pi^0, \mathbf{q}_\pi)$, with $\mathbf{q}_\pi = \mathbf{k} - \mathbf{p}$. Before the central reduction, the OPE interaction has the schematic spin-momentum structure

$$V_{1\pi} \propto -\frac{(\mathbf{S}_B\cdot\mathbf{q}_\pi)(\mathbf{S}_M\cdot\mathbf{q}_\pi)}{(q_\pi^0)^2 - \mathbf{q}_\pi^2 - m_\pi^2 + i0}, \tag{58}$$

where $\mathbf{S}_B$ and $\mathbf{S}_M$ are the transition-spin operators at the baryon and meson vertices. The present S-wave calculation retains the trace part of the momentum tensor,

$$q_{\pi i}q_{\pi j} = \frac{\delta_{ij}}{3}\mathbf{q}_\pi^2 + \left(q_{\pi i}q_{\pi j} - \frac{\delta_{ij}}{3}\mathbf{q}_\pi^2\right) \longrightarrow \frac{\delta_{ij}}{3}\mathbf{q}_\pi^2, \tag{59}$$

and omits the traceless tensor part.

For a transition $i\to f$, let $\hat{c}_{fi}^{(J)}$ denote the real, dimensionless channel coefficient after projection onto the physical $I = 1/2$ and definite-J basis. Its extraction from the coefficient matrices of Ref. [23], including the required rephasing, is given in Sec. IV B. In the three-dimensional potential normalization of that reference, the full central OPE kernel is

$$V^{[\mathrm{Lin}],J}_{\pi,\mathrm{full};fi}(k,p,u) = \frac{|g||g_2|\hat{c}_{fi}^{(J)}}{f_\pi^2}\frac{\mathbf{q}_\pi^2}{\mathbf{q}_\pi^2 + m_\pi^2 - [q_\pi^0(p,k)]^2 - i0} \times F_{\Lambda_\pi}(k,p), \tag{60}$$

where the relative-angle variable u was defined in Sec. II C, and

$$\mathbf{q}_\pi^2 = k^2 + p^2 - 2kpu,$$
$$F_{\Lambda_\pi}(k,p) = \exp\left[-\frac{k^2+p^2}{\Lambda_\pi^2}\right]. \tag{61}$$

The cutoff Λ_π distinguishes the OPE regulator from the other momentum scales in the calculation. The factor F_{Λ_π} is the single potential-level regulator used in Ref. [23]; it is not a vertex form factor and is therefore not squared. The coefficient $\hat{c}_{fi}^{(J)}$ already includes the component-field factors, the physical $I = 1/2$ projection, the spin recoupling, and the factor $1/3$ in Eq. (59). No additional isospin

TABLE V. OPE inputs used in the reference calculation. The pion mass is the charge average $(m_{\pi^0} + 2m_{\pi^\pm})/3$. The mass $M_{\Sigma_c}^{\mathrm{av}} \equiv M_B^{\mathrm{av}}$ is the same arithmetic charge average defined in Eq. (14).

Quantity	Value
$\lvert g\rvert$	0.59
$\lvert g_2\rvert$	1.04
f_π	0.092 GeV
m_π	0.138039 GeV
Λ_π	0.500 GeV
$M_{\Sigma_c}^{\mathrm{av}}$	2.453310 GeV

TABLE VI. OPE coefficients for the selected physical $I = 1/2$ transitions. The Lin entry identifies the corresponding matrix element in Ref. [23]. The next column gives its phase and numerical factor in that convention, and $\hat{c}_{fi}^{(J)}$ is the real reference-basis coefficient of Eq. (64). The $J = 3/2\to\Lambda_c\bar{D}$ channel is not an S-wave zero: its leading contribution has $L_f = 2$ and is outside the present truncation.

Initial	J	Final	Lin entry	$C_{fi}^{[\mathrm{Lin}],J}/(gg_2)$	$\hat{c}_{fi}^{(J)}$	Treatment
$\Sigma_c\bar{D}$	$\frac{1}{2}$	$\Lambda_c\bar{D}$	VI: C_{13}	0	0	no $\bar{D}\,\bar{D}\,\pi$ vertex
$\Sigma_c\bar{D}$	$\frac{1}{2}$	$\Lambda_c\bar{D}^*$	VI: C_{23}	$-i\sqrt{6}/12$	$+\sqrt{6}/12$	Retained
$\Sigma_c\bar{D}^*$	$\frac{1}{2}$	$\Lambda_c\bar{D}$	VI: C_{14}	$+i\sqrt{6}/12$	$+\sqrt{6}/12$	Retained
$\Sigma_c\bar{D}^*$	$\frac{1}{2}$	$\Lambda_c\bar{D}^*$	VI: C_{24}	$-\sqrt{2}/6$	$-\sqrt{2}/6$	Retained
$\Sigma_c\bar{D}^*$	$\frac{3}{2}$	$\Lambda_c\bar{D}$	—	—	—	$L_f = 2$; not calculated
$\Sigma_c\bar{D}^*$	$\frac{3}{2}$	$\Lambda_c\bar{D}^*$	VII: C_{13}	$+\sqrt{2}/12$	$+\sqrt{2}/12$	Retained

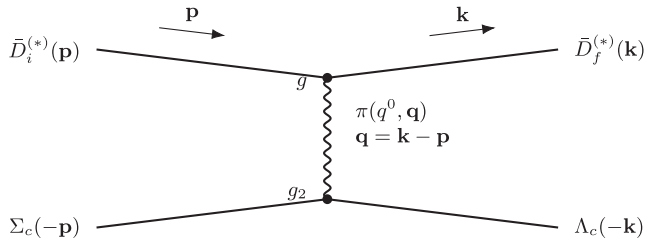


FIG. 2. Direct OPE transition $\Sigma_c \bar{D}_i^{(*)} \to \Lambda_c \bar{D}_f^{(*)}$. The initial meson and baryon carry momenta $\mathbf{p}$ and $-\mathbf{p}$, while the final pair carries $\mathbf{k}$ and $-\mathbf{k}$. Directing the pion momentum from the baryon line to the meson line gives $q_\pi^\mu = (q_\pi^0, \mathbf{k} - \mathbf{p})$. The physical $I = 1/2$ and definite-J projections are contained in $\hat{c}_{fi}^{(J)}$.

coefficient, spin factor, or central-reduction factor multiplies Eq. (60).

The reference inputs are collected in Table V. Coupling magnitudes are used here so that Eq. (60) defines a real reference basis before the pion cut is encountered. The remaining relative sign between the OPE and QI bases is treated explicitly in Sec. IV F.

Figure 2 shows the corresponding hadron-level Born topology. It is evaluated once and is distinct from the constituent rearrangement diagrams of Sec. III.

B. Channel coefficients and phase convention

Let $C_{fi}^{[\mathrm{Lin}],J}$ denote an entry of the OPE coefficient matrices in Tables VI and VII of Ref. [23], with the first suffix denoting the final channel and the second the initial channel. The numerical channel labels used in those matrices are quoted only to make the translation reproducible; they are unrelated to the constituent labels of Sec. III.

The off-diagonal $\bar{D} \leftrightarrow \bar{D}^*$ entries in the Lin basis contain conventional factors of i. We introduce a real reference basis by

$$|\bar{D}\rangle_{\mathrm{ref}} = i|\bar{D}\rangle_{[\mathrm{Lin}]}, \qquad |\bar{D}^*\rangle_{\mathrm{ref}} = |\bar{D}^*\rangle_{[\mathrm{Lin}]}. \tag{62}$$

More generally, if $|h\rangle_{\mathrm{ref}} = e^{i\phi_h}|h\rangle_{[\mathrm{Lin}]}$, then

$$C_{fi}^{[\mathrm{ref}],J} = e^{-i\phi_f} C_{fi}^{[\mathrm{Lin}],J} e^{i\phi_i}, \quad \phi_{\bar{D}} = \frac{\pi}{2}, \quad \phi_{\bar{D}^*} = 0. \tag{63}$$

The dimensionless coefficient used in Eq. (60) is therefore

$$\hat{c}_{fi}^{(J)} \equiv \frac{C_{fi}^{[\mathrm{ref}],J}}{|g||g_2|}. \tag{64}$$

This definition separates the channel-dependent spin, isospin, and phase factor from the common positive coupling magnitude.

Equations (62)–(64) convert both retained $\bar{D} \leftrightarrow \bar{D}^*$ coefficients to $+\sqrt{6}/12$ and leave the real diagonal-in-meson-spin entries unchanged. These coefficients already act between normalized physical $I = 1/2$ channel states. Consequently, the $\sqrt{3/2}$ charged-to-isospin factor used for the QI kernel in Eq. (51) is not applied again to OPE. The remaining relative phase between this reference chiral basis and the signed QI basis is kept explicit in the coherent matching.

C. Retarded energy transfer and the pion cut

In the molecular fold, p is integrated over the initial wave function, whereas k is fixed by the final two-body kinematics of Eq. (16). Our reference energy transfer follows the direct baryon-line routing in Fig. 2,

$$q_{\pi,\mathrm{dir}}^0(p,k) = E_{\Sigma_c}(p) - E_{\Lambda_c}(k), \qquad E_H(x) = \sqrt{M_H^2 + x^2}. \tag{65}$$

Here $M_{\Sigma_c} = M_{\Sigma_c}^{\mathrm{av}}$ from Table V, while M_{Λ_c} is the physical final baryon mass. Only $(q_\pi^0)^2$ enters Eq. (60); hence reversing the overall four-momentum direction assigned to the pion does not change the kernel.

To probe the off-shell continuation, we also consider

$$q_{\pi,\mathrm{swap}}^0(p,k) = E_{\Sigma_c}(k) - E_{\Lambda_c}(p), \qquad q_{\pi,\mathrm{stat}}^0 = 0. \tag{66}$$

The first diagnostic merely interchanges p and k in the baryon energy difference; it does not represent a crossed Feynman topology. These two choices are sensitivity prescriptions, not additional decay channels or statistical variations.

Retardation is important because the $\Sigma_c - \Lambda_c$ mass difference is comparable to m_π. For any chosen $q_\pi^0(p,k)$, define

$$\begin{aligned} &\Delta_\pi(p,k) = m_\pi^2 - [q_\pi^0(p,k)]^2, \\ &D_0(p,k) = p^2 + k^2 + \Delta_\pi(p,k), \quad D_1(p,k) = 2pk. \end{aligned} \tag{67}$$

The propagator denominator in Eq. (60) is then $D_0 - D_1 u - i0$. For $D_1 > 0$, a pole lies inside the angular integration interval when $|D_0| < D_1$. This is the on-shell-pion cut associated with the allowed three-body intermediate state. On the physical sheet, the required angular integral is

$$\begin{aligned} \mathcal{L}_\pi(p,k) &\equiv \int_{-1}^{1} \frac{du}{D_0 - D_1 u - i0} \\ &= \frac{1}{D_1} \ln\left|\frac{D_0 + D_1}{D_0 - D_1}\right| + i\frac{\pi}{D_1}\Theta(D_1 - |D_0|). \end{aligned} \tag{68}$$

Its continuous $D_1 \to 0$ limit is $\mathcal{L}_\pi = 2/(D_0 - i0)$. The positive imaginary part follows from $1/(x - i0) = PV(1/x) + i\pi\delta(x)$. Equation (68) is used directly, so no artificial finite width is introduced in the pion propagator.

The absorptive part generated by Eq. (68) is retained in the two-body Born amplitude. Because the kernel is not iterated and the three-body channel is not solved explicitly, this treatment is not a unitary three-body calculation and does not furnish a separate $\Lambda_c\bar{D}^{(*)}\pi$ partial width.

D. Contactlike and pion-pole pieces

The central numerator can be separated algebraically before the molecular fold. For finite $\epsilon > 0$,

$$\frac{\mathbf{q}_\pi^2}{\mathbf{q}_\pi^2+\Delta_\pi-i\epsilon} = 1-\frac{\Delta_\pi-i\epsilon}{\mathbf{q}_\pi^2+\Delta_\pi-i\epsilon} \xrightarrow[\epsilon\to 0^+]{} 1-\frac{\Delta_\pi}{\mathbf{q}_\pi^2+\Delta_\pi-i0}, \tag{69}$$

where the last equality is understood in the distributional sense. We label the resulting OPE prescriptions by $\xi \in \{\mathrm{ct}, \mathrm{pole}, \mathrm{full}\}$ and define

$$V^{[\mathrm{Lin}],J}_{\pi,\mathrm{ct};fi} = \frac{|g||g_2|\hat{c}^{(J)}_{fi}}{f_\pi^2} F_{\Lambda_\pi}(k,p), \tag{70}$$

$$V^{[\mathrm{Lin}],J}_{\pi,\mathrm{pole};fi} = -\frac{|g||g_2|\hat{c}^{(J)}_{fi}}{f_\pi^2}\frac{\Delta_\pi}{\mathbf{q}_\pi^2+\Delta_\pi-i0} F_{\Lambda_\pi}(k,p). \tag{71}$$

Thus $V^{[\mathrm{Lin}],J}_{\pi,\mathrm{full};fi} = V^{[\mathrm{Lin}],J}_{\pi,\mathrm{ct};fi} + V^{[\mathrm{Lin}],J}_{\pi,\mathrm{pole};fi}$. After integration over u, the three prescriptions are represented by

$$\begin{aligned} &\mathcal{K}_{\mathrm{ct}}(p,k) = 2, \qquad \mathcal{K}_{\mathrm{pole}}(p,k) = -\Delta_\pi\mathcal{L}_\pi, \\ &\mathcal{K}_{\mathrm{full}}(p,k) = 2-\Delta_\pi\mathcal{L}_\pi. \end{aligned} \tag{72}$$

The factor 2 in $\mathcal{K}_{\mathrm{ct}}$ is simply $\int_{-1}^{1} du$.

Because the QI kernel already provides a model of the predominantly short-distance rearrangement transition, directly adding the full regulated OPE kernel would risk double counting its contactlike short-range part. We therefore take the contact-subtracted pion-pole term as the reference exploratory OPE prescription and retain the full kernel only as a diagnostic of short-distance matching sensitivity. This subtraction removes the explicit momentum-independent term in Eq. (69), but it is not a microscopic matching condition. The QI constituent parameters and the OPE chiral couplings are fixed independently, and no common short-distance counterterm is fitted. Moreover, at finite Λ_π the separation is regulator dependent, and the retained pion-pole term can still overlap with QI at intermediate momenta. The coherent QI-OPE widths should therefore be interpreted as regulator- and prescription-dependent matching-sensitivity scenarios rather than unique hybrid predictions. A systematic treatment of double counting would require a common regulator-consistent coupled-channel framework in which the short-distance operators and OPE are matched simultaneously, including the counterterms associated with tensor-induced S-D mixing [14].

The present Born calculation retains only the central $L_i = L_f = 0$ projection. Tensor OPE, OPE iteration, S-D mixing, and the physical $L_i = 0 \to L_f = 2$ transition $\Sigma_c\bar{D}^*(J=3/2)\to\Lambda_c\bar{D}$ are outside this truncation. The last decay is therefore uncalculated rather than forbidden.

E. Normalization bridge and molecular fold

Equations (69), (70), and (71) have so far carried the plane-wave normalization of Ref. [23]. We now convert them to the $T^{(J)}_{00;fi}$ convention fixed in Sec. II C. To avoid confusing a normalization label with orbital angular momentum, we use [Lin] and [pres] for the two conventions.

The plane-wave states satisfy

$$\begin{aligned} {}_{[\mathrm{Lin}]}\langle\mathbf{p}'|\mathbf{p}\rangle_{[\mathrm{Lin}]} &= (2\pi)^3\delta^3(\mathbf{p}'-\mathbf{p}), \\ {}_{[\mathrm{pres}]}\langle\mathbf{p}'|\mathbf{p}\rangle_{[\mathrm{pres}]} &= \delta^3(\mathbf{p}'-\mathbf{p}). \end{aligned} \tag{73}$$

Consequently,

$$|\mathbf{p}\rangle_{[\mathrm{pres}]} = (2\pi)^{-3/2}|\mathbf{p}\rangle_{[\mathrm{Lin}]}, \qquad V^{[\mathrm{pres}]} = (2\pi)^{-3}V^{[\mathrm{Lin}]}. \tag{74}$$

For the same normalized state, the corresponding radial functions obey

$$\int_0^\infty \frac{p^2dp}{(2\pi)^3}|\phi^{[\mathrm{Lin}]}_\ell(p)|^2 = 1, \phi^{[\mathrm{Lin}]}_\ell(p) = (2\pi)^{3/2}R_\ell(p). \tag{75}$$

For the molecular S wave, R_ℓ reduces to the R_0 of Eq. (9).

For a rotationally invariant scalar potential and normalized spherical harmonics, the Funk–Hecke relation gives

$$\begin{aligned} &\int d\Omega_p V^{[\mathrm{Lin}]}(k,p,u)Y_{\ell m}(\hat{\mathbf{p}}) \\ &= 2\pi Y_{\ell m}(\hat{\mathbf{k}})\int_{-1}^{1} du\, P_\ell(u)V^{[\mathrm{Lin}]}(k,p,u). \end{aligned} \tag{76}$$

Combining Eqs. (74)–(76) for $\ell = 0$ yields the polarization-resolved OPE amplitude in the present convention,

$$\mathcal{T}^{[\mathrm{pres}]}_{\pi;fi;M_J;m_Mm_B}(\mathbf{k}) = \frac{Y_{00}(\hat{\mathbf{k}})}{(2\pi)^2}\langle s_Mm_M, s_Bm_B|JM_J\rangle\left\{\int_0^\infty p^2dp\, R_0(p)\int_{-1}^{1} du V^{[\mathrm{Lin}],J}_{\pi,\xi;fi}(k,p,u)\right\}. \tag{77}$$

Comparison with Eq. (19) identifies the expression in braces as $T^{(J)}_{00,\pi,\xi;fi}(k)$. Thus, although the state-level matrix elements in Eq. (74) differ by $(2\pi)^{-3}$, the radial-state and partial-wave factors compensate so that the Lin three-dimensional potential appears directly under the braces in Eq. (77).

The same result can be expressed through a generic partial wave. Define

$$G^{[\mathrm{Lin}]}_{\ell}(k) \equiv \int_0^\infty \frac{p^2 dp}{(2\pi)^3} V^{[\mathrm{Lin}]}_{\ell}(k,p)\phi^{[\mathrm{Lin}]}_{\ell}(p) = \frac{1}{\sqrt{2\pi}} T^{[\mathrm{pres}]}_{\ell}(k),$$
$$V^{[\mathrm{Lin}]}_{\ell}(k,p) = 2\pi \int_{-1}^{1} du P_\ell(u) V^{[\mathrm{Lin}]}(k,p,u). \tag{78}$$

If μ_f denotes the reduced mass of the final two-hadron channel, the nonrelativistic expression $\mu_f k|G^{[\mathrm{Lin}]}_{\ell}|^2/(4\pi^2)$ becomes $\mu_f k|T^{[\mathrm{pres}]}_{\ell}|^2/(2\pi)^3$. The relativistic replacement $\mu_f \to E_{M_f} E_{B_f}/M_{P_c}$ then reproduces the width convention of Eq. (23).

Reference [23] relates its heavy-hadron chiral Feynman amplitude to the nonrelativistic potential through $V^{[\mathrm{Lin}]} = -\mathcal{M}^{[\mathrm{Lin}]}_{\mathrm{HH}\chi\mathrm{PT}}/4$. That conversion is already contained in Eq. (60); the factor $-1/4$ and the external heavy-field normalizations must not be applied again. The chiral amplitude $\mathcal{M}^{[\mathrm{Lin}]}_{\mathrm{HH}\chi\mathrm{PT}}$ is distinct from the relativistic decay amplitude $\mathcal{M}_{fi}$ defined in Eq. (20). Similarly, Eqs. (59), (64), and (77) show why no additional factor of $1/3$, $\sqrt{3/2}$, 2π, or $(2\pi)^3$ is inserted.

Using the angular functions in Eq. (72), the OPE contribution in the common present convention is therefore

$$T^{(J)}_{00,\pi,\xi;fi}(k) = \frac{|g||g_2|\hat{c}^{(J)}_{fi}}{f_\pi^2} \int_0^\infty dp\, p^2 R_0(p) F_{\Lambda_\pi}(k,p) \times \mathcal{K}_\xi(p,k), \xi \in \{\mathrm{ct}, \mathrm{pole}, \mathrm{full}\}. \tag{79}$$

The reference-sign OPE amplitude used in the coherent matching is

$$T^{(J)}_{00,\pi,\mathrm{ref};fi}(k) \equiv T^{(J)}_{00,\pi,\mathrm{pole};fi}(k). \tag{80}$$

Equation (79) is the endpoint of the normalization bridge: $T^{(J)}_{00,\pi,\xi;fi}$ now has the same normalization as the QI amplitude and a fixed real reference-channel phase convention. Only its overall sign relative to the independently constructed QI basis remains to be matched.

The logarithmic endpoint singularities in Eq. (68) are integrable. Their numerical treatment and the radial cutoff are specified in Sec. V B, with convergence tests in Appendix D. In the conventions used here, $[V_\pi] = \mathrm{GeV}^{-2}$, $[R_0] = \mathrm{GeV}^{-3/2}$, and $[T^{(J)}_{00,\pi}] = \mathrm{GeV}^{-1/2}$, as required by Eq. (23). The complex-scaled channel wave functions and their c-product normalization play no role in this Gaussian Born fold.

F. Coherent matching to quark interchange

The QI and OPE mechanisms feed the same asymptotic two-body channel and must therefore be combined at the amplitude level. The rephasing in Sec. IV B fixes the relative phases among the OPE channels, but it does not by itself determine the overall phase of the chiral heavy-hadron basis relative to the independently constructed QI basis. We parametrize this remaining correlated ambiguity by one sign,

$$T^{(J)}_{00,\mathrm{tot};fi}(k;\eta_{\mathrm{match}}) = T^{(J)}_{00,\mathrm{QI};fi}(k) + \eta_{\mathrm{match}} T^{(J)}_{00,\pi,\mathrm{ref};fi}(k),$$
$$\eta_{\mathrm{match}} = \pm 1. \tag{81}$$

Equation (81) is a correlated matching ansatz, not a relative sign derived from either model separately. Within a reported branch, the same η_{match} is therefore used for every decay channel; it is not selected channel by channel. The two branches are not statistical limits and are not averaged.

The factor η_{match} parameterizes only the unresolved global relative phase between the two amplitude conventions; it does not remove or quantify the residual short-distance overlap discussed in Sec. IV D.

Using the phase-space factor ρ_{fi} defined in Eq. (23), the separate mechanism widths are

$$\Gamma^{(J)}_{\mathrm{QI};fi} = \rho_{fi}|T^{(J)}_{00,\mathrm{QI};fi}|^2, \quad \Gamma^{(J)}_{\pi,\mathrm{ref};fi} = \rho_{fi}|T^{(J)}_{00,\pi,\mathrm{ref};fi}|^2. \tag{82}$$

The coherent total width is

$$\Gamma^{(J)}_{\mathrm{tot};fi}(\eta_{\mathrm{match}}) = \Gamma^{(J)}_{\mathrm{QI};fi} + \Gamma^{(J)}_{\pi,\mathrm{ref};fi} + 2\eta_{\mathrm{match}}\rho_{fi}\mathrm{Re}[T^{(J)}_{00,\mathrm{QI};fi} T^{(J)*}_{00,\pi,\mathrm{ref};fi}],$$
$$\Gamma^{(J)}_{\pm;fi} \equiv \Gamma^{(J)}_{\mathrm{tot};fi}(\eta_{\mathrm{match}} = \pm 1). \tag{83}$$

Thus, the separately quoted QI and OPE widths are not added incoherently. Fixing which correlated branch is realized requires a signed microscopic matching of the quark-model states to the chiral heavy-hadron fields, or an interference-sensitive observable. Until such information is available, we report both Γ_+ and Γ_- alongside the QI-only central results. The numerical inputs, integration settings, and stability tests used for all three amplitudes are given in Sec. V.

V. NUMERICAL INPUTS, EVALUATION, AND VALIDATION

This Section completes the setup needed for the results. We first list the physical masses and the molecular scales derived from the prescription of Sec. II B. We then specify the numerical integration settings, summarize the algebraic

TABLE VII. Hadron masses used in the reference calculation.

Hadron	M_H (GeV)
$P_c(4312)^+$	4.31190
$P_c(4440)^+$	4.44030
$P_c(4457)^+$	4.45730
$\bar{D}^0$	1.86484
D^-	1.86966
$\bar{D}^{*0}$	2.00685
D^{*-}	2.01026
Σ_c^+	2.45265
Σ_c^{++}	2.45397
Λ_c^+	2.28646

and convergence checks, and define the model-variation scenarios used to assess the stability of the predicted width hierarchies. Unless stated otherwise, all dimensionful inputs are given in GeV. No parameter is fitted to the selected $\Lambda_c\bar{D}^{(*)}$ partial widths. The QI and OPE interaction parameters already given in Tables II and V, respectively, are not repeated here.

A. Hadron masses and derived molecular scales

The reference masses are collected in Table VII. We use the central LHCb peak masses for the three P_c states [9] and the conventional-hadron masses from the Particle Data Group [40]. Experimental mass uncertainties are not propagated as statistical errors, because the uncertainty of the calculation is dominated by the molecular and interaction-model assumptions. The effect of choosing the neutral, averaged, or charged molecular threshold is instead examined explicitly in Sec. V D.

For the reference molecular calculation, the masses in Eq. (11) are the arithmetic charge averages M_A^{av} and M_B^{av} defined in Eq. (14). Thus $E_{\mathrm{bind}} = \bar{M}_{\mathrm{th}}^{D^{(*)}} - M_{P_c}$, $\mu_{AB} = \mu_{AB}^{\mathrm{av}}$, and Eq. (13) fixes β_{P_c}. The resulting thresholds, binding energies, Gaussian widths, and final-state momenta are listed in Table VIII. The momenta are obtained from Eq. (16) using the physical masses of $\Lambda_c^+\bar{D}^0$ or $\Lambda_c^+\bar{D}^{*0}$ in the final charge channel.

At a fixed peak mass, the $J = 1/2$ and $J = 3/2$ $\Sigma_c\bar{D}^*$ assignments therefore have identical kinematics and differ only through their spin-dependent transition kernels. The particularly small reference binding energy of $P_c(4457)$ also explains why its molecular width is most sensitive to the charged–neutral threshold prescription.

B. Numerical evaluation and reference settings

The QI amplitude in Eq. (52) is evaluated with Gauss-Legendre quadrature in the initial relative momentum p and the external angular variable $u = \hat{\mathbf{k}} \cdot \hat{\mathbf{p}}$. After the analytic Gaussian reduction described in Sec. III D, the remaining Coulomb-plus-confinement integral is evaluated in the magnitude $q = |\mathbf{q}|$, the polar-angle cosine $u_q \equiv \cos\theta_q$, and the azimuthal angle ϕ_q. We use Gauss-Legendre quadrature for q and u_q and a uniform periodic sum for ϕ_q. The Gaussian-smeared hyperfine contribution is evaluated after its internal momentum integrations have been carried out analytically.

For OPE, the u integration is performed analytically through Eq. (68). The remaining radial domain is partitioned at the logarithmic endpoint singularities. Each pole-separated interval is mapped with the $\sin^2$ transformation given in Appendix D 2 and evaluated with Gauss-Legendre quadrature. The endpoint conditions are first bracketed on a uniform scan and then refined before the integration. Table IX lists the reference settings for both mechanisms.

C. Algebraic consistency and numerical convergence

We distinguish exact consistency relations from convergence of the remaining numerical integrations. In the QI sector, the initial and final color and spin states are normalized, both labeled rearrangement topologies have flavor overlap $1/\sqrt{2}$, and the explicit color-flavor-spin construction reproduces the coefficient $\sqrt{6}/144$ in Eq. (45). The two labeled final clusterings satisfy Eq. (50) pointwise in (k, p, u) before the molecular fold. The subsequent antisymmetrization and exact-isospin reconstruction yield Eq. (51); the neutral initial charge component is therefore not evaluated independently.

In the OPE sector, the five S-wave coefficients used here agree with Tables VI and VII of Ref. [23] after the rephasing in Eq. (62). The contact-pole relation (69) is satisfied in the distributional limit $\epsilon \to 0^+$, and an independent delta-function evaluation reproduces the absorptive part implied by Eq. (68). The same global value of η_{match} is used in every channel, as required by Eq. (81). These are algebraic or convention-level checks and are independent of the quadrature orders.

TABLE VIII. Reference molecular scales and final-state momenta. The averaged thresholds and reduced masses are defined in Eq. (14); E_{bind} and β_{P_c} then follow from Eqs. (11) and (13). The final-state momenta use the physical $\bar{D}^0$ and $\bar{D}^{*0}$ masses.

Assignment	$\bar{M}_{\mathrm{th}}$ (GeV)	E_{bind} (MeV)	β_{P_c} (GeV)	$k_{\Lambda_c\bar{D}}$ (GeV)	$k_{\Lambda_c\bar{D}^*}$ (GeV)
$P_c(4312):\Sigma_c\bar{D}, J=\frac{1}{2}$	4.320560	8.660	0.165969	0.580128	0.199561
$P_c(4440):\Sigma_c\bar{D}^*, J=\frac{1}{2},\frac{3}{2}$	4.461865	21.565	0.267298	0.784313	0.565390
$P_c(4457):\Sigma_c\bar{D}^*, J=\frac{1}{2},\frac{3}{2}$	4.461865	4.565	0.122982	0.807877	0.597780

TABLE IX. Reference numerical settings. The orders N_p and N_u refer to the QI molecular fold; N_q, N_{u_q}, and N_ϕ refer to the remaining Coulomb-plus-confinement integral. The order N_π is used on each pole-separated OPE interval.

Setting	Reference value
(N_p, N_u)	(20,16)
$p_{\max}^{\mathrm{QI}}$	1.6 GeV
(N_q, N_{u_q}, N_ϕ)	(24,12,12)
$q_{\max}$	4.0 GeV
$p_{\max}^{\pi}$	2.0 GeV
Endpoint-bracketing scan	2000 subintervals
N_π per pole-separated interval	64

The convergence tests show that the numerical uncertainty is negligible on the scale of the model variations. Raising the QI orders from $(N_p, N_u; N_q, N_{u_q}, N_\phi) = (20, 16; 24, 12, 12)$ to $(28, 22; 32, 16, 16)$ changes the most sensitive calculated width by only $9.42 \times 10^{-5}\%$. For the reference $P_c(4312) \to \Lambda_c \bar{D}^*$ pion-pole amplitude with $q^0_{\pi,\mathrm{dir}}$ and $\Lambda_\pi = 0.50$ GeV, increasing N_π from 64 to 128 changes the complex amplitude by 9.83×10^{-8} GeV$^{-1/2}$. Extending $p_{\max}^{\pi}$ from 2 to 3 GeV at $N_\pi = 256$ changes it by 1.84×10^{-10} GeV$^{-1/2}$. Appendix D gives the channel-by-channel QI comparison, the OPE endpoint analysis, and the complex amplitudes entering these tests.

D. Reference prescriptions and model-variation scenarios

The convergence tests above quantify numerical errors; they do not measure the uncertainty associated with the physical and modeling assumptions. Table X defines the variations used for that second purpose. In the QI sector, one of eight input groups is varied at a time while all other inputs remain at their reference values. Each group is evaluated at a lower, reference, and upper choice, giving the 24 entries used to construct the scenario envelopes in Sec. VI. Repeated reference entries are retained in this count. The variations are not assigned probability distributions and are not combined in quadrature.

The OPE scenarios separately probe the regulator cutoff, the off-shell energy-transfer prescription, and the treatment of the short-distance part of the regulated interaction. Finally, $\eta_{\mathrm{match}} = +1$ and -1 define two globally correlated QI-OPE matching branches. Neither branch is selected as the preferred sign, and the sign is never chosen separately for different channels.

Finite Σ_c and $\bar{D}^*$ widths are not included. Their possible smearing of the pion cut, together with tensor OPE, OPE iteration, and S-D mixing, lies beyond the present first-Born, central-S-wave treatment. With the reference inputs, numerical accuracy, and model scenarios now specified, Sec. VI presents the central QI predictions and the exploratory coherent QI-OPE branches.

VI. RESULTS AND DISCUSSION

With the transition amplitudes, numerical settings, and model-variation scenarios now specified, we turn to the predicted decay patterns. We first present the QI amplitudes and partial widths, which constitute the central results of this work. We then test the stability of their channel and spin hierarchies, examine OPE through the matching scenarios defined in Secs. IV F and V D, and compare the resulting patterns with other open-charm calculations.

All amplitudes quoted below are the physical $I = 1/2$, molecularly folded S-wave amplitudes of Sec. II C. The channel labels and on-shell momentum argument are suppressed in tables only after the relevant initial and final states have been specified. For $J = 3/2 \to \Lambda_c \bar{D}$, angular-momentum and parity conservation require $L_f = 2$. Those two D-wave transitions are outside the central-S-wave treatment adopted here; an entry marked "not calculated" must therefore not be interpreted as a vanishing width.

TABLE X. Reference prescriptions and one-at-a-time model-variation choices. These alternatives define model scenarios rather than statistical confidence intervals. The two values of η_{match} are globally correlated matching branches.

Sector	Ingredient	Reference choice	Alternative choices
QI	Molecular constituent masses	$(M_A^{\mathrm{av}}, M_B^{\mathrm{av}})$ from Eq. (14)	neutral or charged constituent masses
QI	Molecular width	β_{P_c} from Eq. (13)	$0.9\beta_{P_c}$ and $1.1\beta_{P_c}$
QI	Meson oscillator widths	(β_D, β_{D^*}) in Table II	common factors 0.9 and 1.1
QI	Baryon oscillator widths	$(\alpha_\rho, \alpha_\lambda^{(c)})$ in Table II	common factors 0.9 and 1.1
QI	Light constituent mass	m_q in Table II	$0.95m_q$ and $1.05m_q$
QI	Charm constituent mass	m_c in Table II	$0.95m_c$ and $1.05m_c$
QI	String tension	b in Table II	$0.9b$ and $1.1b$
QI	Hyperfine smearing	τ_{hf} in Table II	$0.9\tau_{\mathrm{hf}}$ and $1.1\tau_{\mathrm{hf}}$
OPE	Regulator cutoff	$\Lambda_\pi = 0.50$ GeV	$0.40 \le \Lambda_\pi \le 1.00$ GeV in 0.10 GeV steps
OPE	Energy transfer	$q^0_{\pi,\mathrm{dir}}$	$q^0_{\pi,\mathrm{swap}}$ and $q^0_{\pi,\mathrm{stat}}$
OPE	Short-distance treatment	$\xi =$ pole	$\xi =$ full
QI–OPE	Relative matching sign	no preferred branch	$\eta_{\mathrm{match}} = +1$ and -1, globally

A. Central quark-interchange results

The reference QI amplitudes and partial widths are collected in Table XI. For each row, $T^{(J)}_{00,\mathrm{CL}}$ and $T^{(J)}_{00,\mathrm{HF}}$ abbreviate the channel-specific amplitudes $T^{(J)}_{00,\mathrm{CL};fi}(k)$ and $T^{(J)}_{00,\mathrm{HF};fi}(k)$ defined in Eq. (52); hence $T^{(J)}_{00,\mathrm{QI}} = T^{(J)}_{00,\mathrm{CL}} + T^{(J)}_{00,\mathrm{HF}}$. All three amplitudes are in the common convention of Sec. II C and are real in the adopted phase convention. The range accompanying each width is the minimum-to-maximum envelope of the 24 QI scenarios defined in Table X, not a statistical confidence interval.

The two calculated $P_c(4312)$ channels illustrate the origin of the main hierarchy. In the transition $\Sigma_c\bar{D}\to\Lambda_c\bar{D}$, the Coulomb-plus-confinement contribution vanishes, leaving the small width to be generated entirely by the hyperfine interaction. For $\Sigma_c\bar{D}\to\Lambda_c\bar{D}^*$, the Coulomb-plus-confinement amplitude is large and is only moderately reduced by destructive interference with the hyperfine term. Consequently,

$$\frac{\Gamma_{\mathrm{QI}}[P_c(4312)\to\Lambda_c\bar{D}^*]}{\Gamma_{\mathrm{QI}}[P_c(4312)\to\Lambda_c\bar{D}]} = 260.6. \tag{84}$$

For the $J = 1/2$ $\Sigma_c\bar{D}^*$ assignments, the analogous $\Lambda_c\bar{D}^*$-to-$\Lambda_c\bar{D}$ ratios are 13.73 at the $P_c(4440)$ mass and 76.53 at the $P_c(4457)$ mass. The latter value is enhanced by the cancellation $0.05309 - 0.03596 = 0.01712$ in the $\Lambda_c\bar{D}$ amplitude and should not be interpreted as a symmetry-protected prediction.

This distinction becomes transparent in the HQSS limit. Before phase-space corrections, Voloshin obtained the spin-recoupling relation [15]

$$\frac{\Gamma(\Sigma_c\bar{D}^*, J = 1/2\to\Lambda_c\bar{D}^*)}{\Gamma(\Sigma_c\bar{D}^*, J = 1/2\to\Lambda_c\bar{D})} = \frac{4}{3}. \tag{85}$$

As an internal limit check, making the D and D^* masses and Gaussian widths degenerate and removing the spin-dependent interaction gives

$$\left|\frac{T_{00,\mathrm{CL}}(\Lambda_c\bar{D}^*)}{T_{00,\mathrm{CL}}(\Lambda_c\bar{D})}\right|^2 = \frac{4}{3}.$$

The substantially larger physical ratios in Table XI therefore arise from unequal spatial overlaps, the hyperfine contribution, and channel-dependent cancellations. Likewise, the small but nonzero $P_c(4312)\to\Lambda_c\bar{D}$ width is a spin-dependent correction to the leading HQSS suppression.

For the three calculated $J = 1/2$ assignments, the relative share of the two selected open-charm modes can be summarized by the conditional fraction

$$\mathcal{F}^{(\bar{D},\bar{D}^*)}_{\bar{D}^*} \equiv \frac{\Gamma_{\mathrm{QI}}(\Lambda_c\bar{D}^*)}{\Gamma_{\mathrm{QI}}(\Lambda_c\bar{D}) + \Gamma_{\mathrm{QI}}(\Lambda_c\bar{D}^*)}. \tag{86}$$

The reference values are 99.62%, 93.21%, and 98.71% for $P_c(4312)$, $P_c(4440, J = 1/2)$, and $P_c(4457, J = 1/2)$, respectively. These are conditional two-channel fractions, not inclusive branching fractions: hidden-charm, $\Sigma_c^{(*)}\bar{D}^{(*)}$, and three-body modes are not included in the denominator.

B. Stability of the QI hierarchies

Figure 3 summarizes the 24 QI scenarios. Absolute widths vary appreciably, particularly when the reference amplitude is small because of cancellation. To display the correlated ratios compactly, define

$$\Gamma^{\mathrm{QI}}_{n,J}(f) \equiv \Gamma^{(J)}_{\mathrm{QI};fi} \quad \text{for } i = P_c(n),$$

where $n \in \{4312, 4440, 4457\}$ and f is the final channel named in the argument. Within each one-at-a-time scenario,

TABLE XI. Reference QI amplitudes and partial widths obtained with the averaged molecular thresholds and the inputs of Sec. V. Amplitudes are in $\mathrm{GeV}^{-1/2}$ and widths are in MeV. The parenthetical interval in the last column is the minimum-to-maximum envelope of the 24 one-at-a-time QI scenarios.

Initial state	J	Final state	$T^{(J)}_{00,\mathrm{CL}}$	$T^{(J)}_{00,\mathrm{HF}}$	$T^{(J)}_{00,\mathrm{QI}}$	$\Gamma^{(J)}_{\mathrm{QI}}$ (scenario range)
$P_c(4312)$	$\frac{1}{2}$	$\Lambda_c\bar{D}$	0	−0.033759	−0.033759	0.002848(0.001537 − 0.004318)
$P_c(4312)$	$\frac{1}{2}$	$\Lambda_c\bar{D}^*$	1.067412	−0.140435	0.926978	0.742111(0.398344 − 1.345232)
$P_c(4440)$	$\frac{1}{2}$	$\Lambda_c\bar{D}$	0.215196	−0.113425	0.101771	0.036067(0.012826 − 0.065088)
$P_c(4440)$	$\frac{1}{2}$	$\Lambda_c\bar{D}^*$	−0.916089	0.472811	−0.443278	0.495335(0.212903 − 0.899050)
$P_c(4440)$	$\frac{3}{2}$	$\Lambda_c\bar{D}$			D wave not calculated	
$P_c(4440)$	$\frac{3}{2}$	$\Lambda_c\bar{D}^*$	0.458044	−0.324335	0.133709	0.045068(0.010919 − 0.103664)
$P_c(4457)$	$\frac{1}{2}$	$\Lambda_c\bar{D}$	0.053088	−0.035964	0.017124	0.001056(0.000016 − 0.004277)
$P_c(4457)$	$\frac{1}{2}$	$\Lambda_c\bar{D}^*$	−0.341078	0.167280	−0.173798	0.080820(0.030208 − 0.141703)
$P_c(4457)$	$\frac{3}{2}$	$\Lambda_c\bar{D}$			D wave not calculated	
$P_c(4457)$	$\frac{3}{2}$	$\Lambda_c\bar{D}^*$	0.170539	−0.114254	0.056285	0.008477(0.002569 − 0.017729)

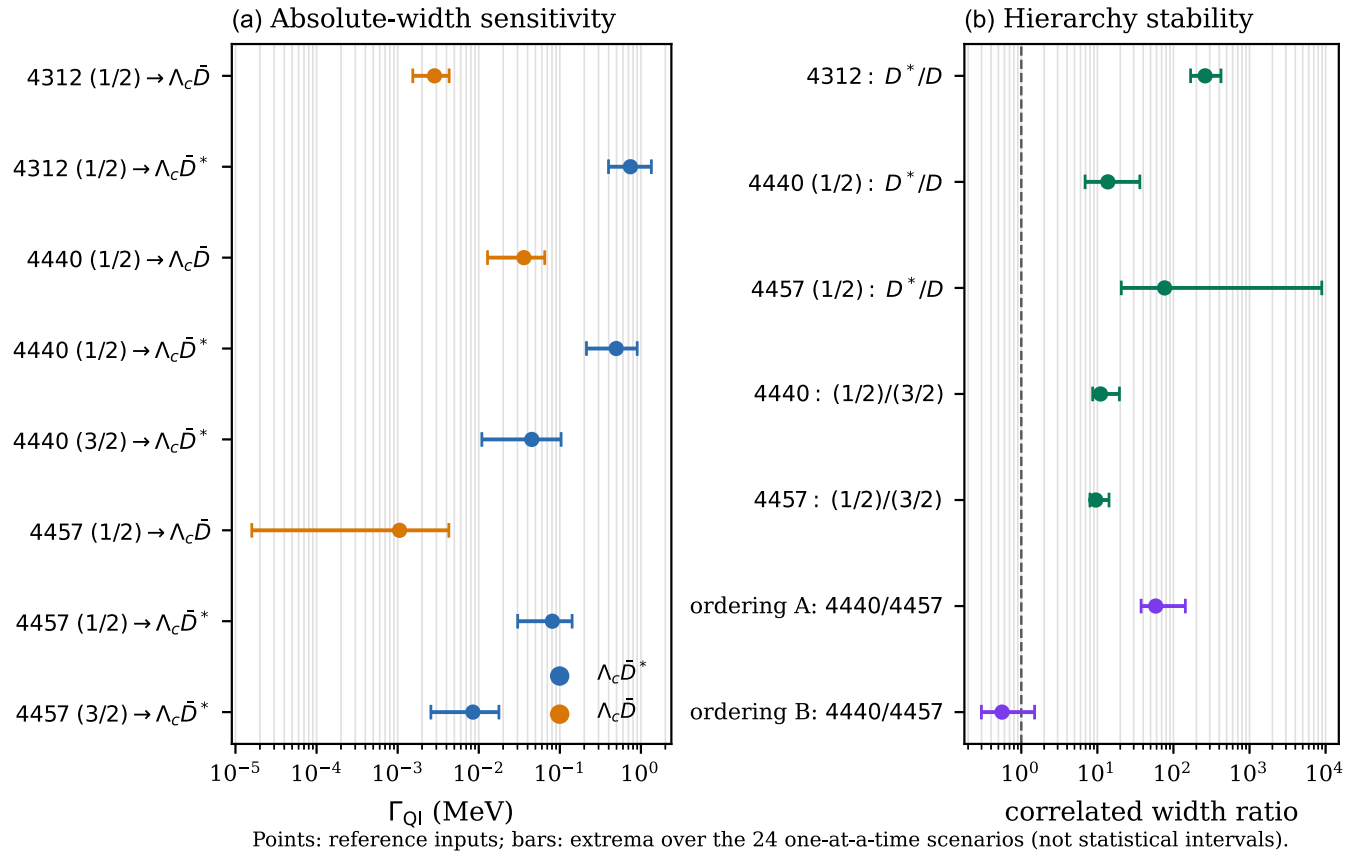


FIG. 3. Stability of the QI results over the 24 one-at-a-time scenarios of Table X. Points show the reference inputs, and horizontal bars span the corresponding minimum and maximum. Panel (a) gives the eight calculated S-wave widths. Panel (b) gives correlated width ratios, with the vertical dashed line marking unity. The bars are model-scenario envelopes, not statistical error intervals.

the same varied input is used in the numerator and denominator. The channel ratios then satisfy

$$\begin{aligned} 168.0 &\le \frac{\Gamma^{\mathrm{QI}}_{4312,1/2}(\Lambda_c\bar{D}^*)}{\Gamma^{\mathrm{QI}}_{4312,1/2}(\Lambda_c\bar{D})} \le 421.6, \\ 6.90 &\le \frac{\Gamma^{\mathrm{QI}}_{4440,1/2}(\Lambda_c\bar{D}^*)}{\Gamma^{\mathrm{QI}}_{4440,1/2}(\Lambda_c\bar{D})} \le 36.15, \\ 20.61 &\le \frac{\Gamma^{\mathrm{QI}}_{4457,1/2}(\Lambda_c\bar{D}^*)}{\Gamma^{\mathrm{QI}}_{4457,1/2}(\Lambda_c\bar{D})} \le 8912.4. \end{aligned} \tag{87}$$

The large upper endpoint in the final line results from an accidental near-zero in the $\Lambda_c\bar{D}$ denominator. It is therefore more useful as evidence for a stable hierarchy than as a precise enhancement factor.

At each heavier peak mass, the calculated $\Lambda_c\bar{D}^*$ width also shows a stable dependence on the assigned spin,

$$\begin{aligned} 8.67 &\le \frac{\Gamma^{\mathrm{QI}}_{4440,1/2}(\Lambda_c\bar{D}^*)}{\Gamma^{\mathrm{QI}}_{4440,3/2}(\Lambda_c\bar{D}^*)} \le 19.50, \\ 7.99 &\le \frac{\Gamma^{\mathrm{QI}}_{4457,1/2}(\Lambda_c\bar{D}^*)}{\Gamma^{\mathrm{QI}}_{4457,3/2}(\Lambda_c\bar{D}^*)} \le 14.22. \end{aligned} \tag{88}$$

Thus, within all tested QI scenarios, the selected $\Lambda_c\bar{D}^*$ width is larger for $J = 1/2$ than for $J = 3/2$ at the same peak mass. The size of the enhancement remains model dependent.

The two possible assignments of the heavier peaks can now be compared without reusing the QI cluster labels A and B. We call

$$\begin{aligned} &\text{spin ordering I:}\ J[P_c(4440)] = \frac{1}{2}, \quad J[P_c(4457)] = \frac{3}{2}, \\ &\text{spin ordering II:}\ J[P_c(4440)] = \frac{3}{2}, \quad J[P_c(4457)] = \frac{1}{2}. \end{aligned}$$

For spin ordering I, the reference peak-to-peak ratio and its scenario envelope are

$$R_{\mathrm{I}}^{\bar{D}^*} \equiv \frac{\Gamma^{\mathrm{QI}}_{4440,1/2}(\Lambda_c\bar{D}^*)}{\Gamma^{\mathrm{QI}}_{4457,3/2}(\Lambda_c\bar{D}^*)} = 58.4,$$
$$R_{\mathrm{I}}^{\bar{D}^*} \in [37.5, 143.4]. \quad (89)$$

The reversed spin ordering II gives

$$R_{\mathrm{II}}^{\bar{D}^*} \equiv \frac{\Gamma^{\mathrm{QI}}_{4440,3/2}(\Lambda_c\bar{D}^*)}{\Gamma^{\mathrm{QI}}_{4457,1/2}(\Lambda_c\bar{D}^*)} = 0.558,$$
$$R_{\mathrm{II}}^{\bar{D}^*} \in [0.299, 1.495]. \quad (90)$$

Accordingly, a much larger $P_c(4440)$ partial width in this channel would be characteristic of spin ordering I within the present QI model. A ratio of order unity would remain compatible with spin ordering II, but would not by itself establish it because the corresponding scenario envelope crosses unity. In applying either test, an experimental amplitude analysis must separate resonance couplings from production effects and interference with nonresonant contributions.

C. Exploratory one-pion-exchange scenarios

We next examine how the long-range contribution modifies the central QI pattern. The reference OPE scenario uses the direct baryon-line energy transfer $q^0_{\pi,\mathrm{dir}}$, the cutoff $\Lambda_\pi = 0.50$ GeV, and the pion-pole prescription $\xi = \mathrm{pole}$. Table XII lists the corresponding amplitude $T^{(J)}_{00,\pi,\mathrm{ref};fi}$ of Eq. (80), its magnitude relative to QI, the OPE-only width, and the two coherent widths Γ_+ and Γ_- defined in Eq. (83). The amplitude itself does not contain η_{match}; the same global sign is used in every row of each coherent branch. Imaginary parts generated by the on-shell pion cut are retained.

The reference OPE amplitude is largest relative to QI for $P_c(4312)\to\Lambda_c\bar{D}^*$. Its QI width of 0.742 MeV becomes 1.735 MeV in the $\eta_{\mathrm{match}} = +1$ branch and 0.250 MeV in the $\eta_{\mathrm{match}} = -1$ branch. The leading OPE amplitude for $P_c(4312)\to\Lambda_c\bar{D}$ is exactly zero because no $\bar{D}\,\bar{D}\,\pi$ axial vertex exists; that channel is therefore omitted from Table XII, and its small QI width is unchanged. For the other listed transitions, $|T_{00,\pi,\mathrm{ref}}/T_{00,\mathrm{QI}}|$ ranges from 0.024 to 0.233.

At the reference point, the spin-discriminating pattern survives in both globally correlated branches. For the peak-to-peak $\Lambda_c\bar{D}^*$ ratio, spin ordering I gives 73.8 for $\eta_{\mathrm{match}} = +1$ and 47.8 for $\eta_{\mathrm{match}} = -1$, whereas spin ordering II gives 0.615 and 0.511, respectively. Thus the reference OPE contribution changes the absolute widths but does not reverse the QI separation between the two spin orderings.

The reference numbers should not, however, be promoted to unique QI + OPE predictions. Figure 4 displays the regulator dependence in the channel for which OPE is most important. Even the pion-pole prescription depends appreciably on the off-shell continuation chosen for q^0_π. Retaining the full regulated kernel produces a much stronger dependence because its contactlike part has not been matched to the short-distance QI interaction. For a general diagnostic prescription ξ, we use the coherent formula of Eq. (81) with $T^{(J)}_{00,\pi,\mathrm{ref}}$ replaced by $T^{(J)}_{00,\pi,\xi}$ and denote the resulting branches by $\Gamma_{\mathrm{tot},\xi,+}$ and $\Gamma_{\mathrm{tot},\xi,-}$. For example, the full kernel with $q^0_{\pi,\mathrm{dir}}$ and $\Lambda_\pi = 0.50$ GeV gives

$$\Gamma_{\pi,\mathrm{full}} = 7.06\ \mathrm{MeV},$$
$$\Gamma_{\mathrm{tot,full},+} = 12.36\ \mathrm{MeV},$$
$$\Gamma_{\mathrm{tot,full},-} = 3.25\ \mathrm{MeV} \quad (91)$$

for $P_c(4312)\to\Lambda_c\bar{D}^*$. Across the full cutoff and energy-transfer scan, several pion-pole scenarios make the OPE amplitude comparable to the QI amplitude, while the corresponding full-kernel ratios can be considerably larger. This spread diagnoses regulator, energy-transfer, and short-distance-matching sensitivity; it is not a statistical uncertainty and does not justify choosing an extreme scenario as a prediction.

This interpretation is consistent with the general observation that the short-range part of OPE cannot be separated

TABLE XII. Reference OPE matching scenario. For each row, the fi and k labels of the amplitudes and widths are suppressed. Amplitudes are in $\mathrm{GeV}^{-1/2}$ and widths are in MeV. The OPE-only width is independent of η_{match}; Γ_+ and Γ_- use the globally correlated choices $\eta_{\mathrm{match}} = +1$ and -1, respectively.

Initial state	J	Final state	$T^{(J)}_{00,\pi,\mathrm{ref}}$	$\lvert T^{(J)}_{00,\pi,\mathrm{ref}}/T^{(J)}_{00,\mathrm{QI}}\rvert$	$\Gamma^{(J)}_{\pi,\mathrm{ref}}$	$\Gamma^{(J)}_+;\Gamma^{(J)}_-$
$P_c(4312)$	$\frac{1}{2}$	$\Lambda_c\bar{D}^*$	$0.463698 + 0.274212i$	0.581	0.250634	1.735189; 0.250299
$P_c(4440)$	$\frac{1}{2}$	$\Lambda_c\bar{D}$	$-0.008156 + 0.000021i$	0.080	0.000232	0.030518; 0.042079
$P_c(4440)$	$\frac{1}{2}$	$\Lambda_c\bar{D}^*$	$0.010338 - 0.002907i$	0.024	0.000291	0.472523; 0.518729
$P_c(4440)$	$\frac{3}{2}$	$\Lambda_c\bar{D}^*$	$-0.005169 + 0.001453i$	0.040	0.000073	0.041656; 0.048625
$P_c(4457)$	$\frac{1}{2}$	$\Lambda_c\bar{D}$	-0.003996	0.233	0.000057	0.000621; 0.001606
$P_c(4457)$	$\frac{1}{2}$	$\Lambda_c\bar{D}^*$	0.014743	0.085	0.000582	0.067689; 0.095113
$P_c(4457)$	$\frac{3}{2}$	$\Lambda_c\bar{D}^*$	-0.007372	0.131	0.000145	0.006402; 0.010842

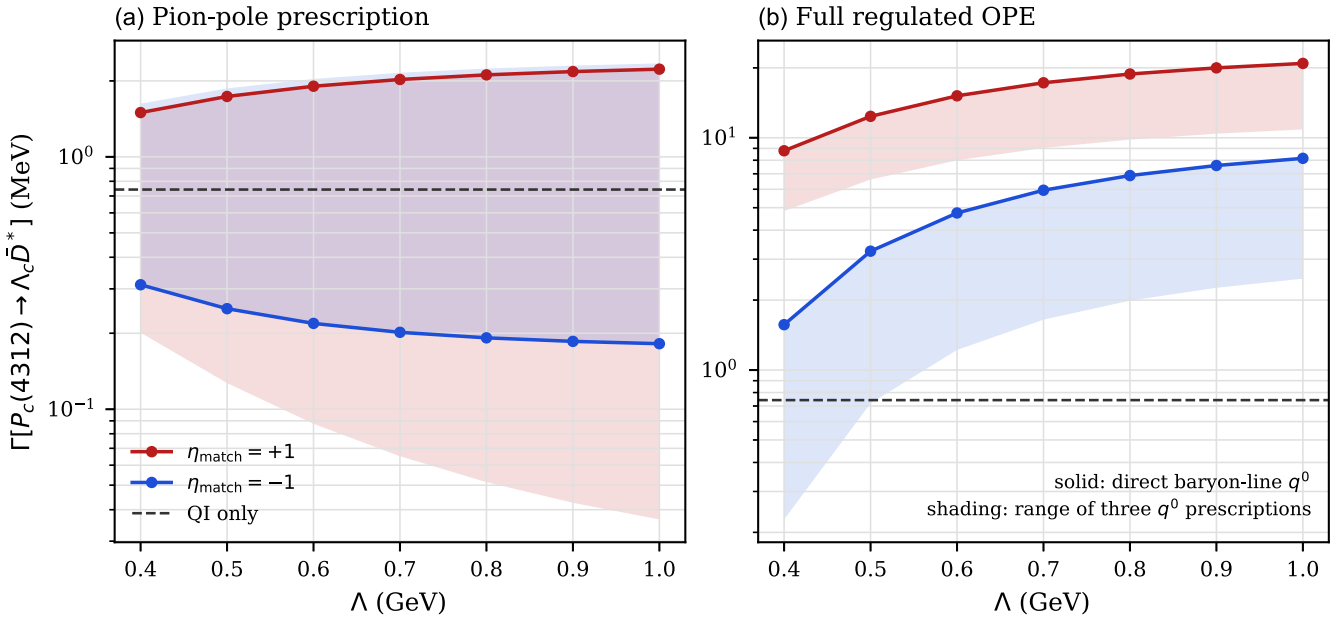


FIG. 4. Exploratory cutoff dependence of $P_c(4312) \to \Lambda_c \bar{D}^*$. Solid curves use $q^0_{\pi,\text{dir}}$, the shaded regions span $q^0_{\pi,\text{dir}}$, $q^0_{\pi,\text{swap}}$, and $q^0_{\pi,\text{stat}}$, and the dashed line is the QI-only width. Panel (a) uses the pion-pole prescription; panel (b) retains the full regulated OPE kernel. The two values of η_{match} are globally correlated matching alternatives. Neither the shading nor the separation of the two branches is a probability interval.

from contact or quark-exchange dynamics in a model-independent manner. Regulator-dependent spin assignments in OPE-based descriptions have been emphasized in Refs. [14,34], while a recent quark-exchange study shows explicitly that the treatment of short-range spin-dependent OPE can alter the molecular interaction [31]. The pion-pole subtraction adopted here is therefore a stated matching prescription, not a derived QI-OPE identity.

D. Comparison with other approaches and experimental implications

Wang *et al.* applied the same prior-post QI framework and amplitude normalization to the hidden-charm $J/\psi p$ and $\eta_c p$ modes [18]. Their calculation fixes the constituent interaction and normalization adopted here, but it does not provide an open-charm numerical benchmark. We therefore compare with studies that explicitly evaluated the $\Lambda_c \bar{D}^{(*)}$ final states, keeping in mind that their dynamics and normalization prescriptions differ.

The uncalculated $J^P = 3/2^- \to \Lambda_c \bar{D}$ transition can be placed on a rough scale by comparison with calculations that retain the required rank-two dynamics. Although a D-wave width has the threshold behavior $\Gamma_D \propto k^5$, its normalization cannot be inferred from the present S-wave amplitudes because the corresponding tensor operator is absent from our QI interaction and from the central OPE projection. Moreover, the final momenta, $k = 0.784$ and 0.808 GeV at the $P_c(4440)$ and $P_c(4457)$ masses, respectively, are not small enough to ensure a strong centrifugal suppression.

The pion-exchange triangle calculation of Ref. [25], which explicitly separates the final S- and D-wave components, gives

$$\Gamma_D[P_c(4440), J = 3/2 \to \Lambda_c \bar{D}] = 1.06 - 1.79 \text{ MeV},$$

$$\Gamma_D[P_c(4457), J = 3/2 \to \Lambda_c \bar{D}] = 0.51 - 0.90 \text{ MeV}.$$

The Bethe-Salpeter calculation of Ref. [26] instead obtains 20.0 and 16.7 MeV for the corresponding assignments. These values use different molecular wave functions, regulators, and transition mechanisms and should not be interpreted as an uncertainty interval for the present calculation. They nevertheless indicate external model estimates spanning approximately 0.5–20 MeV. The $J^P = 3/2^- \to \Lambda_c \bar{D}$ mode therefore need not be negligible, but a quantitative prediction within our framework requires inclusion of the tensor QI and OPE operators and a complete $L_i = 0 \to L_f = 2$ projection.

The reference QI widths are smaller than the constituent-quark, effective-Lagrangian, and Bethe-Salpeter values in Table XIII. The pronounced preference for $\Lambda_c \bar{D}^*$ is nevertheless common to these calculations. This is qualitative agreement on the channel hierarchy, not agreement on the absolute normalization. For example, Li *et al.* obtain 8.8 and 0.026 MeV for the $\Lambda_c \bar{D}^*$ and $\Lambda_c \bar{D}$ modes, respectively [22], compared with the present reference QI values 0.742 and 0.00285 MeV.

The percentages of Lin *et al.* require a separate interpretation. Their complex-scaling calculation includes

TABLE XIII. Selected results for $P_c(4312)\to\Lambda_c\bar{D}^{(*)}$. The first four rows quote absolute partial widths. The final row gives the restricted lower-channel two-body fractions reported in the complex-scaling analysis and must not be interpreted as a width in MeV.

Approach	$\Lambda_c\bar{D}$	$\Lambda_c\bar{D}^*$	Reported observable
Present reference QI	0.00285	0.742	Partial width (MeV)
Dong *et al.* [21]	0	6.16	Partial width (MeV)
Lin and Zou [17]	0.06–0.30	3.8–10.7	Partial width (MeV)
Li *et al.* [22]	0.026	8.8	Partial width (MeV)
Lin *et al.* [23]	0.04%	99.96%	Restricted two-body fraction

contact interactions, retarded OPE, and coupled channels, with low-energy constants fitted to the observed pole properties [23]. On-shell three-body effects are partly included in the total pole width but excluded from the tabulated lower-channel two-body fractions. Multiplying those percentages by the total pole width would therefore not yield partial widths directly comparable with the quantities calculated here. We use them only to compare channel hierarchies. Their $P_c(4440, J = 1/2)$ fractions—10.8%, 38.4%, and 50.9% for $\Lambda_c\bar{D}$, $\Lambda_c\bar{D}^*$, and $\Sigma_c\bar{D}$, respectively—also illustrate why the conditional quantity in Eq. (86) is not an inclusive branching fraction.

Independent calculations find that the $\bar{D}^{(*)}\Lambda_c\pi$ three-body modes can themselves be sizable [30]; these channels lie outside the selected two-body widths considered here.

Several analyses find that open-charm decays can be strongly spin dependent [17,25–27,29], but no unique assignment of the two heavier peaks has emerged. Under the assumption of relatively weak off-diagonal contact interactions, Lin *et al.*, together with the triangle-diagram analysis of Yang *et al.*, favor spin ordering I [23,25]. Other coupled-channel and Bethe-Salpeter studies favor spin ordering II [14,26,28]. The present calculation does not infer the spin ordering from the peak masses. Instead, Eqs. (89) and (90) give distinct conditional decay patterns for the two hypotheses.

The relevant final states can be studied experimentally in $\Lambda_b^0\to\Lambda_c^+\bar{D}^{(*)0}K^-$ decays [32]. The two channels offer complementary experimental advantages. In the LHCb study cited above, the $\Lambda_b^0\to\Lambda_c^+\bar{D}^0K^-$ mode was fully reconstructed from charged particles, whereas the $\bar{D}^{*0}$ mode was treated as partially reconstructed because the neutral particle in $\bar{D}^{*0}\to\bar{D}^0\pi^0$ or $\bar{D}^0\gamma$ was not reconstructed. Full $\bar{D}^{*0}$ reconstruction can therefore incur an efficiency penalty from the additional soft neutral particle, while partial reconstruction provides less complete kinematic information and requires a more involved signal description. The $\Lambda_c\bar{D}$ mode may consequently provide a cleaner experimental spectrum even when its calculated $J = 1/2$ partial width is smaller. Conversely, the larger calculated $\Lambda_c\bar{D}^*$ widths and their pronounced spin dependence make that mode the sharper discriminator within the present model. The actual experimental sensitivity depends also on production rates, reconstruction efficiencies, resolution, backgrounds, and interference, and cannot be inferred from the partial widths alone.

Searches in the two modes are therefore complementary. Direct tests would include a search for the $P_c(4312)$ in $\Lambda_c^+\bar{D}^{*0}$, searches for the two heavier peaks in both $\Lambda_c^+\bar{D}^0$ and $\Lambda_c^+\bar{D}^{*0}$, and an amplitude analysis comparing their resonant $\Lambda_c^+\bar{D}^{*0}$ strengths while separating nonresonant backgrounds and production-dependent interference. These observables probe the stable QI hierarchies without requiring a preferred value of η_{match}.

Taken together, the results identify the $\Lambda_c\bar{D}^*$ hierarchy and its spin dependence as the robust predictions of the present QI calculation. The absolute widths remain model dependent, especially where the QI pieces cancel. The reference OPE contribution preserves the central spin pattern, whereas the broader OPE scan reveals unresolved cutoff, energy-transfer, short-distance, and matching-sign dependence. The following Section summarizes these conclusions and their scope.

VII. SUMMARY AND CONCLUSIONS

We have studied selected open-charm decays of the $P_c(4312)$, $P_c(4440)$, and $P_c(4457)$ as predominantly S-wave $\Sigma_c\bar{D}^{(*)}$ molecules. The $P_c(4312)$ was assigned $J^P = 1/2^-$, while both $J^P = 1/2^-$ and $3/2^-$ $\Sigma_c\bar{D}^*$ assignments were evaluated at each heavier peak mass. Our central results were obtained for the S-wave transitions $\Sigma_c\bar{D}^{(*)}\to\Lambda_c\bar{D}^{(*)}$ at Born order in the QI model. The prior and post rearrangement diagrams were evaluated with their color, flavor, spin, and spatial matrix elements, projected onto the physical $I = 1/2$ channels, and folded with the molecular wave functions.

The most robust QI result is the preference for $\Lambda_c\bar{D}^*$ over $\Lambda_c\bar{D}$ for every $J^P = 1/2^-$ assignment considered. The central $\Lambda_c\bar{D}^*/\Lambda_c\bar{D}$ width ratios are 260.6, 13.73, and 76.53 for the $P_c(4312)$, $P_c(4440)$, and $P_c(4457)$, respectively, and the hierarchy survives all 24 one-at-a-time input variations. These ratios compare only the two calculated open-charm modes and are not inclusive branching fractions. Their large values are also not universal HQSS predictions: they reflect unequal spatial overlaps, hyperfine effects, phase space, and channel-dependent interference.

In particular, the suppressed $P_c(4312)\to\Lambda_c\bar{D}$ width is generated by the hyperfine interaction, whereas the small $P_c(4457, J=1/2)\to\Lambda_c\bar{D}$ width results from a model-dependent cancellation.

The $\Lambda_c\bar{D}^*$ mode also shows a stable spin dependence. At a fixed heavier peak mass, its central QI width for $J^P = 1/2^-$ exceeds that for $J^P = 3/2^-$ by factors of approximately 11.0 at 4440 MeV and 9.5 at 4457 MeV; the separation persists throughout the input scan. Consequently, the two possible spin orderings predict distinct conditional patterns for the resonant $\Lambda_c\bar{D}^*$ strengths. A much larger $P_c(4440)$ partial width is characteristic of spin ordering I, $J[P_c(4440)] = 1/2$ and $J[P_c(4457)] = 3/2$, within the present model. For the reverse ordering, the two strengths can be comparable. This provides a decay-based discriminator but does not determine the ordering from the peak masses alone. The $J^P = 3/2^-\to\Lambda_c\bar{D}$ transition begins in a D wave and was not calculated; it is not predicted to have zero width.

We also explored a direct retarded OPE transition at first Born order. The contact-subtracted pion-pole term was used as the reference long-distance prescription, while the full regulated kernel and alternative energy-transfer choices served as diagnostics. The $P_c(4312)\to\Lambda_c\bar{D}^*$ amplitude is the most sensitive to OPE. At the reference point, both globally correlated matching-sign branches preserve the principal QI channel and spin hierarchies. The broader scan nevertheless reveals substantial dependence on the cutoff, energy-transfer prescription, treatment of the contactlike term, and an unresolved relative QI-OPE sign. The coherent widths are therefore matching-sensitivity scenarios, not unique predictions or statistical uncertainty bands. A predictive synthesis will require QI and pion exchange to be matched in a common regulator-consistent framework that controls double counting and treats rescattering and three-body cuts consistently.

The $\Lambda_c^+\bar{D}^0$ and $\Lambda_c^+\bar{D}^{*0}$ modes are experimentally complementary: the former can provide a cleaner fully reconstructed final state, whereas the latter has the larger calculated $J^P = 1/2^-$ widths and the stronger spin sensitivity within the present model. The most informative experimental program would therefore examine both final states, with a search for the $P_c(4312)$ in $\Lambda_c^+\bar{D}^{*0}$ and a comparison of the resonant $\Lambda_c^+\bar{D}^{*0}$ strengths of the two heavier peaks providing direct tests of the predicted hierarchy and spin dependence. Such measurements require amplitude analyses that separate resonance couplings from nonresonant backgrounds, production effects, and interference. The present conclusions remain conditional on pure-channel Gaussian molecular states, exact-isospin reconstruction, and a first-Born treatment. Coupled channels and final-state rescattering, D-wave transitions, tensor-induced S-D mixing, finite Σ_c and $\bar{D}^*$ widths, and unitary three-body dynamics lie beyond the present scope. Within these limitations, the stable $\Lambda_c\bar{D}^*$ hierarchy and its pronounced spin dependence make the selected open-charm modes useful probes of the molecular interpretation of the narrow P_c states.

ACKNOWLEDGMENTS

V. P. acknowledges the financial assistance by University Grants Commission (UGC) under the CSIR-UGC Junior Research Fellow (JRF) scheme with Ref. No. 231610186052.

DATA AVAILABILITY

There are no publicly available research data or software supporting this manuscript. Requests for further information or data should be sent to the authors.

APPENDIX A: CONSTITUENT-STATE AND INTERNAL-WAVE-FUNCTION CONVENTIONS

This Appendix specifies the normalized constituent states and phase conventions used to obtain the color, flavor, and spin factors in Sec. III. We also collect here the internal spatial wave functions of the external mesons and baryons. The constituent labels are those of Eqs. (24)–(26): the initial state is $A(12) = D^{(*)-}(\bar{c}_1 d_2)$ and $B(345) = \Sigma_c^{++}(c_3 u_4 u_5)$, while the two labeled final clusterings are $F_{14} = M_f(14)B_f(325)$ and $F_{15} = M_f(15)B_f(324)$.

1. Internal spatial wave functions

For each external hadron, the internal wave function is factorized as

$$\Psi_H = \chi_H^c \chi_H^f \chi_H^s \phi_H, \tag{A1}$$

where χ_H^c, χ_H^f, and χ_H^s denote the color, flavor, and spin factors, respectively, and ϕ_H is the momentum-space spatial wave function. Following Ref. [18], we use normalized Gaussian functions for the ground-state mesons and baryons.

For a meson $M(\bar{q}_\nu q_{\nu'})$ with total momentum $\mathbf{P}_M = \mathbf{p}_\nu + \mathbf{p}_{\nu'}$, the mass-weighted relative momentum is

$$\begin{aligned}\mathbf{p}_{\rm rel}^{(\nu\nu')} &= \frac{m_\nu \mathbf{p}_{\nu'} - m_{\nu'}\mathbf{p}_\nu}{m_\nu + m_{\nu'}} \\ &= \mathbf{p}_{\nu'} - \frac{m_{\nu'}}{m_\nu + m_{\nu'}}\mathbf{P}_M.\end{aligned} \tag{A2}$$

Equivalently, $\mathbf{p}_{\rm rel} = (m_{\bar{q}}\mathbf{p}_q - m_q\mathbf{p}_{\bar{q}})/(m_q + m_{\bar{q}})$. The normalized S-wave Gaussian is

$$\phi_M(\mathbf{p}_{\rm rel}) = \frac{1}{\pi^{3/4}\beta_M^{3/2}}\exp\left[-\frac{p_{\rm rel}^2}{2\beta_M^2}\right], \tag{A3}$$

with

$$\int d^3p_{\rm rel}|\phi_M(\mathbf{p}_{\rm rel})|^2 = 1. \tag{A4}$$

Equation (A2) is used for both the initial $D^{(*)-}(12)$ and the final $\bar{D}^{(*)0}(14)$ or $\bar{D}^{(*)0}(15)$, with the appropriate constituent labels and meson width β_M.

For an ordered baryon $B(\nu_1\nu_2\nu_3)$, with constituent ν_1 chosen as the first entry, define $m_{\nu_1\nu_2\nu_3} \equiv m_{\nu_1} + m_{\nu_2} + m_{\nu_3}$. The mass-weighted Jacobi momenta are

$$\begin{aligned}\mathbf{p}_\rho^{(\nu_1\nu_2\nu_3)} &= \frac{1}{\sqrt{2}m_{\nu_1\nu_2\nu_3}}[(m_{\nu_1}+2m_{\nu_3})\mathbf{p}_{\nu_2} \\ &\quad -(m_{\nu_1}+2m_{\nu_2})\mathbf{p}_{\nu_3}+(m_{\nu_3}-m_{\nu_2})\mathbf{p}_{\nu_1}], \\ \mathbf{p}_\lambda^{(\nu_1\nu_2\nu_3)} &= \sqrt{\frac{3}{2}}\frac{1}{m_{\nu_1\nu_2\nu_3}}[m_{\nu_1}(\mathbf{p}_{\nu_2}+\mathbf{p}_{\nu_3}) \\ &\quad -(m_{\nu_2}+m_{\nu_3})\mathbf{p}_{\nu_1}].\end{aligned} \tag{A5}$$

The corresponding normalized S-wave baryon Gaussian is

$$\begin{aligned}\phi_B(\mathbf{p}_{\nu_1},\mathbf{p}_{\nu_2},\mathbf{p}_{\nu_3}) &= \frac{3^{3/4}}{\pi^{3/2}\alpha_\rho^{3/2}\alpha_\lambda^{3/2}} \\ &\quad \times\exp\left[-\frac{(p_\rho^{(\nu_1\nu_2\nu_3)})^2}{2\alpha_\rho^2}-\frac{(p_\lambda^{(\nu_1\nu_2\nu_3)})^2}{2\alpha_\lambda^2}\right].\end{aligned} \tag{A6}$$

At fixed baryon momentum $\mathbf{P}_B$, its normalization may be written as

$$\int d^3p_{\nu_1}d^3p_{\nu_2}|\phi_B(\mathbf{p}_{\nu_1},\mathbf{p}_{\nu_2},\mathbf{P}_B-\mathbf{p}_{\nu_1}-\mathbf{p}_{\nu_2})|^2 = 1. \tag{A7}$$

At fixed $\mathbf{P}_B$, the six-dimensional Jacobian associated with Eq. (A5) is

$$\left|\frac{\partial(\mathbf{p}_\rho,\mathbf{p}_\lambda)}{\partial(\mathbf{p}_{\nu_1},\mathbf{p}_{\nu_2})}\right|_{\mathbf{P}_B} = 3^{3/2}, \quad d^3p_\rho d^3p_\lambda = 3^{3/2}d^3p_{\nu_1}d^3p_{\nu_2}. \tag{A8}$$

The factor $3^{3/4}$ in Eq. (A6) is the corresponding wave-function normalization factor. For equal light-quark masses, $m_{\nu_2} = m_{\nu_3} = m_q$, one has $\mathbf{p}_\rho = (\mathbf{p}_{\nu_2} - \mathbf{p}_{\nu_3})/\sqrt{2}$, while $\mathbf{p}_\lambda$ describes the motion of the heavy quark relative to the light pair.

The ordered triplets used here are

$$\begin{aligned}\Sigma_c^{++}&:\ (\nu_1,\nu_2,\nu_3) = (3,4,5), \\ \Lambda_c(F_{14})&:\ (\nu_1,\nu_2,\nu_3) = (3,2,5), \\ \Lambda_c(F_{15})&:\ (\nu_1,\nu_2,\nu_3) = (3,2,4).\end{aligned} \tag{A9}$$

Thus the same definition, Eq. (A5), is used for the initial and final baryons after replacing the ordered constituent labels. The central charmed-baryon widths quoted in Table II follow the parametrization of Ref. [18]; in particular, its central-width prescription is

$$\alpha_\lambda^2 = \left(\frac{3m_c}{2m_q+m_c}\right)^{1/2}\alpha_\rho^2, \tag{A10}$$

up to the rounding of the tabulated widths. The internal hadron Gaussians in Eqs. (A3) and (A6) are distinct from the molecular radial wave function $R_0(p)$ in Eq. (9). Diagram-dependent momentum routing and the reduction of products of four such Gaussians are given in Appendix B.

2. Color states

Let $a_i \in \{1,2,3\}$ denote the color carried by constituent i. In the ordered five-constituent basis $|\bar{a}_1 a_2 a_3 a_4 a_5\rangle$, the initial color state is

$$\chi_{AB}^c = \frac{1}{\sqrt{18}}\delta_{a_1a_2}\epsilon_{a_3a_4a_5}|\bar{a}_1a_2a_3a_4a_5\rangle, \tag{A11}$$

where repeated color indices are summed. The two labeled final color states are

$$\chi_{F_{14}}^c = \frac{1}{\sqrt{18}}\delta_{a_1a_4}\epsilon_{a_3a_2a_5}|\bar{a}_1a_2a_3a_4a_5\rangle, \tag{A12}$$

$$\chi_{F_{15}}^c = \frac{1}{\sqrt{18}}\delta_{a_1a_5}\epsilon_{a_3a_2a_4}|\bar{a}_1a_2a_3a_4a_5\rangle. \tag{A13}$$

Each state is a product of a normalized meson singlet and a normalized baryon singlet, and therefore

$$\langle\chi_{AB}^c|\chi_{AB}^c\rangle = \langle\chi_{F_{14}}^c|\chi_{F_{14}}^c\rangle = \langle\chi_{F_{15}}^c|\chi_{F_{15}}^c\rangle = 1. \tag{A14}$$

For a quark, $t^A = \lambda^A/2$, whereas the generator acting on constituent 1 is the antiquark generator

$$t_{\bar{q}}^A = -(t_q^A)^*. \tag{A15}$$

The contractions can be reduced with the fundamental $SU(3)$ identity

$$\sum_{A=1}^{8}(t^A)_{ab}(t^A)_{cd} = \frac{1}{2}\left(\delta_{ad}\delta_{bc}-\frac{1}{3}\delta_{ab}\delta_{cd}\right). \tag{A16}$$

For example, inserting Eqs. (A11), (A12), and (A15) gives

$$I_{C,\rm pr}^{14}(13) = \langle\chi_{F_{14}}^c|\mathbf{t}_1\cdot\mathbf{t}_3|\chi_{AB}^c\rangle = \frac{2}{9}. \tag{A17}$$

Applying the same contraction to the remaining prior and post pairs gives the color vectors in Table III. For every representation and labeled topology they satisfy

$$\sum_{\nu\nu'\in\mathcal{P}_{r,a}} I^{a}_{C,r}(\nu\nu')=0, \quad r\in\{\mathrm{pr},\mathrm{po}\}, \quad a\in\{14,15\}. \tag{A18}$$

This identity is the color-singlet cancellation used in the distributional treatment of the linear-confinement term.

3. Flavor states

The constituent interaction is diagonal in flavor and does not change the flavor carried by a labeled constituent line. The charged initial component therefore has the normalized flavor state

$$\chi^{f}_{AB}=|\bar{c}_1 d_2 c_3 u_4 u_5\rangle. \tag{A19}$$

For topology F_{14}, the final $\bar{D}^{(*)0}$ contains labels (1, 4) and the antisymmetric light pair in the Λ_c contains labels (2, 5). For F_{15}, the corresponding pairs are (1, 5) and (2, 4). In the same ordered five-particle basis, the final flavor states are therefore

$$\chi^{f}_{F_{14}}=\frac{1}{\sqrt{2}}(|\bar{c}_1 d_2 c_3 u_4 u_5\rangle-|\bar{c}_1 u_2 c_3 u_4 d_5\rangle), \tag{A20}$$

$$\chi^{f}_{F_{15}}=\frac{1}{\sqrt{2}}(|\bar{c}_1 d_2 c_3 u_4 u_5\rangle-|\bar{c}_1 u_2 c_3 d_4 u_5\rangle). \tag{A21}$$

The relative minus sign in each of Eqs. (A20) and (A21), together with the sign chosen for its first ket, fixes the Λ_c flavor-state phase convention used here. A simultaneous overall rephasing of the Λ_c state is conventional and leaves QI-only widths unchanged, but the same phase convention must be used when the QI amplitude is combined coherently with another transition mechanism. The two kets in either final state are orthogonal. Since only the first ket in Eqs. (A20) and (A21) overlaps with Eq. (A19), one obtains

$$I^{14}_{F}=\langle\chi^{f}_{F_{14}}|\chi^{f}_{AB}\rangle=I^{15}_{F}=\langle\chi^{f}_{F_{15}}|\chi^{f}_{AB}\rangle=\frac{1}{\sqrt{2}}. \tag{A22}$$

The subsequent antisymmetrization of the two labeled clusterings is a separate normalization issue and is discussed in Appendix C.

4. Spin states and recoupling

All spin states are defined in the Condon-Shortley convention. For two spin-1/2 constituents ν and ν', we use

$$\chi^{(\nu\nu')}_{00}=\frac{1}{\sqrt{2}}(|\uparrow_\nu\downarrow_{\nu'}\rangle-|\downarrow_\nu\uparrow_{\nu'}\rangle), \tag{A23}$$

$$\chi^{(\nu\nu')}_{11}=|\uparrow_\nu\uparrow_{\nu'}\rangle, \qquad \chi^{(\nu\nu')}_{10}=\frac{1}{\sqrt{2}}(|\uparrow_\nu\downarrow_{\nu'}\rangle+|\downarrow_\nu\uparrow_{\nu'}\rangle),$$
$$\chi^{(\nu\nu')}_{1,-1}=|\downarrow_\nu\downarrow_{\nu'}\rangle. \tag{A24}$$

Thus

$$\chi^{s}_{\bar{D}}(\nu\nu')=\chi^{(\nu\nu')}_{00}, \qquad \chi^{s}_{\bar{D}^*,m}(\nu\nu')=\chi^{(\nu\nu')}_{1m}. \tag{A25}$$

The light pair (4, 5) in the initial Σ_c is in a spin-1 state and is coupled with the charm-quark spin to $s_{\Sigma_c}=1/2$,

$$\chi^{s}_{\Sigma_c,m_\Sigma}(345)=\sum_{m_{45},m_3}\left\langle 1m_{45},\frac{1}{2}m_3\middle|\frac{1}{2}m_\Sigma\right\rangle\chi^{(45)}_{1m_{45}}\chi^{(3)}_{\frac{1}{2}m_3}. \tag{A26}$$

For later reference, the two projections are

$$\chi^{s}_{\Sigma_c,+\frac{1}{2}}=\sqrt{\frac{2}{3}}\chi^{(45)}_{11}\chi^{(3)}_{\frac{1}{2},-\frac{1}{2}}-\frac{1}{\sqrt{3}}\chi^{(45)}_{10}\chi^{(3)}_{\frac{1}{2},+\frac{1}{2}}, \tag{A27}$$

$$\chi^{s}_{\Sigma_c,-\frac{1}{2}}=\frac{1}{\sqrt{3}}\chi^{(45)}_{10}\chi^{(3)}_{\frac{1}{2},-\frac{1}{2}}-\sqrt{\frac{2}{3}}\chi^{(45)}_{1,-1}\chi^{(3)}_{\frac{1}{2},+\frac{1}{2}}. \tag{A28}$$

The final Λ_c has a spin-zero light pair, so that

$$\chi^{s}_{\Lambda_c,m_\Lambda}(325)=\chi^{(25)}_{00}\chi^{(3)}_{\frac{1}{2}m_\Lambda}, \tag{A29}$$

$$\chi^{s}_{\Lambda_c,m_\Lambda}(324)=\chi^{(24)}_{00}\chi^{(3)}_{\frac{1}{2}m_\Lambda}. \tag{A30}$$

The meson and baryon spins are coupled in that order. If $s_A=0$ or 1 is the spin of the initial $D^{(*)-}$, the initial five-constituent spin state is

$$\chi^{s;JM_J}_{AB}(s_A)=\sum_{m_A,m_\Sigma}\langle s_A m_A,\frac{1}{2}m_\Sigma|JM_J\rangle\chi^{(12)}_{s_A m_A}\chi^{s}_{\Sigma_c,m_\Sigma}(345). \tag{A31}$$

For $a=14$, 15, define

$$(\nu^{(M)}_{14},\nu^{(B)}_{14})=(4,5), \qquad (\nu^{(M)}_{15},\nu^{(B)}_{15})=(5,4). \tag{A32}$$

The corresponding final spin state, with final-meson spin $s_{M_f}=0$ or 1, is

$$\chi^{s;JM_J}_{F_a}(s_{M_f})=\sum_{m_M,m_\Lambda}\langle s_{M_f}m_M,\frac{1}{2}m_\Lambda|JM_J\rangle \times\chi^{(1\nu^{(M)}_a)}_{s_{M_f}m_M}\chi^{s}_{\Lambda_c,m_\Lambda}(32\nu^{(B)}_a). \tag{A33}$$

The change from the initial to the final coupling tree can be organized with Wigner symbols rather than evaluated projection by projection. We write $\hat{j}\equiv\sqrt{2j+1}$. The elementary three-angular-momentum recoupling relation is

$$|((j_1j_2)j_{12},j_3)JM_J\rangle = \sum_{j_{23}}(-1)^{j_1+j_2+j_3+J}\hat{j}_{12}\hat{j}_{23} \times \begin{Bmatrix} j_1 & j_2 & j_{12} \\ j_3 & J & j_{23} \end{Bmatrix} |(j_1,(j_2j_3)j_{23})JM_J\rangle, \tag{A34}$$

while the four-spin change of pairings is

$$\langle[(j_1j_3)j_{13}(j_2j_4)j_{24}]KM_K|[(j_1j_2)j_{12}(j_3j_4)j_{34}]KM_K\rangle = \hat{j}_{12}\hat{j}_{34}\hat{j}_{13}\hat{j}_{24}\begin{Bmatrix} j_1 & j_2 & j_{12} \\ j_3 & j_4 & j_{34} \\ j_{13} & j_{24} & K \end{Bmatrix}. \tag{A35}$$

For F_{14}, Eq. (A35) is applied to the four-spin rearrangement $(12)(45)\to(14)(25)$; for F_{15} it is applied after $4 \leftrightarrow 5$. Because the charm spin s_3 is coupled inside both baryons, the complete open-charm overlap is a five-spin recoupling: one uses Eq. (A34) to couple s_3 last, performs the four-spin transformation in Eq. (A35), and recouples s_3 to the final baryon. Thus the result is a product and sum of $6j$ and $9j$ coefficients, not a single four-spin $9j$ coefficient. The explicit states above fix all pair-ordering phases and provide a direct check of the Wigner-symbol evaluation.

For a spin-1 meson and a spin-1/2 baryon, the two couplings needed in this work may be displayed at $M_J = +1/2$ as

$$[\chi_1\chi_{\frac{1}{2}}]_{\frac{1}{2},+\frac{1}{2}} = \sqrt{\frac{2}{3}}\chi_{11}\chi_{\frac{1}{2},-\frac{1}{2}} - \frac{1}{\sqrt{3}}\chi_{10}\chi_{\frac{1}{2},+\frac{1}{2}}, \tag{A36}$$

$$[\chi_1\chi_{\frac{1}{2}}]_{\frac{3}{2},+\frac{1}{2}} = \frac{1}{\sqrt{3}}\chi_{11}\chi_{\frac{1}{2},-\frac{1}{2}} + \sqrt{\frac{2}{3}}\chi_{10}\chi_{\frac{1}{2},+\frac{1}{2}}. \tag{A37}$$

Equations (A31) and (A33) define normalized states for any M_J. We use $M_J = +1/2$ to evaluate the scalar overlaps; rotational invariance makes the result independent of this convenient choice.

5. Representative spin and combined factors

For the CL interaction, $\hat{O}_{\rm CL} = 1$, so the spin factor is the direct overlap of Eqs. (A31) and (A33). For the HF term, we use

$$\mathbf{s}_\nu \cdot \mathbf{s}_{\nu'} = s_\nu^z s_{\nu'}^z + \frac{1}{2}(s_\nu^+ s_{\nu'}^- + s_\nu^- s_{\nu'}^+). \tag{A38}$$

Equivalently, in a basis of definite pair spin $s_{\nu\nu'}$,

$$\mathbf{s}_\nu \cdot \mathbf{s}_{\nu'} = \frac{1}{2}\left[s_{\nu\nu'}(s_{\nu\nu'}+1) - \frac{3}{2}\right], \tag{A39}$$

with eigenvalues $-3/4$ and $+1/4$ for $s_{\nu\nu'} = 0$ and 1, respectively. Here $\mathbf{s}_\nu$ is the spin-1/2 operator used in Eq. (33); it is related to the Pauli matrix by $\boldsymbol{\sigma}_\nu = 2\mathbf{s}_\nu$. Therefore no additional factor of 4 multiplies the hyperfine entries below. For a chosen interacting pair, Eq. (A34) may be used to expose $s_{\nu\nu'}$ before applying Eq. (A39).

As a compact phase-convention check, the spin-independent overlaps for topology F_{14} are

Transition	J	$I_{S,\rm CL}^{14,J}$
$\Sigma_c\bar{D}\to\Lambda_c\bar{D}$	$\frac{1}{2}$	0
$\Sigma_c\bar{D}\to\Lambda_c\bar{D}^*$	$\frac{1}{2}$	$-\frac{1}{2}$
$\Sigma_c\bar{D}^*\to\Lambda_c\bar{D}$	$\frac{1}{2}$	$-\frac{1}{2}$
$\Sigma_c\bar{D}^*\to\Lambda_c\bar{D}^*$	$\frac{1}{2}$	$1/\sqrt{3}$
$\Sigma_c\bar{D}^*\to\Lambda_c\bar{D}^*$	$\frac{3}{2}$	$-1/(2\sqrt{3})$.

(A40)

These are the identity-operator entries of Table IV. The hyperfine entries follow by inserting Eq. (A38) for each ordered interacting pair. For example, for $\Sigma_c\bar{D}\to\Lambda_c\bar{D}$ in topology F_{14},

$$I_{S,\rm HF,pr}^{14,1/2}(13) = \langle\chi_{F_{14}}^{s;1/2,1/2}|\mathbf{s}_1\cdot\mathbf{s}_3|\chi_{AB}^{s;1/2,1/2}\rangle = \frac{\sqrt{3}}{8}. \tag{A41}$$

Combining Eqs. (A17), (A22), and (A41) with the single prior-post averaging factor gives

$$\kappa_{\rm pr,14,13,HF}^{(1/2)} = \frac{1}{2}\left(\frac{2}{9}\right)\left(\frac{1}{\sqrt{2}}\right)\left(\frac{\sqrt{3}}{8}\right) = \frac{\sqrt{6}}{144}. \tag{A42}$$

The factor 1/2 in Eq. (A42) is the arithmetic prior-post average and is included exactly once. The remaining entries in Tables III and IV follow from the same normalized states and contractions. More explicitly, let P_{45} interchange the constituent labels 4 and 5 in an ordered interacting pair. The factors of topology F_{15} are then related to those of F_{14} by

$$I_{C,r}^{15}(\nu\nu') = -I_{C,r}^{14}(P_{45}(\nu\nu')), \tag{A43}$$

$$I_F^{15} = I_F^{14}, \tag{A44}$$

$$I_{S,X,r}^{15,J}(\nu\nu') = I_{S,X,r}^{14,J}(P_{45}(\nu\nu')), \tag{A45}$$

where $r\in\{\rm pr,po\}$ and $X\in\{\rm CL,HF\}$. Together with the corresponding spatial mapping in Appendix B, these relations generate all F_{15} entries from the F_{14} calculation. The normalization and relative sign with which the two labeled clusterings form the physical identical-quark final state are a separate issue and are derived in Appendix C.

APPENDIX B: MOMENTUM ROUTING AND GAUSSIAN SPATIAL MATRIX ELEMENTS

This Appendix gives the momentum routing and analytic Gaussian reduction used for the spatial factors in the QI kernel. The normalized meson and baryon wave functions, including the mass-weighted Jacobi momenta, are defined in Appendix A 1. Here we adapt the momentum-space construction of Ref. [18] to the open-charm clusterings $A(12)+B(345)\to M_f(1\nu_a^{(M)})+B_f(32\nu_a^{(B)})$, with

$$(\nu_{14}^{(M)},\nu_{14}^{(B)})=(4,5),\qquad (\nu_{15}^{(M)},\nu_{15}^{(B)})=(5,4). \tag{B1}$$

The derivation applies to both $M_f=\bar{D}$ and $\bar{D}^*$ because their spatial wave functions differ only through the Gaussian width.

1. External momenta and constituent routing

We work in the two-hadron center-of-mass frame and assign

$$\mathbf{P}_A=\mathbf{p},\qquad \mathbf{P}_B=-\mathbf{p},$$
$$\mathbf{P}_{M_f}=\mathbf{k},\qquad \mathbf{P}_{B_f}=-\mathbf{k}. \tag{B2}$$

For an ordered interaction $\nu\nu'$, the transferred momentum $\mathbf{q}_{\nu\nu'}$ is delivered to constituent ν and removed from constituent ν',

$$\delta\mathbf{p}_n^{(\nu\nu')}=\mathbf{q}_{\nu\nu'}(\delta_{n\nu}-\delta_{n\nu'}),\qquad \mathbf{p}_n'=\mathbf{p}_n+\delta\mathbf{p}_n^{(\nu\nu')}. \tag{B3}$$

Thus the order of the labels matters; for example, 43 means $\delta\mathbf{p}_4=+\mathbf{q}_{43}$ and $\delta\mathbf{p}_3=-\mathbf{q}_{43}$. The ordered pair sets are

$$\mathcal{P}_{\mathrm{pr},14}=\mathcal{P}_{\mathrm{pr},15}=\{13,14,15,23,24,25\}, \tag{B4}$$

$$\mathcal{P}_{\mathrm{po},14}=\{13,12,15,43,42,45\}, \tag{B5}$$

$$\mathcal{P}_{\mathrm{po},15}=\{13,12,14,53,52,54\}. \tag{B6}$$

Equations (B3)–(B6) therefore specify the momentum transfer in every prior and post diagram.

It is convenient to use $\mathbf{p}_3$ and $\mathbf{p}_4$ as independent internal momenta. Momentum conservation in the initial baryon gives

$$\mathbf{p}_5=-\mathbf{p}-\mathbf{p}_3-\mathbf{p}_4. \tag{B7}$$

The condition $\mathbf{p}_1'+\mathbf{p}'_{\nu_a^{(M)}}=\mathbf{k}$ for the final meson then fixes the remaining initial momenta,

$$\mathbf{p}_1=\mathbf{k}-\mathbf{p}_{\nu_a^{(M)}}-\delta\mathbf{p}_1^{(\nu\nu')}-\delta\mathbf{p}_{\nu_a^{(M)}}^{(\nu\nu')},\qquad \mathbf{p}_2=\mathbf{p}-\mathbf{p}_1. \tag{B8}$$

These assignments satisfy

$$\mathbf{p}_1+\mathbf{p}_2=\mathbf{p},\qquad \mathbf{p}_3+\mathbf{p}_4+\mathbf{p}_5=-\mathbf{p},$$
$$\mathbf{p}_1'+\mathbf{p}'_{\nu_a^{(M)}}=\mathbf{k},\qquad \mathbf{p}_3'+\mathbf{p}_2'+\mathbf{p}'_{\nu_a^{(B)}}=-\mathbf{k}, \tag{B9}$$

for every pair in Eqs. (B4)–(B6). Consequently, no diagram-specific momentum constraint is needed beyond the ordered shift rule in Eq. (B3).

The meson relative momenta following from Eq. (A2) are

$$\mathbf{a}_A=\mathbf{p}_2-\xi_A\mathbf{p},\qquad \xi_A=\frac{m_2}{m_1+m_2},$$
$$\mathbf{a}_f=\mathbf{p}'_{\nu_a^{(M)}}-\xi_f\mathbf{k},\qquad \xi_f=\frac{m_{\nu_a^{(M)}}}{m_1+m_{\nu_a^{(M)}}}. \tag{B10}$$

Equivalently, $1-\xi_A=m_1/(m_1+m_2)$ is the mass fraction denoted by f_A in Ref. [18]. The initial and final baryon arguments are the ordered triplets (345) and $(32\nu_a^{(B)})$, respectively, as fixed in Eq. (A9).

With these conventions, the spatial factor associated with the scalar potential $v^X_{\nu\nu'}(q_{\nu\nu'})$, where $X\in\{\mathrm{CL},\mathrm{HF}\}$, is

$$I^{a,\nu\nu'}_{\mathrm{space},X}(\mathbf{k},\mathbf{p})=\int d^3q_{\nu\nu'}d^3p_3d^3p_4\,v^X_{\nu\nu'}(q_{\nu\nu'})\phi_A(\mathbf{a}_A)\times\phi_B(\mathbf{p}_3,\mathbf{p}_4,\mathbf{p}_5)\phi^*_{M_f}(\mathbf{a}_f)\phi^*_{B_f}(\mathbf{p}_3{}',\mathbf{p}_2{}',\mathbf{p}_{\nu_a^{(B)}}{}'). \tag{B11}$$

The representation label $r\in\{\mathrm{pr},\mathrm{po}\}$ retained in Sec. III is a bookkeeping label. For $\nu\nu'\in\mathcal{P}_{r,a}$, we use the identification

$$I^{r,a,\nu\nu'}_{\mathrm{space},X}\equiv I^{a,\nu\nu'}_{\mathrm{space},X}. \tag{B12}$$

The spatial matrix element is fixed by the topology and the ordered interacting pair. The prior-post distinction enters through the pair set and through the coefficient $\kappa^{(J)}_{r,a,\nu\nu',X}$. The integration measure in Eq. (B11) follows the convention of Ref. [18]; no additional $(2\pi)^{-3}$ factor is included in the internal overlap.

As a worked example, consider the ordered pair 13 in topology F_{14}. In this case $\delta\mathbf{p}_1=\mathbf{q}_{13}$, $\delta\mathbf{p}_3=-\mathbf{q}_{13}$, and all other shifts vanish. Equations (B7) and (B8) give

$$\mathbf{p}_1=\mathbf{k}-\mathbf{p}_4-\mathbf{q}_{13},\qquad \mathbf{p}_2=\mathbf{p}-\mathbf{k}+\mathbf{p}_4+\mathbf{q}_{13},$$
$$\mathbf{p}_3{}'=\mathbf{p}_3-\mathbf{q}_{13},\qquad \mathbf{p}_1{}'=\mathbf{k}-\mathbf{p}_4,$$
$$\mathbf{p}_2{}'=\mathbf{p}_2,\qquad \mathbf{p}_4{}'=\mathbf{p}_4,\qquad \mathbf{p}_5{}'=\mathbf{p}_5. \tag{B13}$$

The corresponding overlap is

$$I^{14,13}_{\mathrm{space},X} = \int d^3q_{13}d^3p_3d^3p_4 v^X_{13}(q_{13}) \times \phi_A[(1-\xi_A)\mathbf{p}-\mathbf{k}+\mathbf{p}_4+\mathbf{q}_{13}] \times \phi_B(\mathbf{p}_3,\mathbf{p}_4,-\mathbf{p}-\mathbf{p}_3-\mathbf{p}_4)\phi^*_{M_f}(\mathbf{p}_4-\xi_f\mathbf{k}) \times \phi^*_{B_f}(\mathbf{p}_3-\mathbf{q}_{13},\mathbf{p}-\mathbf{k}+\mathbf{p}_4+\mathbf{q}_{13},\mathbf{p}_5). \quad \text{(B14)}$$

All remaining overlaps follow by changing the ordered pair in Eq. (B3); the second topology follows at the same time from $\nu^{(M)}_{14} \leftrightarrow \nu^{(M)}_{15}$ and $\nu^{(B)}_{14} \leftrightarrow \nu^{(B)}_{15}$.

2. Quadratic form of the four-hadron overlap

For the Gaussian reduction, the ordered pair is held fixed and we write $\mathbf{q} \equiv \mathbf{q}_{\nu\nu'}$ to avoid repeating its suffix. The product in Eq. (B11) contains six three-vector Gaussian arguments. We collect them as

$$\mathbf{z}_1 = \mathbf{a}_A, \quad \mathbf{z}_2 = \mathbf{p}_{\rho,B}, \quad \mathbf{z}_3 = \mathbf{p}_{\lambda,B}, \quad \mathbf{z}_4 = \mathbf{a}_f, \quad \mathbf{z}_5 = \mathbf{p}_{\rho,B_f}, \quad \mathbf{z}_6 = \mathbf{p}_{\lambda,B_f}, \quad \text{(B15)}$$

with the associated widths

$$(\omega_1,\ldots,\omega_6) = (\beta_A,\alpha_{\rho,B},\alpha_{\lambda,B},\beta_f,\alpha_{\rho,B_f},\alpha_{\lambda,B_f}). \quad \text{(B16)}$$

Every argument is an affine function of the nine integration components. Introducing

$$\mathbf{x} = \begin{pmatrix} \mathbf{q} \\ \mathbf{p}_3 \\ \mathbf{p}_4 \end{pmatrix}, \qquad \mathbf{z}_h = \mathsf{L}_h\mathbf{x} + \mathbf{d}_h, \quad h = 1,\ldots,6, \quad \text{(B17)}$$

the 3×9 matrices L_h follow directly from Eqs. (B3)–(B10) and the Jacobi definitions in Eq. (A5). The vectors $\mathbf{d}_h$ contain only the fixed external momenta $\mathbf{p}$ and $\mathbf{k}$. Thus the product of the four normalized hadron wave functions can be written as

$$\Phi_{a,\nu\nu'}(\mathbf{x}) \equiv \phi_A\phi_B\phi^*_{M_f}\phi^*_{B_f} = \mathcal{N}_4 \exp\left[-\frac{1}{2}\mathbf{x}^T\mathsf{A}\mathbf{x} + \boldsymbol{\eta}^T\mathbf{x} - \frac{1}{2}C\right], \quad \text{(B18)}$$

where $\mathcal{N}_4$ is the product of the two meson and two baryon normalization constants, and

$$\mathsf{A} = \sum_{h=1}^{6}\frac{\mathsf{L}_h^T\mathsf{L}_h}{\omega_h^2}, \quad \boldsymbol{\eta} = -\sum_{h=1}^{6}\frac{\mathsf{L}_h^T\mathbf{d}_h}{\omega_h^2}, \quad C = \sum_{h=1}^{6}\frac{\mathbf{d}_h^2}{\omega_h^2}. \quad \text{(B19)}$$

The topology and pair labels on A, $\boldsymbol{\eta}$, and C are suppressed in Eqs. (B18) and (B19); $\boldsymbol{\eta}$ and C also depend on the external momenta. For the routings used here, the matrix obtained by stacking $\mathsf{L}_1,\ldots,\mathsf{L}_6$ has full column rank. Consequently, positive Gaussian widths make A real, symmetric, and positive definite.

For the explicit F_{14}, 13 example, the six affine arguments entering Eq. (B17) are obtained from

$$\mathbf{a}_A = (1-\xi_A)\mathbf{p}-\mathbf{k}+\mathbf{p}_4+\mathbf{q}_{13}, \qquad \mathbf{a}_f = \mathbf{p}_4-\xi_f\mathbf{k}, \qquad (\mathbf{p}_3,\mathbf{p}_4,\mathbf{p}_5)_B, \qquad (\mathbf{p}_3-\mathbf{q}_{13},\mathbf{p}_2,\mathbf{p}_5)_{B_f}, \quad \text{(B20)}$$

where the last two ordered triplets are converted to their ρ and λ momenta with Eq. (A5). This gives the matrices in Eq. (B19) without any additional momentum convention.

3. Analytic hyperfine overlap

The scalar hyperfine potential for the fixed pair is

$$v^{\mathrm{HF}}_{\nu\nu'}(q) = -\frac{8\pi\alpha_{\nu\nu'}}{3m_\nu m_{\nu'}}\exp\left(-\frac{q^2}{4\tau^2_{\mathrm{hf}}}\right), \qquad \alpha_{\nu\nu'} \equiv \alpha_s(\mathcal{Q}^2_{\nu\nu'}), \qquad \mathcal{Q}^2_{\nu\nu'} = (m_\nu+m_{\nu'})^2. \quad \text{(B21)}$$

Let

$$\mathsf{P}_q = \begin{pmatrix} 1_3 & 0 \\ 0 & 0_6 \end{pmatrix}, \qquad \tilde{\mathsf{A}} = \mathsf{A} + \frac{\mathsf{P}_q}{2\tau^2_{\mathrm{hf}}}. \quad \text{(B22)}$$

The smearing exponential is then absorbed into the same quadratic form, and the complete nine-dimensional integral is analytic,

$$I^{a,\nu\nu'}_{\mathrm{space,HF}} = -\frac{8\pi\alpha_{\nu\nu'}}{3m_\nu m_{\nu'}}\mathcal{N}_4\frac{(2\pi)^{9/2}}{\sqrt{\det\tilde{\mathsf{A}}}} \times \exp\left[-\frac{1}{2}C + \frac{1}{2}\boldsymbol{\eta}^T\tilde{\mathsf{A}}^{-1}\boldsymbol{\eta}\right]. \quad \text{(B23)}$$

The color, flavor, and spin factors are not included in Eq. (B23); they multiply this spatial result through $\kappa^{(J)}_{r,a,\nu\nu',\mathrm{HF}}$ defined in Eq. (43).

4. Schur reduction of the central terms

For the Coulomb and linear-confinement terms, it is useful to retain $\mathbf{q}$ and integrate analytically over $\mathbf{y} = (\mathbf{p}_3,\mathbf{p}_4)^T$. Partition the matrix and vector in Eq. (B18) as

$$\mathsf{A} = \begin{pmatrix} \mathsf{A}_{qq} & \mathsf{A}_{qy} \\ \mathsf{A}_{yq} & \mathsf{A}_{yy} \end{pmatrix}, \qquad \boldsymbol{\eta} = \begin{pmatrix} \boldsymbol{\eta}_q \\ \boldsymbol{\eta}_y \end{pmatrix}, \quad \text{(B24)}$$

where the q block has dimension three and the y block has dimension six. The Gaussian integration over $\mathbf{y}$ gives the reduced form factor

$$\mathcal{G}_{a,\nu\nu'}(\mathbf{q};\mathbf{k},\mathbf{p}) = \mathcal{C}_{a,\nu\nu'}\exp\left[-\frac{1}{2}\mathbf{q}^T\mathsf{G}_{a,\nu\nu'}\mathbf{q} + \mathbf{h}^T_{a,\nu\nu'}\mathbf{q}\right], \quad \text{(B25)}$$

with the Schur complement

$$\mathsf{G}_{a,\nu\nu'} = \mathsf{A}_{qq} - \mathsf{A}_{qy}\mathsf{A}_{yy}^{-1}\mathsf{A}_{yq},$$
$$\mathbf{h}_{a,\nu\nu'} = \boldsymbol{\eta}_q - \mathsf{A}_{qy}\mathsf{A}_{yy}^{-1}\boldsymbol{\eta}_y, \tag{B26}$$

and

$$\mathcal{C}_{a,\nu\nu'} = \mathcal{N}_4 \frac{(2\pi)^3}{\sqrt{\det \mathsf{A}_{yy}}} \exp\left[-\frac{1}{2}C + \frac{1}{2}\boldsymbol{\eta}_y^T \mathsf{A}_{yy}^{-1}\boldsymbol{\eta}_y\right]. \tag{B27}$$

The individual Coulomb spatial integral is therefore

$$I^{a,\nu\nu'}_{\text{space,C}} = 4\pi\alpha_{\nu\nu'} \int d^3q \frac{\mathcal{G}_{a,\nu\nu'}(\mathbf{q})}{q^2}. \tag{B28}$$

For the angular integrations one may choose

$$\mathbf{k} = (0,0,k), \quad \mathbf{p} = \left(p\sqrt{1-u^2}, 0, pu\right), \quad u = \hat{\mathbf{k}}\cdot\hat{\mathbf{p}}. \tag{B29}$$

The remaining measure is $d^3q = q^2 dq d(\cos\theta_q) d\phi_q$. Hence the Coulomb singularity is integrable at the origin, while the Gaussian form factor suppresses the large-q region. The radial and angular ranges used in the evaluation are specified together with the convergence tests in Sec. V and Appendix D.

5. Distributional treatment of linear confinement

The factor $1/q^4$ is a distribution rather than an ordinary integrable function in three dimensions. Its regulated action on a smooth test function $F(\mathbf{q})$ may be written as

$$\left\langle \left[\frac{1}{q^4}\right]_R, F \right\rangle \equiv \lim_{\epsilon\to 0^+}\left[\int d^3q \frac{F(\mathbf{q})}{(q^2+\epsilon^2)^2} - \frac{\pi^2}{\epsilon}F(\mathbf{0})\right]$$
$$= \int d^3q \frac{F(\mathbf{q}) - F(\mathbf{0})}{q^4}, \tag{B30}$$

where the last expression is understood with symmetric angular integration. Indeed, its angular average obeys

$$\frac{1}{4\pi}\int d\Omega_q [F(q\hat{\mathbf{q}}) - F(\mathbf{0})] = \mathcal{O}(q^2), \tag{B31}$$

which makes the radial integral finite at $q = 0$.

In the QI amplitude, we apply the distribution after forming the complete spin-independent, color-weighted diagram sum. This organization makes the color-neutrality cancellation explicit and is numerically stable. Applying the same regulated distribution to the separate diagram contributions is algebraically equivalent, provided that the subtraction is retained consistently. For representation r and topology a, define

$$\mathcal{F}^{(J)}_{r,a}(\mathbf{q}) = \sum_{\nu\nu'\in\mathcal{P}_{r,a}} \kappa^{(J)}_{r,a,\nu\nu',\text{CL}} \mathcal{G}_{a,\nu\nu'}(\mathbf{q}),$$
$$\mathcal{F}^{\alpha,(J)}_{r,a}(\mathbf{q}) = \sum_{\nu\nu'\in\mathcal{P}_{r,a}} \kappa^{(J)}_{r,a,\nu\nu',\text{CL}} \alpha_{\nu\nu'} \mathcal{G}_{a,\nu\nu'}(\mathbf{q}). \tag{B32}$$

At $\mathbf{q} = \mathbf{0}$, the momentum shifts vanish, so the individual overlaps become independent of the interacting pair within a fixed topology,

$$\mathcal{G}_{a,\nu\nu'}(\mathbf{0}) = \mathcal{G}^{(0)}_a \qquad (\nu\nu' \in \mathcal{P}_{r,a}). \tag{B33}$$

Using Eq. (43), one then obtains

$$\mathcal{F}^{(J)}_{r,a}(\mathbf{0}) = \mathcal{G}^{(0)}_a \sum_{\nu\nu'\in\mathcal{P}_{r,a}} \kappa^{(J)}_{r,a,\nu\nu',\text{CL}}$$
$$= \frac{1}{2}\mathcal{G}^{(0)}_a I^a_F I^{a,J}_{S,\text{CL}} \sum_{\nu\nu'\in\mathcal{P}_{r,a}} I^a_{C,r}(\nu\nu') = 0. \tag{B34}$$

The final equality is the color-singlet zero-sum identity in Eq. (A18). It holds separately in the prior and post representations and separately for F_{14} and F_{15}. The prior and post terms of a fixed topology may therefore be combined before the transferred-momentum integration. This gives the same result as treating the two representations separately in the formulas below.

Since the coefficient κ already contains the single prior-post factor $1/2$, the central contribution carried by representation r can be written compactly as

$$\mathcal{V}^{(J)}_{r,a,\text{CL}} = 4\pi \int d^3q \frac{\mathcal{F}^{\alpha,(J)}_{r,a}(\mathbf{q})}{q^2}$$
$$+ 6\pi b \int d^3q \frac{\mathcal{F}^{(J)}_{r,a}(\mathbf{q}) - \mathcal{F}^{(J)}_{r,a}(\mathbf{0})}{q^4}. \tag{B35}$$

Although Eq. (B34) makes the subtracted constant vanish analytically, retaining the difference in Eq. (B35) enforces the distributional definition and keeps the small-q evaluation stable. The subtraction itself follows from the distributional definition in Eq. (B30). Color neutrality makes the zero-transfer constant vanish in the complete intercluster sum, so no adjustable infrared regulator or arbitrary additive confinement constant is introduced.

The hyperfine contribution from the same representation is

$$\mathcal{V}^{(J)}_{r,a,\text{HF}} = \sum_{\nu\nu'\in\mathcal{P}_{r,a}} \kappa^{(J)}_{r,a,\nu\nu',\text{HF}} I^{r,a,\nu\nu'}_{\text{space,HF}}, \tag{B36}$$

and the labeled topology kernel is

$$V^{(J)}_a = \sum_{r\in\{\text{pr,po}\}} \left(\mathcal{V}^{(J)}_{r,a,\text{CL}} + \mathcal{V}^{(J)}_{r,a,\text{HF}}\right). \tag{B37}$$

No additional prior-post averaging factor is to be applied to Eq. (B37). The combination of the two labeled topologies into the normalized identical-quark final state is derived separately in Appendix C.

Finally, the dimensions provide a direct normalization check. With the normalizations of Appendix A 1,

$$[\phi_M]=\mathrm{GeV}^{-3/2},\quad [\phi_B]=\mathrm{GeV}^{-3},\quad [v^X_{\nu\nu'}]=\mathrm{GeV}^{-2}. \tag{B38}$$

The intermediate Gaussian quantities have dimensions

$$[\mathsf{A}]=[\mathsf{G}]=\mathrm{GeV}^{-2},\qquad [\boldsymbol{\eta}]=[\mathbf{h}]=\mathrm{GeV}^{-1},$$
$$[C]=1,\qquad [\mathcal{C}_{a,\nu\nu'}]=\mathrm{GeV}^{-3}. \tag{B39}$$

The nine-dimensional measure in Eq. (B11) therefore gives

$$[I_{\mathrm{space},X}]=[V_a^{(J)}]=\mathrm{GeV}^{-2}. \tag{B40}$$

After the molecular folding in Eq. (52), $[R_0]=\mathrm{GeV}^{-3/2}$ implies $[T^{(J)}_{00,\mathrm{QI};fi}]=\mathrm{GeV}^{-1/2}$, in agreement with the width normalization of Eq. (23).

APPENDIX C: IDENTICAL-QUARK ANTISYMMETRIZATION AND TOPOLOGY NORMALIZATION

This Appendix derives the relative sign and normalization with which the two labeled open-charm clusterings, F_{14} and F_{15}, enter the physical charged-component kernel. The derivation uses the constituent labels and state phases fixed in Appendix A. It also clarifies the separate exact-isospin projection used to obtain the physical $I=1/2$ amplitude.

1. Asymptotic state of the two identical light quarks

Let P_{45} interchange all one-particle variables carried by the two identical u quarks. In the temporarily labeled first-quantized space,

$$P_{45}^\dagger=P_{45},\qquad P_{45}^2=1, \tag{C1}$$

and the projector onto the antisymmetric two-u subspace is

$$\Pi_{45}^{(-)}=\frac{1-P_{45}}{2}. \tag{C2}$$

The two labeled final clusterings introduced in Eqs. (25) and (26) obey

$$|F_{15}\rangle=P_{45}|F_{14}\rangle. \tag{C3}$$

The minus sign required between them can also be seen directly from fermion creation operators. For a normalized one-particle wave packet f, define the smeared operator

$$u^\dagger[f]=\sum_\alpha f_\alpha u^\dagger_\alpha, \tag{C4}$$

where α collectively denotes momentum, spin, and color. The canonical anticommutation relations give

$$\{u[f],u^\dagger[g]\}=\langle f|g\rangle,\qquad \{u^\dagger[f],u^\dagger[g]\}=0. \tag{C5}$$

If f_M and f_B are the asymptotic modes associated with the final meson and baryon, respectively, then

$$u^\dagger[f_M]u^\dagger[f_B]|0\rangle \leftrightarrow \frac{|f_M\rangle_4|f_B\rangle_5-|f_B\rangle_4|f_M\rangle_5}{\sqrt{2}}. \tag{C6}$$

The spectator constituents and the sums over the internal cluster variables have been suppressed in Eq. (C6). Restoring them identifies the first term with F_{14} and the second with F_{15}. Thus the relative minus sign is a consequence of the anticommutation of the two identical-u creation operators; it is not a phase chosen separately for the decay amplitude.

For asymptotically separated meson and baryon wave packets, $\langle f_M|f_B\rangle=0$. Equivalently, the labeled cluster states obey

$$\langle F_{14}|F_{14}\rangle=\langle F_{15}|F_{15}\rangle=1,\qquad \langle F_{14}|F_{15}\rangle=0. \tag{C7}$$

The normalized antisymmetric final state associated with the explicitly evaluated charged initial component is therefore

$$|F_{\mathrm{AS}}\rangle=\sqrt{2}\Pi_{45}^{(-)}|F_{14}\rangle=\frac{|F_{14}\rangle-|F_{15}\rangle}{\sqrt{2}}, \tag{C8}$$

which reproduces Eq. (48).

2. Exchange parity of the initial and final cluster states

The exchange property of the initial state follows separately from its internal factors. For the u_4u_5 pair in the ground-state Σ_c^{++},

$$P_{45}\chi^c_{AB}=-\chi^c_{AB},\qquad P_{45}\chi^f_{AB}=+\chi^f_{AB},$$
$$P_{45}\chi^s_{AB}=+\chi^s_{AB},\qquad P_{45}\phi_{AB}=+\phi_{AB}. \tag{C9}$$

The color sign follows from $\epsilon_{a_3a_4a_5}=-\epsilon_{a_3a_5a_4}$; the flavor state u_4u_5, the light-pair spin triplet, and the ground-state spatial wave function are symmetric. Consequently, the complete initial state has the required fermionic exchange parity,

$$P_{45}|AB;JM_J\rangle=-|AB;JM_J\rangle. \tag{C10}$$

For the final labeled state, P_{45} moves the light quark in the meson to the baryon and the light quark in the baryon to the meson. With the common cluster ordering M_fB_f and the phases of Appendix A, this maps

$$M_f(14)B_f(325)\xrightarrow{P_{45}}M_f(15)B_f(324),$$
$$\chi^c_{F_{14}}\chi^f_{F_{14}}\chi^s_{F_{14}}\phi_{F_{14}}\xrightarrow{P_{45}}\chi^c_{F_{15}}\chi^f_{F_{15}}\chi^s_{F_{15}}\phi_{F_{15}}, \tag{C11}$$

which is the component form of Eq. (C3).

3. Relation between the two labeled kernels

For $r\in\{\mathrm{pr},\mathrm{po}\}$, let $\hat{\mathcal{V}}_{r,a}$ denote the complete pair-interaction sum for representation r and labeled topology a. Exact isospin symmetry gives $m_4=m_5$, and the two u quarks use the same internal widths and constituent interaction. Hence

$$P_{45}\hat{\mathcal{V}}_{r,14}P_{45}=\hat{\mathcal{V}}_{r,15}. \tag{C12}$$

At the diagram level, the required pair mappings are

$$(13,14,15,23,24,25)\xrightarrow{4\leftrightarrow5}(13,15,14,23,25,24), \tag{C13}$$

$$(13,12,15,43,42,45)\xrightarrow{4\leftrightarrow5}(13,12,14,53,52,54). \tag{C14}$$

The first line is the prior set in a permuted order, while the second maps the F_{14} post set into the F_{15} post set. Under the same exchange, the spin and spatial arguments are relabeled as in Appendixes A and B. Equation (C12) therefore applies to the complete color-flavor-spin weighted sum, including both the CL and HF interactions.

Using Eqs. (C3), (C10), and (C12), one obtains

$$\begin{aligned}V^{(J)}_{r,15}&=\langle F_{15};JM_J|\hat{\mathcal{V}}_{r,15}|AB;JM_J\rangle\\&=\langle F_{14};JM_J|P_{45}(P_{45}\hat{\mathcal{V}}_{r,14}P_{45})|AB;JM_J\rangle\\&=-\langle F_{14};JM_J|\hat{\mathcal{V}}_{r,14}|AB;JM_J\rangle=-V^{(J)}_{r,14}.\end{aligned} \tag{C15}$$

The relation holds separately for the prior and post representations. It is therefore preserved by their arithmetic average,

$$V^{(J)}_{15}=-V^{(J)}_{14}, \tag{C16}$$

and holds before the molecular radial and partial-wave integrations. In particular, it is valid pointwise in the external variables (k,p,u).

Projecting the transition onto the normalized state in Eq. (C8) gives

$$\begin{aligned}V^{(J)}_{\mathrm{ch}}&=\langle F_{\mathrm{AS}};JM_J|\hat{\mathcal{V}}|AB;JM_J\rangle\\&=\frac{V^{(J)}_{14}-V^{(J)}_{15}}{\sqrt{2}}=\sqrt{2}V^{(J)}_{14}.\end{aligned} \tag{C17}$$

The $1/\sqrt{2}$ in the normalized external state is distinct from the fixed-topology flavor overlap $I_F^{14}=I_F^{15}=1/\sqrt{2}$ derived in Eq. (A22). Both are also distinct from the factor $1/2$ used once in the prior-post average. Equation (C17) contains no additional prior-post factor.

The factor $\sqrt{2}$ is a coherent quark-line normalization effect, rather than a fitted enhancement or a final-state phase-space multiplicity. The asymptotic hadrons Λ_c and $\bar{D}^{(*)}$ are distinguishable, so no $1/2!$ identical-particle factor is introduced in the two-body width.

4. Exact-isospin reconstruction

For completeness, the topology normalization can be combined with the charge-state projection of Sec. II A. Define

$$\begin{aligned}V^{(J)}_{\mathrm{ch}}&=\langle\Lambda_c^+\bar{D}^{(*)0}|\hat{\mathcal{V}}|\Sigma_c^{++}D^{(*)-}\rangle,\\V^{(J)}_{\mathrm{neu}}&=\langle\Lambda_c^+\bar{D}^{(*)0}|\hat{\mathcal{V}}|\Sigma_c^{+}\bar{D}^{(*)0}\rangle.\end{aligned} \tag{C18}$$

In the Condon-Shortley convention of Eq. (4), the orthogonal $I=3/2$ state is

$$\left|\frac{3}{2},\frac{1}{2}\right\rangle=\frac{1}{\sqrt{3}}|\Sigma_c^{++}D^{(*)-}\rangle+\sqrt{\frac{2}{3}}|\Sigma_c^{+}\bar{D}^{(*)0}\rangle. \tag{C19}$$

An isospin-conserving interaction cannot connect this state to the $I=1/2$ final channel. Therefore,

$$\frac{1}{\sqrt{3}}V^{(J)}_{\mathrm{ch}}+\sqrt{\frac{2}{3}}V^{(J)}_{\mathrm{neu}}=0,\qquad V^{(J)}_{\mathrm{neu}}=-\frac{V^{(J)}_{\mathrm{ch}}}{\sqrt{2}}. \tag{C20}$$

Projection of the initial $I=1/2$ state then gives

$$V^{(J)}_{\mathrm{QI};fi}=\sqrt{\frac{2}{3}}V^{(J)}_{\mathrm{ch}}-\frac{1}{\sqrt{3}}V^{(J)}_{\mathrm{neu}}=\sqrt{\frac{3}{2}}V^{(J)}_{\mathrm{ch}}=\sqrt{3}V^{(J)}_{14}. \tag{C21}$$

The last equality combines two logically separate operations: antisymmetrizing the identical u quarks in the charged component and projecting that charged component onto the exact $I=1/2$ molecular state. Physical charge splittings used in thresholds and final-state kinematics do not alter this amplitude normalization convention.

5. Finite exchange overlap

Equation (C7) is an asymptotic external-state statement. At finite cluster separation, quark exchange can produce a nonzero overlap between the two labeled clusterings. For normalized wave packets, define

$$S_{45}=\langle F_{14}|P_{45}|F_{14}\rangle=\langle F_{14}|F_{15}\rangle. \tag{C22}$$

Since P_{45} is Hermitian, S_{45} is real, and the normalized antisymmetric combination would contain

$$|F_{\rm AS}\rangle_{\rm finite} = \frac{|F_{14}\rangle - |F_{15}\rangle}{\sqrt{2(1-S_{45})}}. \tag{C23}$$

For continuum cluster states, the corresponding exchange contribution is a nonlocal norm kernel,

$$\mathcal{N}_{45}(\mathbf{k}',\mathbf{k}) = \langle F_{14};\mathbf{k}'|P_{45}|F_{14};\mathbf{k}\rangle. \tag{C24}$$

A finite-overlap treatment would require simultaneous Hamiltonian and norm kernels, with an orthogonalized kernel of the schematic form $\mathcal{N}^{-1/2}\mathcal{H}\mathcal{N}^{-1/2}$. Such a resonating-group treatment is not part of the present first-Born calculation. We instead use normalized asymptotic hadron states, for which $S_{45}\to 0$ and Eq. (C8) follows. The simple $\sqrt{2}$ in Eq. (C17) should therefore not be interpreted as an estimate of finite-separation exchange dynamics.

APPENDIX D: ADDITIONAL ANALYTIC AND NUMERICAL CONSISTENCY CHECKS

This Appendix supplements the compact validation summary in Sec. V. We first document the pointwise identities and the higher-order quadrature comparison for the QI amplitudes. We then give the endpoint treatment of the retarded OPE fold, an independent expression for its absorptive part, and representative contact-pole and coherent-width identities. The parameter variations defined in Sec. V D test physical and model assumptions and are distinct from the numerical comparisons collected here.

1. QI identities and quadrature refinement

The internal-state conventions of Appendix A imply the exact normalizations

$$\langle \chi^c_{AB}|\chi^c_{AB}\rangle = \langle \chi^c_{F_{14}}|\chi^c_{F_{14}}\rangle = \langle \chi^c_{F_{15}}|\chi^c_{F_{15}}\rangle = 1,$$
$$I_F^{14} = I_F^{15} = \frac{1}{\sqrt{2}}, \qquad \sum_{\nu\nu'\in\mathcal{P}_{r,a}} I^a_{C,r}(\nu\nu') = 0. \tag{D1}$$

The last relation removes the zero-transfer constant from the distributional confinement kernel, as derived in Appendix B. The representative color-flavor-spin coefficient also reproduces

$$\kappa^{(1/2)}_{\rm pr,14,13,HF} = \frac{\sqrt{6}}{144}, \tag{D2}$$

in agreement with Eq. (45).

It is useful to state the topology check at the level at which the molecular fold is performed. Let $V^{(J)}_{r,a,X}(k,p,u)$ denote the kernel for prior or post representation r, labeled topology a, and interaction part $X\in\{\mathrm{CL},\mathrm{HF}\}$. The exchange argument of Appendix C gives

$$\mathcal{R}^{(J)}_{r,X}(k,p,u) \equiv V^{(J)}_{r,14,X}(k,p,u) + V^{(J)}_{r,15,X}(k,p,u) = 0. \tag{D3}$$

This relation is satisfied separately by the spin-independent and hyperfine parts, for both prior and post representations, before the integrations over p and u. The subsequent normalization chain is therefore

$$V^{(J)}_{\rm ch} = \sqrt{2}V^{(J)}_{14}, \qquad V^{(J)}_{{\rm QI};fi} = \sqrt{\frac{3}{2}}V^{(J)}_{\rm ch} = \sqrt{3}V^{(J)}_{14}, \tag{D4}$$

with no additional topology, flavor, or prior-post factor.

To isolate quadrature effects, all orders are raised simultaneously from

$$(N_p, N_u; N_q, N_{u_q}, N_\phi) = (20,16;24,12,12) \tag{D5}$$

to

$$(N_p, N_u; N_q, N_{u_q}, N_\phi) = (28,22;32,16,16), \tag{D6}$$

while keeping $p^{\rm QI}_{\rm max} = 1.6$ GeV and $q_{\rm max} = 4.0$ GeV fixed. Table XIV lists the result for every calculated S-wave channel. We define

TABLE XIV. QI quadrature refinement for all eight calculated S-wave channels. Widths are in MeV. The two $J = 3/2\to\Lambda_c\bar{D}$ modes are D waves and are not part of this comparison.

Initial state	J	Final state	$\Gamma_{\rm ref}$	$\Gamma_{\rm high}$	δ_Γ (%)
$P_c(4312)$	$\frac{1}{2}$	$\Lambda_c\bar{D}$	0.0028477648	0.0028477648	$< 10^{-6}$
$P_c(4312)$	$\frac{1}{2}$	$\Lambda_c\bar{D}^*$	0.7421105620	0.7421105626	7.19×10^{-8}
$P_c(4440)$	$\frac{1}{2}$	$\Lambda_c\bar{D}$	0.0360671554	0.0360671894	9.42×10^{-5}
$P_c(4440)$	$\frac{1}{2}$	$\Lambda_c\bar{D}^*$	0.4953352423	0.4953354563	4.32×10^{-5}
$P_c(4440)$	$\frac{3}{2}$	$\Lambda_c\bar{D}^*$	0.0450681927	0.0450682250	7.16×10^{-5}
$P_c(4457)$	$\frac{1}{2}$	$\Lambda_c\bar{D}$	0.0010560078	0.0010560077	8.63×10^{-6}
$P_c(4457)$	$\frac{1}{2}$	$\Lambda_c\bar{D}^*$	0.0808195485	0.0808195502	2.01×10^{-6}
$P_c(4457)$	$\frac{3}{2}$	$\Lambda_c\bar{D}^*$	0.0084765093	0.0084765095	2.72×10^{-6}

$$\delta_\Gamma = 100\left|\frac{\Gamma_{\rm high}-\Gamma_{\rm ref}}{\Gamma_{\rm ref}}\right|. \tag{D7}$$

The largest change is the $P_c(4440), J=1/2\to\Lambda_c\bar{D}$ entry, 0.0360671554→0.0360671894 MeV, corresponding to $9.42\times10^{-5}\%$. Thus the numerical integration uncertainty of the reference grid is negligible compared with the one-at-a-time variations of the molecular and constituent-model inputs.

2. Pion-pole endpoints and interval mapping

For fixed final momentum k, recall from Eq. (67) that the angular denominator is $D_0 - D_1 u - i0$. It is useful to define the two endpoint functions

$$D_\pm(p,k) \equiv D_0(p,k) \pm D_1(p,k), \qquad D_1(p,k) = 2pk. \tag{D8}$$

The endpoints of the on-shell angular interval occur when the pole reaches $u=\pm1$. They are therefore the positive roots of

$$D_-(p,k)=0, \qquad D_+(p,k)=0. \tag{D9}$$

All roots in $0<p<p^\pi_{\rm max}$ are bracketed and then refined. Together with 0 and $p^\pi_{\rm max}$, they define an ordered partition

$$0=p_0<p_1<\cdots<p_n=p^\pi_{\rm max}. \tag{D10}$$

On each interval $[p_j,p_{j+1}]$, we use $x\in[-1,1]$ and the mapping

$$p(x)=p_j+(p_{j+1}-p_j)\sin^2\left[\frac{\pi}{4}(x+1)\right],$$
$$\frac{dp}{dx}=\frac{\pi}{4}(p_{j+1}-p_j)\sin\left[\frac{\pi}{2}(x+1)\right]. \tag{D11}$$

The vanishing Jacobian at both ends clusters the integration points near an endpoint cusp and controls the integrable logarithms in Eq. (68). For the reference $P_c(4312)\to\Lambda_c\bar{D}^*$ case with the direct baryon-line energy transfer and $\Lambda_\pi = 0.50$ GeV, one finds

$$k=0.199560876\,\text{GeV},$$
$$p_1=0.116819670\,\text{GeV}, \quad p_2=0.311762532\,\text{GeV}. \tag{D12}$$

Both internal endpoints in this case are roots of $D_-(p,k)$, and the on-shell angular region lies between them.

3. Independent absorptive-part relation

The physical-sheet identity

$$\frac{1}{x-i0}=\mathrm{PV}\frac{1}{x}+i\pi\delta(x) \tag{D13}$$

gives an expression for the imaginary part that does not require evaluating the real logarithm. Defining

$$\Omega_\pi(k)=\{p\in[0,p^\pi_{\rm max}]:|D_0(p,k)|<D_1(p,k)\}, \tag{D14}$$

one has

$$\mathrm{Im}\,\mathcal{L}_\pi(p,k)=\frac{\pi}{D_1(p,k)}\Theta(D_1-|D_0|). \tag{D15}$$

Consequently, the absorptive part of the pion-pole amplitude is

$$\mathrm{Im}\,T^{(J)}_{00,\pi,\mathrm{pole};fi}=-\frac{|g||g_2|\hat{c}^{(J)}_{fi}}{f_\pi^2}\int_{\Omega_\pi(k)}dp\,p^2R_0(p)F_{\Lambda_\pi}(k,p)\times\frac{\pi\Delta_\pi(p,k)}{D_1(p,k)}. \tag{D16}$$

The contactlike contribution is real, so the full and pion-pole kernels have the same imaginary part. For the reference channel of Eq. (D12), evaluating Eq. (D16) gives

$$\mathrm{Im}\,T^{(1/2)}_{00,\pi,\mathrm{pole}}=0.274212282530\ \text{GeV}^{-1/2}, \tag{D17}$$

identical in the displayed digits to the result obtained from the complex logarithm in Eq. (68). This check fixes the sign of the physical-sheet imaginary part. It does not turn the first-Born treatment into a unitary three-body calculation or define a separate $\Lambda_c\bar{D}^{(*)}\pi$ partial width.

4. Contact-pole and coherent-width identities

The distributional decomposition in Eq. (69) requires the folded amplitudes to obey

$$T^{(J)}_{00,\pi,\mathrm{full};fi}=T^{(J)}_{00,\pi,\mathrm{ct};fi}+T^{(J)}_{00,\pi,\mathrm{pole};fi}. \tag{D18}$$

For the same reference $P_c(4312)\to\Lambda_c\bar{D}^*$ transition,

$$T^{(1/2)}_{00,\pi,\mathrm{ct}}=2.383195854,$$
$$T^{(1/2)}_{00,\pi,\mathrm{pole}}=0.463697755+0.274212283i, \qquad [\text{GeV}^{-1/2}].$$
$$T^{(1/2)}_{00,\pi,\mathrm{full}}=2.846893609+0.274212283i, \tag{D19}$$

The residual of Eq. (D18) is below 3×10^{-15} GeV$^{-1/2}$. This is an internal identity, not a preference for the full OPE kernel. As explained in Sec. IV D, the full kernel is retained only as a short-distance matching diagnostic.

The coherent-width relation supplies a second independent check. Writing

$$\Gamma^{(J)}_{\mathrm{int};fi}=2\rho_{fi}\mathrm{Re}\left[T^{(J)}_{00,\mathrm{QI};fi}T^{(J)*}_{00,\pi,\mathrm{ref};fi}\right], \tag{D20}$$

Eq. (83) becomes

$$\Gamma^{(J)}_{\mathrm{tot};fi}(\eta_{\mathrm{match}}) = \Gamma^{(J)}_{\mathrm{QI};fi} + \Gamma^{(J)}_{\pi,\mathrm{ref};fi} + \eta_{\mathrm{match}}\Gamma^{(J)}_{\mathrm{int};fi}. \quad \text{(D21)}$$

For the reference $P_c(4312)\to\Lambda_c\bar{D}^*$ case, the individual terms are

$$\begin{aligned}\Gamma^{(1/2)}_{\mathrm{QI};fi} &= 0.742110562\ \mathrm{MeV},\\ \Gamma^{(1/2)}_{\pi,\mathrm{ref};fi} &= 0.250633751\ \mathrm{MeV},\\ \Gamma^{(1/2)}_{\mathrm{int};fi} &= 0.742445183\ \mathrm{MeV},\end{aligned} \quad \text{(D22)}$$

which yield

$$\Gamma_+ = 1.735189496\ \mathrm{MeV}, \qquad \Gamma_- = 0.250299130\ \mathrm{MeV}. \quad \text{(D23)}$$

The direct evaluation of $\rho_{fi}|T^{(J)}_{00,\mathrm{tot};fi}(\eta_{\mathrm{match}})|^2$ agrees with Eq. (D21) to better than 5×10^{-16} MeV. The same global η_{match} must be used in every channel; this identity does not permit a separate sign choice for each decay.

5. OPE quadrature and radial-endpoint convergence

Table XV gives the complex amplitudes underlying the compact OPE convergence summary in Sec. V. Both tests use the reference $P_c(4312)\to\Lambda_c\bar{D}^*$ channel, the direct baryon-line energy transfer, the pion-pole kernel, and $\Lambda_\pi = 0.50$ GeV. The quadrature-order comparison keeps $p^\pi_{\max} = 2$ GeV fixed. In the radial-endpoint comparison, $N_\pi = 256$ is used for both endpoints so that the high-momentum tail is isolated from the quadrature-order difference.

TABLE XV. Complex amplitudes in the detailed OPE convergence comparison. The first two rows vary N_π at $p^\pi_{\max} = 2$ GeV; the last two vary $p^\pi_{\max}$ at $N_\pi = 256$. Amplitudes are in $\mathrm{GeV}^{-1/2}$.

Setting	$T_{00,\pi,\mathrm{pole}}$
$N_\pi = 64$	$0.463697754671 + 0.274212282530i$
$N_\pi = 128$	$0.463697656416 + 0.274212282530i$
$p^\pi_{\max} = 2$ GeV	$0.463697650177 + 0.274212282530i$
$p^\pi_{\max} = 3$ GeV	$0.463697650361 + 0.274212282530i$

The reference result reported in Sec. VI uses $N_\pi = 64$ and $p^\pi_{\max} = 2$ GeV. The absolute differences between the two quadrature orders and between the two radial endpoints are, respectively, 9.83×10^{-8} and 1.84×10^{-10} $\mathrm{GeV}^{-1/2}$. They are many orders of magnitude smaller than the changes generated by the cutoff, energy-transfer prescription, and contact treatment. The numerical stability demonstrated here therefore does not reduce the matching ambiguities attached to the exploratory OPE scenarios.

[1] H.-X. Chen, W. Chen, X. Liu, and S.-L. Zhu, The hidden-charm pentaquark and tetraquark states, Phys. Rep. **639**, 1 (2016).

[2] R. F. Lebed, R. E. Mitchell, and E. S. Swanson, Heavy-quark QCD exotica, Prog. Part. Nucl. Phys. **93**, 143 (2017).

[3] V. Patel, J. Oudichhya, and A. K. Rai, Mass spectra of $qq\bar{q}\,\bar{q}$, $ss\bar{s}\,\bar{s}$, and $qq\bar{s}\,\bar{s}$ tetraquarks using regge phenomenology, Eur. Phys. J. A **61**, 218 (2025).

[4] V. Patel, J. Oudichhya, and A. K. Rai, Spectroscopy of $cc\bar{c}\,\bar{c}$ and $ss\bar{c}\,\bar{c}$ tetraquarks within the framework of regge phenomenology, Few-Body Syst. **66**, 39 (2025).

[5] V. Patel, J. Oudichhya, and A. K. Rai, Spectroscopic study of $ss\bar{b}\,\bar{b}$ and $bb\bar{b}\,\bar{b}$ tetraquarks using regge phenomenology, Int. J. Mod. Phys. A **40**, 2550152 (2025).

[6] C. Lodha, M. Parmar, and A. K. Rai, Exploring beauty bound states: Mass spectra and decay dynamics of B mesons and $bq\bar{q}\,\bar{q}$ tetraquarks, Eur. Phys. J. Plus **141**, 453 (2026).

[7] H. Rathod and A. K. Rai, Study of singly charmed pentaquark using the hypercentral constituent quark model approach, Eur. Phys. J. A **62**, 125 (2026).

[8] LHCb Collaboration, Observation of $J/\psi p$ resonances consistent with pentaquark states in $\Lambda_b^0\to J/\psi K^- p$ decays, Phys. Rev. Lett. **115**, 072001 (2015).

[9] LHCb Collaboration, Observation of a narrow pentaquark state, $P_c(4312)^+$, and of a two-peak structure of the $P_c(4450)^+$, Phys. Rev. Lett. **122**, 222001 (2019).

[10] F.-K. Guo, C. Hanhart, U.-G. Meißner, Q. Wang, Q. Zhao, and B.-S. Zou, Hadronic molecules, Rev. Mod. Phys. **90**, 015004 (2018).

[11] H.-X. Chen, W. Chen, X. Liu, Y.-R. Liu, and S.-L. Zhu, An updated review of the new hadron states, Rep. Prog. Phys. **86**, 026201 (2023).

[12] M.-Z. Liu, Y.-W. Pan, F.-Z. Peng, M. S. Sánchez, L.-S. Geng, A. Hosaka, and M. P. Valderrama, Emergence of a complete heavy-quark spin symmetry multiplet: Seven molecular pentaquarks in light of the latest LHCb analysis, Phys. Rev. Lett. **122**, 242001 (2019).

[13] C. W. Xiao, J. Nieves, and E. Oset, Heavy-quark spin symmetric molecular states from $\bar{D}^{(*)}\Sigma_c^{(*)}$ and other coupled channels in the light of the recent LHCb pentaquarks, Phys. Rev. D **100**, 014021 (2019).

[14] M.-L. Du, V. Baru, F.-K. Guo, C. Hanhart, U.-G. Meißner, J. A. Oller, and Q. Wang, Revisiting the nature of the P_c pentaquarks, J. High Energy Phys. 08 (2021) 157.

[15] M. B. Voloshin, Some decay properties of hidden-charm pentaquarks as baryon-meson molecules, Phys. Rev. D **100**, 034020 (2019).

[16] S. Sakai, H.-J. Jing, and F.-K. Guo, Decays of P_c into $J/\psi N$ and $\eta_c N$ with heavy-quark spin symmetry, Phys. Rev. D **100**, 074007 (2019).
[17] Y.-H. Lin and B.-S. Zou, Strong decays of the latest LHCb pentaquark candidates in hadronic molecule pictures, Phys. Rev. D **100**, 056005 (2019).
[18] G.-J. Wang, L.-Y. Xiao, R. Chen, X.-H. Liu, X. Liu, and S.-L. Zhu, Probing hidden-charm decay properties of P_c states in a molecular scenario, Phys. Rev. D **102**, 036012 (2020).
[19] Z.-H. Guo and J. A. Oller, Anatomy of the newly observed hidden-charm pentaquark states: $P_c(4312)$, $P_c(4440)$, and $P_c(4457)$, Phys. Lett. B **793**, 144 (2019).
[20] Y.-W. Pan, M.-Z. Liu, and L.-S. Geng, Production rates of hidden-charm pentaquark molecules in Λ_b decays, Phys. Rev. D **108**, 114022 (2023).
[21] Y. Dong, P. Shen, F. Huang, and Z. Zhang, Selected strong decays of pentaquark state $P_c(4312)$ in a chiral constituent quark model, Eur. Phys. J. C **80**, 341 (2020).
[22] Q. Li, C.-H. Chang, T. Wang, and G.-L. Wang, Strong decays of $P_\psi^N(4312)^+$ to $J/\psi(\eta_c)p$ and $\bar{D}^{(*)}\Lambda_c$ within the Bethe–Salpeter framework, J. High Energy Phys. 06 (2023) 189.
[23] Z.-Y. Lin, J.-B. Cheng, B.-L. Huang, and S.-L. Zhu, P_c states and their open-charm decays with the complex scaling method, Phys. Rev. D **108**, 114014 (2023).
[24] K. Phumphan, K. Xu, W. Ruangyoo, C.-C. Chen, A. Limphirat, and Y. Yan, Group theory analysis of P_c resonances in molecular picture, arXiv:2105.03150.
[25] Z.-Y. Yang, J. Song, W.-H. Liang, and E. Oset, $P_c(4440)$ and $P_c(4457)$ decay into $\bar{D}\Sigma_c$ and $\bar{D}\Lambda_c$ and the spin of the P_c states, Eur. Phys. J. C **85**, 954 (2025).
[26] Q. Li, C.-H. Chang, X. Tong, X.-Z. Tan, T. Wang, and G.-L. Wang, Strong decays of $P_\psi^N(4440)^+$ and $P_\psi^N(4457)^+$ within the Bethe–Salpeter framework, J. High Energy Phys. 10 (2025) 098.
[27] N. Brambilla, A. Mohapatra, and A. Vairo, Unraveling pentaquarks with the Born–Oppenheimer effective theory, Phys. Rev. D **112**, 114037 (2025).
[28] J.-C. Deng, Y. Ru, X.-Y. Wan, T.-F. Feng, and B. Wang, Strong decays of the hidden-charm molecular pentaquarks, Phys. Rev. D **113**, 114011 (2026).
[29] T. J. Burns and E. S. Swanson, Experimental constraints on the properties of P_c states, Eur. Phys. J. A **58**, 68 (2022).
[30] M.-Z. Liu, Y.-W. Pan, and L.-S. Geng, Studying the heavy quark spin symmetry multiplet of hadronic molecules $\bar{D}^{(*)}\Sigma_c^{(*)}$ in the three-body decays of $\bar{D}^{(*)}\Lambda_c\pi$, Phys. Rev. D **110**, 114022 (2024).
[31] R. Xu, L. Meng, H.-X. Zhu, N. Li, and W. Chen, Towards modeling the short-range interactions of hidden/open charm pentaquark molecular states, Phys. Rev. D **111**, 094015 (2025).
[32] LHCb Collaboration, Observation of $\Lambda_b^0 \to \Lambda_c^+ \bar{D}^{(*)0} K^-$ and $\Lambda_b^0 \to \Lambda_c^+ D_s^{*-}$ decays, Eur. Phys. J. C **84**, 575 (2024).
[33] LHCb Collaboration, Search for prompt production of pentaquarks in charm hadron final states, Phys. Rev. D **110**, 032001 (2024).
[34] M. P. Valderrama, One-pion exchange and the quantum numbers of the $P_c(4440)$ and $P_c(4457)$ pentaquarks, Phys. Rev. D **100**, 094028 (2019).
[35] T. Barnes and E. S. Swanson, A diagrammatic approach to meson–meson scattering in the nonrelativistic quark potential model, Phys. Rev. D **46**, 131 (1992).
[36] E. S. Swanson, Inter-meson potentials from the constituent quark model, Ann. Phys. (N.Y.) **220**, 73 (1992).
[37] T. Barnes and E. S. Swanson, Kaon–nucleon scattering amplitudes and Z^* enhancements from quark born diagrams, Phys. Rev. C **49**, 1166 (1994).
[38] C.-Y. Wong, E. S. Swanson, and T. Barnes, Heavy quarkonium dissociation cross sections in relativistic heavy-ion collisions, Phys. Rev. C **65**, 014903 (2001); **66**, 029901(E) (2002).
[39] J. P. Hilbert, N. Black, T. Barnes, and E. S. Swanson, Charmonium–nucleon dissociation cross sections in the quark model, Phys. Rev. C **75**, 064907 (2007).
[40] S. Navas *et al.* (Particle Data Group), Review of particle physics, Phys. Rev. D **110**, 030001 (2024).